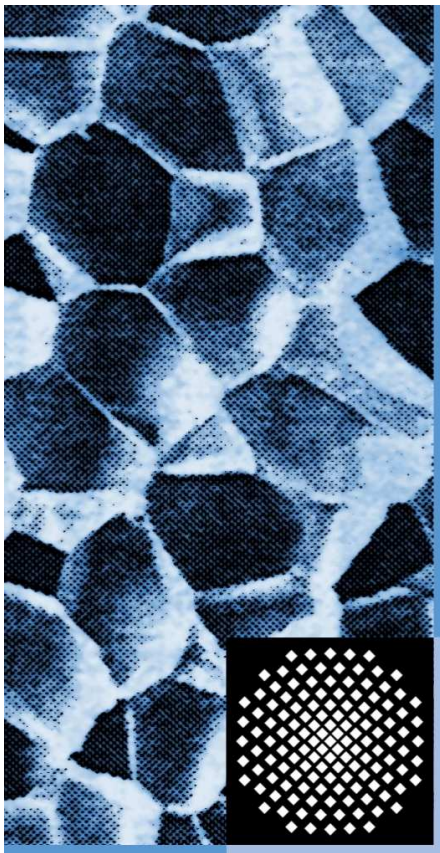

Universität Stuttgart
Germany

Institut für Mechanik (Bauwesen)
Lehrstuhl für Kontinuumsmechanik
Prof. Dr.-Ing. W. Ehlers

Proceedings of the
3rd GAMM Seminar on

Continuum Biomechanics

W. Ehlers & B. Markert (Eds.)

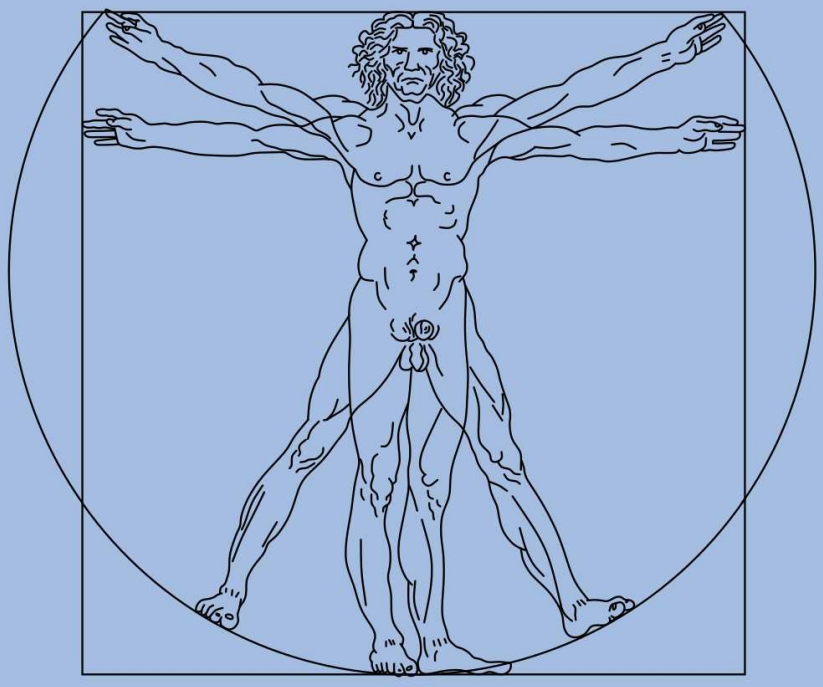

Report No.: II-21 (2012)

Proceedings
of the 3rd GAMM Seminar on

Continuum Biomechanics

W. Ehlers & B. Markert (Eds.)

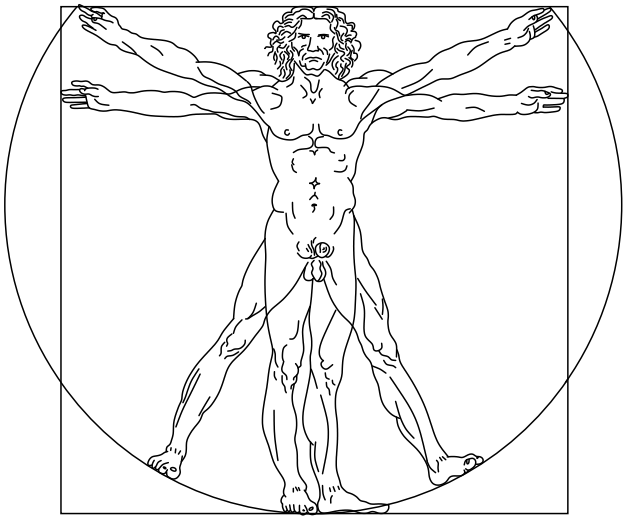

Report No. II-21

Institute of Applied Mechanics (CE)
Chair of Continuum Mechanics
University of Stuttgart
2012

Report No. II-21
Institut für Mechanik (Bauwesen)
Lehrstuhl für Kontinuumsmechanik
Universität Stuttgart, Germany, 2012

Editors:

Prof. Dr.-Ing. W. Ehlers
PD Dr.-Ing. B. Markert

Druck mit freundlicher Unterstützung der

LB≡BW
Stiftungen
Landesbank Baden-Württemberg

ISBN 978–3–937399–21–6

Preface

The 3rd GAMM Seminar on Continuum Biomechanics took place November 24 – 26, 2010, in Freudenstadt-Lauterbad, Germany. It was organised by the Biomechanics Activity Group under the auspices of the International Association of Applied Mathematics and Mechanics (GAMM), which promotes scientific development in all areas of applied mathematics and mechanics. The Seminar venue was the Waldhotel Zollernblick in the climatic spa Freudenstadt-Lauterbad located in the Black Forest region, Germany.
The GAMM Biomechanics Activity Group was formed on October 23, 2003, in Stuttgart with the major objective to foster the interest in biomechanical problems in the German-speaking area in order to keep pace with international developments. After two previous GAMM Seminars on Continuum Biomechanics in 2004 and 2006, the actual Seminar was the third major initiative of the Activity Group providing a discussion forum on the recent advances in theoretical, numerical, and experimental techniques in the broad field of biomechanical engineering with special focus on soft and hard biological tissues. The informal nature of the Seminar offered the opportunity to openly exchange scientific ideas, where the welcoming atmosphere of the Waldhotel Zollernblick with an exceptional view on the Swabian Alb furthermore contributed to its overall success. In particular, exposed problems of continuum and computational biomechanics as well as mechanobiology have been presented in 19 oral presentations, out of which 7 extended contributions are published in this Proceedings Volume. Since the organisers are confident that such Seminars help to manifest and to enlarge the biomechanics community in Germany, we aim at continuing the successful GAMM Seminar Series on Continuum Biomechanics.
Finally, we would like to express our thanks to the sponsors of the Seminar, namely LBBW-Stiftungen, Cluster of Excellence (EXC 310) on Simulation Technology and GAMM. The financial support allowed us to schedule two invited presentations of renown scientists, to publish this volume of Proceedings, and last but not least to keep the registration fee low, so that, in particular, younger researchers had the possibility to participate. The organisation and execution of the Seminar as well as the preparation of the Proceedings Volume was performed by the staff of the Institute of Applied Mechanics (CE) of the University of Stuttgart. Also their extremely valuable help is herewith most gratefully acknowledged.

Stuttgart, November 2012

Wolfgang Ehlers

Bernd Markert

Contents

A Finite Element Approach for Modelling Synovial Joint Contact

K. Fietz & U. Nackenhorst

Institut für Baumechanik und Numerische Mechanik,
Leibniz Universität Hannover, 30167 Hannover, Germany

Abstract. In this contribution a computational approach for modelling hip joint contact is outlined. A contact element for describing the synovial fluid in interaction with the cartilage layers is developed. The fluid description is based on the stationary Stokes flow equations. A discretisation with Taylor Hood elements is applied. Geometrically the synovial gap is modelled as the midsurface between the cartilage layers. The thickness of this liquid interface layer varies over the area. Due to the curvature of the shell-like midsurface convective coordinates are introduced.
The fluid structure interaction is solved by a staggered contact algorithm. During the iteration the solid displacements lead to changes of the thickness distribution of the articular gap. Source terms are introduced into the fluid formulation in order to handle these thickness changes. The joint capsule prevents the synovial fluid from leaving the joint space. Therefore a fluid structure interaction problem with a fully enclosed fluid has to be solved. An artificial compressibility method is applied for this purpose.
The proposed algorithm and the liquid contact element are validated by suitable numerical examples. An outlook on the application of these elements in a three dimensional finite element model of the hip joint is given.

1 Introduction

In synovial joints the bone surfaces are covered with articular cartilage layers. The joint is surrounded by the joint capsule which is filled with synovial fluid. As the cartilage is not supplied with blood vessels the tissue is nourished by the synovial fluid. The synovia can be imbibed into and pressed out of the cartilage, thus establishing a fluid exchange between cartilage and synovial gap. In the healthy joint the synovial fluid creates a thin fluid film between the cartilage surfaces preventing them from direct contact and leading to a very low friction contact ([5, 11]).
Osteoarthritis is one of the most frequently occurring joint diseases. Particularly the hip joint is affected by this degeneration of cartilage and subchondral bone. Due to the absence of nerves in the cartilage tissue the cartilage deterioration can proceed widely without causing pain, so that many patients are only diagnosed with the disease in an advanced stage. This is one of the reasons why the origin and early progress of degeneration still remain unknown. It is however a widely accepted theory that too high local cartilage stresses lead to osteoarthritis ([10, 20]).

An overview of previous numerical modelling approaches for the hip joint is given in [17].
Finite element analyses have often been conducted for two dimensional geometries using plain strain assumptions ([4, 8, 21–23]). Geometric simplifications are also common in three dimensional analyses of the hip joint. In several studies a rigid body spring model or discrete element analysis has been applied with the argument that a finite element analysis would be too complex ([9, 13, 24]). In these models the bone parts were considered to be rigid and contact was modelled using a normal and a shear spring in each element. In numerical investigations with different objectives it is however state of the art to reconstruct very detailed geometries from CT-data ([1, 6]) and even to proceed towards physiological boundary conditions and subject specific analysis ([18]). In numerical hip joint contact analysis only very few authors have applied realistic three dimensional geometries. Even in these more detailed three dimensional models for hip joint contact ([2], [16]) no physiological contact conditions have been simulated. [2] used a linear elastic material law for the cartilage layers, the synovial fluid and joint capsule have not been taken into account. [16] only regarded the acetabular cartilage in contact with a rigid body. A physiological hip joint contact model incorporating the hydrodynamic behaviour of the cartilage layers on both sides in interaction with the synovial fluid in the articular gap does not yet exist.
Our research is focused on developing a hip joint contact model which includes the fluid flow within the articular gap as well as the fluid exchange and nutrient transport between the synovial gap and the cartilage layers.
In this contribution an interface element for describing the contact conditions in synovial joints is proposed. The development of a suitable element is based on the stationary Stokes flow equations for incompressible viscous flow. A staggered contact algorithm for solving the fluid structure interaction problem is presented. The ability of the developed element to model the fluid behaviour correctly is demonstrated by numerical examples.

2 Modelling Approach

2.1 The Overall Computational Framework

As described above the aim of this research is the analysis of the physiological contact conditions in the human hip joint using a three dimensional finite element model. The contact partners in the hip joint are the cartilage layers and the synovial fluid. Apart from these contact partners the relevant osseous structures are also included in the model. The bones involved in the hip joint are the pelvic bone and the femur. The geometries of the femoral head and the pelvic bone are reconstructed from CT-data. From the male dataset of the Visible Human Project®[1] 200 CT-images covering the proximal femur

[1] http://www.nlm.nih.gov/research/visible/visible_human.html

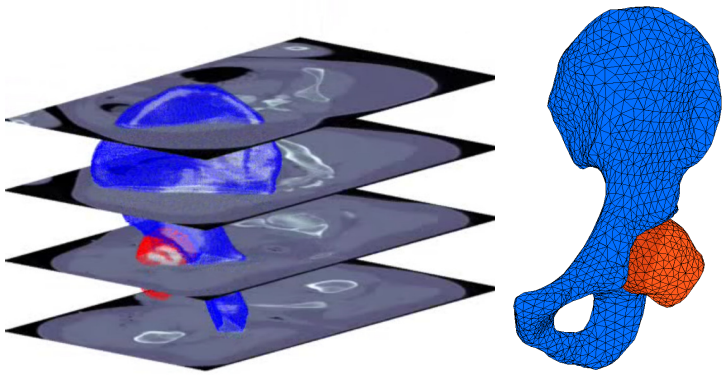

Fig. 1. Three dimensional finite element modelling approach of the hip joint. left: geometry reconstruction from CT-data, right: finite element model

and the pelvic bone with a pixel distance of $1mm$ and a slice thickness of $1mm$ were used. In each CT-image the silhouettes of the osseous structures were identified. A three-dimensional geometry description is then obtained from these two-dimensional outlines. This geometry reconstruction process is illustrated in Figure 1. The bone geometries are discretised with linear tetrahedral elements (see Figure 1). The cartilage layers will be modelled as a fluid saturated porous medium ([15]). The cartilage surfaces will be approximated by quadratic shape functions.
The gap between the cartilage layers of the femoral head and the acetabulum is filled with synovial fluid. For the contact model it is important to describe the interaction between the synovial fluid in the articular gap and the cartilage layers. As the synovial fluid constitutes only a very thin fluid film a shell-like midsurface representation is chosen to describe the fluid domain geometrically. This midsurface description will also contribute to an efficient treatment of the rotation of the femoral head. In order to account for the incongruence of the femoral head and the acetabulum the thickness varies over the midsurface area. Applying the stationary Stokes flow equations the fluid flow in the articular gap is described as an incompressible viscous flow. The synovial fluid is modelled as a Newtonian fluid.
A staggered contact algorithm is used to compute the fluid cartilage interaction.

2.2 Finite Element Approach for the Liquid Interface Layer Cartilage Contact

The synovial gap is represented by a midsurface between the cartilage layers. In the following, different coordinate systems are used. These are presented in Figure 2. Apart from the global Cartesian coordinate system $\mathbf{e}_i$, a convective

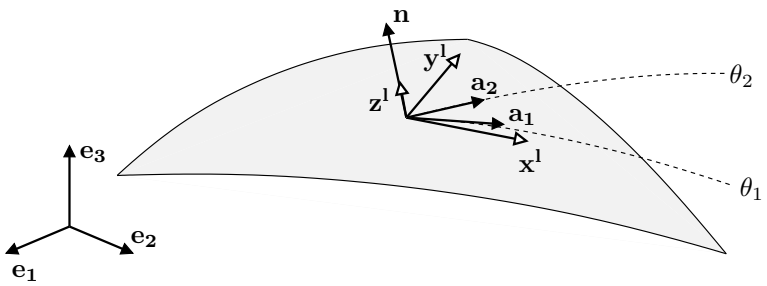

Fig. 2. Coordinate systems

basis $[\mathbf{a}_1\ \mathbf{a}_2\ \mathbf{n}]$ is given. In this coordinate system $\mathbf{a}_i$ are tangent vectors to the curvilinear coordinates θ_i. The normal direction $\mathbf{n}$ is interpolated from normal directions at the element nodes in order to ensure a C^0-smooth normal field over the whole midsurface. The normal directions at the nodes are determined in the construction process of the midsurface.
From this skew basis $[\mathbf{a}_1\ \mathbf{a}_2\ \mathbf{n}]$ a local orthogonal basis $[\mathbf{x^l}\ \mathbf{y^l}\ \mathbf{z^l}]$ with coordinates x^l, y^l, z^l can be constructed as follows

$$\mathbf{z^l} = h\mathbf{n}\,, \tag{1}$$

$$\mathbf{y^l} = \frac{\mathbf{n}\times\mathbf{a}_1}{||\mathbf{n}\times\mathbf{a}_1||}\,, \tag{2}$$

$$\mathbf{x^l} = \frac{\mathbf{y^l}\times\mathbf{n}}{||\mathbf{y^l}\times\mathbf{n}||}\,. \tag{3}$$

In this local basis the normal direction $\mathbf{n}$ is scaled with the element thickness h which is important in the following.
The midsurface is generated by executing an orthogonal projection of each node, belonging to the acetabular cartilage surface, onto the femoral cartilage surface. In the middle of the distance between the acetabular node and its projection point a node of the midsurface is created. Element connectivity on the midsurface is thus an image of the element connectivity of the acetabular surface. The projection direction defines the normal direction $\mathbf{n}$ at each node of the midsurface. Due to the projection process the thickness h is given at each node of the element so that it can be interpolated quadratically

$$h = \mathbf{N}_h\hat{\mathbf{h}}\,. \tag{4}$$

This midsurface element with variable thickness is illustrated in Figure 3.
The volume V of the fluid domain is obtained by integrating the thickness h over the midsurface area Γ

$$V = \int_\Omega \mathrm{dV} = \int_\Gamma h\ \mathrm{d}\Gamma\,. \tag{5}$$

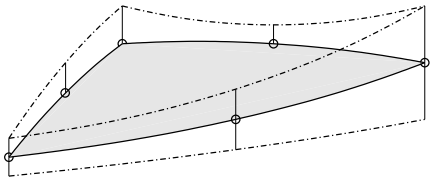

Fig. 3. 6-node-triangular midsurface element with variable thickness h

The fluid behaviour is described by the stationary Stokes equations for incompressible viscous flow,

$$\operatorname{div}(\boldsymbol{\sigma}) = 0\,, \tag{6}$$
$$\operatorname{div}(\mathbf{v}) = 0\,. \tag{7}$$

Equation (6) describes the balance of momentum with the Cauchy stress tensor $\boldsymbol{\sigma}$, where body forces have been neglected. Equation (7) describes the mass balance with the spatial velocity field $\mathbf{v}$. The stress tensor splits into a volumetric part characterised by the hydrostatic pressure p and a deviatoric part $\mathbf{s}$ defined by Stokes law,

$$\boldsymbol{\sigma} = \mathbf{s} - p\mathbf{I}\,, \tag{8}$$
$$\mathbf{s} = 2\mu\ \operatorname{grad}^{\mathrm{sym}}(\mathbf{v})\,. \tag{9}$$

The constitutive parameter μ is known as dynamic viscosity. A standard Galerkin mixed formulation is used to derive the weak form of the Stokes problem,

$$\int_\Omega \operatorname{grad}(\delta\mathbf{v}) : \mathbf{s}\ \mathrm{dV} - \int_\Omega p\ \operatorname{div}(\delta\mathbf{v})\ \mathrm{dV} = \int_{\partial\Omega} \delta\mathbf{v}\cdot\mathbf{t}\ \mathrm{dA}\,, \tag{10}$$
$$\int_\Omega \delta p\ \operatorname{div}(\mathbf{v})\ \mathrm{dV} = 0\,. \tag{11}$$

The Stokes problem has to be solved on the curved midsurface and therefore it is formulated with respect to the local coordinates $x_i = x^l, y^l, z^l$.
In the above equations the gradient is evaluated as the covariant derivative

$$\operatorname{grad}(\mathbf{v}) = \frac{d(v^l)^k}{d(x^l)_i} + (v^l)^j \Gamma^k_{ji}\,. \tag{12}$$

In Equation (12) v^l denotes the components of $\mathbf{v}$ with respect to the convective orthogonal basis $[\mathbf{x^l}\ \mathbf{y^l}\ \mathbf{z^l}]$. Γ^k_{ji} denote the Christoffel symbols which are defined as

$$\Gamma^k_{ji} = \frac{1}{2} g^{kn}(g_{in,j} + g_{jn,i} - g_{ji,n}) \tag{13}$$

with the components of the contravariant metric g^{kn} and the derivatives of the covariant metric $g_{in,j}$. The covariant metric is given by

$$g_{ij} = \begin{bmatrix} \mathbf{x}^l \cdot \mathbf{x}^l & \mathbf{x}^l \cdot \mathbf{y}^l & \mathbf{x}^l \cdot \mathbf{z}^l \\ \mathbf{y}^l \cdot \mathbf{x}^l & \mathbf{y}^l \cdot \mathbf{y}^l & \mathbf{y}^l \cdot \mathbf{z}^l \\ \mathbf{z}^l \cdot \mathbf{x}^l & \mathbf{z}^l \cdot \mathbf{y}^l & \mathbf{z}^l \cdot \mathbf{z}^l \end{bmatrix} . \tag{14}$$

As the basis is orthogonal and $\mathbf{x}^l$ and $\mathbf{y}^l$ are of unit length the metric is of the following structure

$$\mathbf{g} = \begin{bmatrix} 1 & 0 & 0 \\ 0 & 1 & 0 \\ 0 & 0 & h^2 \end{bmatrix} , \tag{15}$$

so that only the Christoffel symbols Γ^1_{33}, Γ^2_{33}, Γ^3_{13}, Γ^3_{23}, Γ^3_{31} and Γ^3_{32} have values which are not equal to zero.
A geometric interpretation for the scaling of the normal vector with the thickness h can be given. The first term in Equation (12) can be interpreted as in-plane gradient, while the second term can be expressed as

$$(v^l)^j \Gamma^k_{ji} = \frac{1}{h} \mathbf{v} \otimes \mathrm{grad}(h) . \tag{16}$$

This result is explained by considering the infinitesimal volume element illustrated in Figure 4. The inflow at x has to equal the outflow at $x + dx$

$$\mathbf{v}(x) A(x) = \mathbf{v}(x + dx) A(x + dx) \tag{17}$$

leading to

$$\frac{d\mathbf{v}}{dx} = -\frac{\mathbf{v}(x)}{h(x)} \frac{dh}{dx} , \tag{18}$$

which can be expressed by Equation (16) for the three dimensional case. The scaling of the normal vector with the thickness therefore ensures fulfilling the mass balance in elements with a variable thickness.
The equations are solved by the finite element method for which they are written in terms of global Cartesian coordinates. A transformation from global

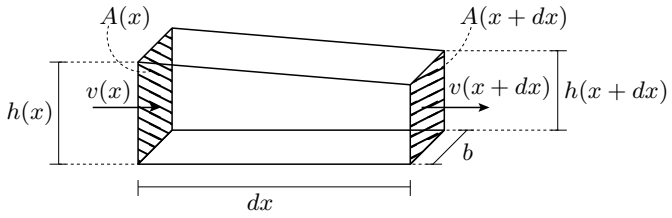

Fig. 4. Infinitesimal volume element

velocity components to local velocity components is given by

$$\mathbf{v}^l = \underbrace{\left[\mathbf{x}^l\ \mathbf{y}^l\ \mathbf{n}\right]^T}_{\mathbf{T}} \mathbf{v}^{gl}\,. \tag{19}$$

Using Equation (19) the velocity gradient from Equation (12) can be written as

$$\mathrm{grad}(\mathbf{v}) = \frac{d\ (T_{km}(v^{gl})^m)}{d(x^l)_i} + T_{mj}(v^{gl})^j \Gamma^k_{mi}\,. \tag{20}$$

The velocity field $\mathbf{v}$, its test function $\delta\mathbf{v}$, the geometry $\mathbf{x}$ and the element thickness h are approximated using quadratic shape functions N_v. The pressure field p and its test function δp are approximated using linear shape functions N_p. This choice corresponds to the classical P2/P1-Taylor-Hood-element ([3, 7, 12]). The discretised formulation reads

$$\begin{bmatrix}\mathbf{K}_{vv} & \mathbf{K}_{vp}\\ \mathbf{K}_{pv} & \mathbf{0}\end{bmatrix}\begin{bmatrix}\hat{\mathbf{v}}_f\\ \hat{\mathbf{p}}_f\end{bmatrix} = \begin{bmatrix}\mathbf{0}\\ \mathbf{0}\end{bmatrix} \tag{21}$$

with

$$\mathbf{K}_{vv} = \int_\Omega \mathbf{B}_v^T (2\mu\mathbf{I}_0)\mathbf{B}_v\ \mathrm{dV}\,, \tag{22}$$

$$\mathbf{K}_{vp} = -\int_\Omega \mathbf{S}_v^T \mathbf{N}_p\ \mathrm{dV}\,, \tag{23}$$

$$\mathbf{K}_{pv} = \mathbf{K}_{vp}^T\,. \tag{24}$$

The diagonal matrix $\mathbf{I}_0$ ensures the correct treatment of symmetries in Voigt notation.

2.3 Contact Algorithm

For solving the fluid solid interaction problem a staggered approach is chosen. Starting with an initial solid geometry $\mathbf{x}_s^0$ the initial midsurface $\mathbf{x}_f^0$ is generated having an initial thickness information h^0. In each iterative step, first the fluid problem is solved for the velocity field $\mathbf{v}_f$ and the pressure distribution $\mathbf{p}_f$. The fluid tangent matrix $\mathbf{K}_f$ and the force vector $\mathbf{f}_f$ are functions of the change in thickness Δh which is a function of the solid displacements $\mathbf{u}_s$ computed in the last iterative step

$$\mathbf{K}_f\left(\Delta h(\mathbf{u}_s^n)\right)\mathbf{u}_f^{n+1} = \mathbf{f}_f\left(\Delta h(\mathbf{u}_s^n)\right) \tag{25}$$

with

$$\mathbf{u}_f = \begin{bmatrix}\mathbf{v}_f\\ \mathbf{p}_f\end{bmatrix}. \tag{26}$$

For the solution of the solid domain contact forces $\mathbf{f}_c$ are computed from the fluid pressure p_f

$$\hat{\mathbf{f}}_c = -\int_{\partial\Omega_s} \mathbf{N}_s^T p_f \mathbf{n}_s \, \mathrm{dA}_s \,. \tag{27}$$

These contact forces are assumed to act in the negative direction of the normal vector $\mathbf{n}_s$ on the cartilage surface A_s. For non matching meshes the integration points are orthogonally projected onto the midsurface and p_f is determined in the projection point. The incremental change of solid deformation $\Delta\mathbf{u}_s$ is solved by

$$\mathbf{K_T}_s^{n+1} \Delta\mathbf{u}_s^{n+1} = \mathbf{f}_{ext} + \mathbf{f}_c^{n+1}(p_f^{n+1}) - \mathbf{f}_{int} \,, \tag{28}$$

$$\mathbf{u}_s^{n+1} = \mathbf{u}_s^n + \Delta\mathbf{u}_s^{n+1} \,. \tag{29}$$

The iteration is stopped if $\|\Delta\mathbf{u}_s\| \leq \epsilon$.
During this iteration the deformation of the solid domain leads to a change of the thickness distribution in the synovial gap. Additional effort is spent to ensure the balance of mass when the thickness is changed. The change of mass can generally be expressed as

$$\Delta m = \Delta \int_\Omega \rho \mathrm{dV} = \int_\Omega \Delta\rho + \rho \mathrm{div}(\mathbf{v}) \, \mathrm{dV} + \int_\Omega \rho \, \Delta \mathrm{dV} = 0 \,. \tag{30}$$

For an incompressible fluid there is no change in density ($\Delta\rho = 0$). Assuming that the area Γ does not change but only the thickness changes, a change in volume can be expressed as $\int_\Omega \Delta \mathrm{dV} = \int_\Gamma \Delta h \mathrm{d}\Gamma$ leading to

$$\int_\Omega \mathrm{div}(\mathbf{v}) \mathrm{dV} + \int_\Gamma \Delta h \mathrm{d}\Gamma = 0 \,. \tag{31}$$

This additional contribution to the mass balance can be interpreted as a source term. The surface integral is transformed into a volume integral by relation (5). The mass balance then reads

$$\int_\Omega \mathrm{div}(\mathbf{v}) \, \mathrm{dV} = -\int_\Omega \frac{\Delta h}{h} \, \mathrm{dV} \,. \tag{32}$$

This modified formulation of the mass balance also has consequences for the transport theorem. In its modified form this is now written as

$$\frac{\mathrm{d}}{\mathrm{dt}} \int_\Omega \rho\psi \mathrm{dV} = \int_\Omega \left(\rho \frac{d\psi}{dt} - \psi\rho \frac{\Delta h}{h} \right) \mathrm{dV} \,. \tag{33}$$

The balance of momentum is changed accordingly and can now be rewritten as

$$\int_\Omega \mathbf{v}\rho \frac{\Delta h}{h} \mathrm{dV} + \int_\Omega \mathrm{div}(\boldsymbol{\sigma}) \mathrm{dV} = 0 \,. \tag{34}$$

From that, an additional contribution $\mathbf{f}_{p,\Delta V}$ to the right hand side arises from the mass balance and an additional contribution $\mathbf{K}_{vv,\Delta V}$ to the tangent matrix results from the balance of momentum

$$\begin{bmatrix} \mathbf{K}_{vv} + \mathbf{K}_{vv,\Delta V} & \mathbf{K}_{vp} \\ \mathbf{K}_{pv} & \mathbf{0} \end{bmatrix} \begin{bmatrix} \hat{\mathbf{v}} \\ \hat{\mathbf{p}} \end{bmatrix} = \begin{bmatrix} \mathbf{0} \\ \mathbf{f}_{p,\Delta v} \end{bmatrix} \tag{35}$$

with

$$\mathbf{K}_{vv,\Delta V} = -\int_{\Omega} \mathbf{N}_v^T \left(\rho \frac{\Delta h}{h} \right) \mathbf{N}_v \, \mathrm{dV} \,, \tag{36}$$

$$\mathbf{f}_{p,\Delta V} = \int_{\Omega} \mathbf{N}_p^T \left(\frac{\Delta h}{h} \right) \, \mathrm{dV} \,. \tag{37}$$

2.4 Artificial Compressibility

Due to the solid displacements not only the thickness distribution but also the overall volume of the synovial gap is changed so that fluid would have to flow out of the domain if the joint space is reduced. In the real joint the synovial gap is enclosed by the joint capsule and its enforcing ligaments so that the fluid cannot flow out of the joint. Therefore hip joint contact is a fluid structure interaction problem with a fully enclosed fluid. This kind of problem cannot be treated with the simple staggered scheme outlined above because the solid deformations violate the fluid's incompressibility condition. This problem is described by [14] and [19] in detail. One possibility to solve such problems with fully enclosed fluids is to introduce an artificial compressibility which vanishes during the iteration. This procedure is described in [19]. Applying this method the mass balance is modified as follows

$$\int_{\Omega} \mathrm{div}(\mathbf{v}) \, \mathrm{dV} + \int_{\Omega} c p^{n+1} \, \mathrm{dV} = -\int_{\Omega} \frac{\Delta h}{h} \, \mathrm{dV} + \int_{\Omega} c p^{n} \, \mathrm{dV} \,, \tag{38}$$

where c is the artificial compressibility parameter and n is the iteration step. The discretised equations now have the form

$$\begin{bmatrix} \mathbf{K}_{vv} + \mathbf{K}_{vv,\Delta V} & \mathbf{K}_{vp} \\ \mathbf{K}_{pv} & \mathbf{K}_{pp,c} \end{bmatrix} \begin{bmatrix} \hat{\mathbf{v}} \\ \hat{\mathbf{p}}^{n+1} \end{bmatrix} = \begin{bmatrix} \mathbf{0} \\ \mathbf{f}_{p,\Delta V} + \mathbf{f}_{p,c} \end{bmatrix} \tag{39}$$

with

$$\mathbf{K}_{pp,c} = -\int_{\Omega} \mathbf{N}_p^T \, c \, \mathbf{N}_p \, \mathrm{dV} \,, \tag{40}$$

$$\mathbf{f}_{p,c} = -\int_{\Omega} \mathbf{N}_p^T \, c p^n \mathrm{dV} \,. \tag{41}$$

It is iterated until $p^{n+1} = p^n$ so that the artificial compressibility has no effect at the end of the iteration.

The described finite element approach for the contact in synovial joints has been implemented into the in-house MatLab based finite element development environment and was verified by various numerical tests, described below.

3 Numerical Examples

In the following, numerical examples are presented which verify the computational approach described above. The observation of the mass balance is shown for curved elements with variable thickness. The functionality of the source terms accounting for changes of the thickness distribution is demonstrated and the effect of the artificial compressibility method is illustrated. The constitutive parameters of the fluid are chosen as $\rho = 10^{-9}\frac{Ns^2}{mm^4}$ and $\mu = 10^{-9}\frac{Ns}{mm^2}$ in the examples of this section. Results for velocity fields are illustrated as vector plots. The arrows point in the direction of the flow and the lengths of the arrows as well as the colour code indicate the magnitude of the velocity vectors.

The first example is chosen in order to verify the conservation of mass in curved elements with variable thickness (see section 2.2). A quarter of a cylinder surface is analysed (see Figure 5). The thickness varies linearly from $0.1mm$ to $0.05mm$ in the circumferential direction (see Figure 5 *a*)). An inflow of $1mm/s$ is prescribed in the circumferential direction. This leads to an outflow of $2mm/s$ which is shown in the velocity field in Figure 5 *b*). Comparing the inflow of $1mm/s$ over an area of $1mm \times 0.1mm$ to the outflow of $2mm/s$ over an area of $1mm \times 0.05mm$ this result proves that the developed curved element satisfies the mass balance in the case of a varying thickness.

In a second example the source terms developed in section 2.3 are verified. A hemispherical surface with a radius of $3mm$ and an initial thickness of $1mm$ is considered (see Figure 6). The thickness is reduced to $0.5mm$ so that the gap volume is reduced by $9\pi\frac{mm^3}{s}$. The fluid is squeezed out over an area of $6\pi mm \times 0.5mm$. An outflow velocity of $3mm/s$ can be observed in Figure 6 so that the outflow corresponds to the displaced volume.

The artificial compressibility method is tested in the third example. Two elastic blocks with a size of $1mm \times 1mm \times 0.5mm$ and a distance of $0.1mm$ are considered. These blocks and the planar midsurface between them are sketched in Figure 7 *a*). The discretisation of the midsurface is shown in Figure 7 *b*). The upper block is displaced downwards by $0.01mm$ so that the change of midsurface thickness Δh is $0.01mm$ (see Figure 7 *c*)). This is the starting point for an iteration in which the fluid finds its initial volume again by developing pressure and thus deforming the two elastic blocks. The situation at the end of this iteration is depicted in Figure 7 *d*). In this simple linear example the pressure needed for obtaining the initial gap volume is known in advance. For the two blocks Hooke's law can be applied

$$p = E\frac{\Delta t}{t_0}\,. \tag{42}$$

With a Young's modulus $E = 15\frac{N}{mm^2}$ an initial block thickness $t_0 = 0.5mm$ and a block displacement $\Delta t = \frac{1}{2}\Delta h = 0.005mm$ the pressure is determined as $p = 0.15\frac{N}{mm^2}$. The artificial compressibility parameter can be chosen to

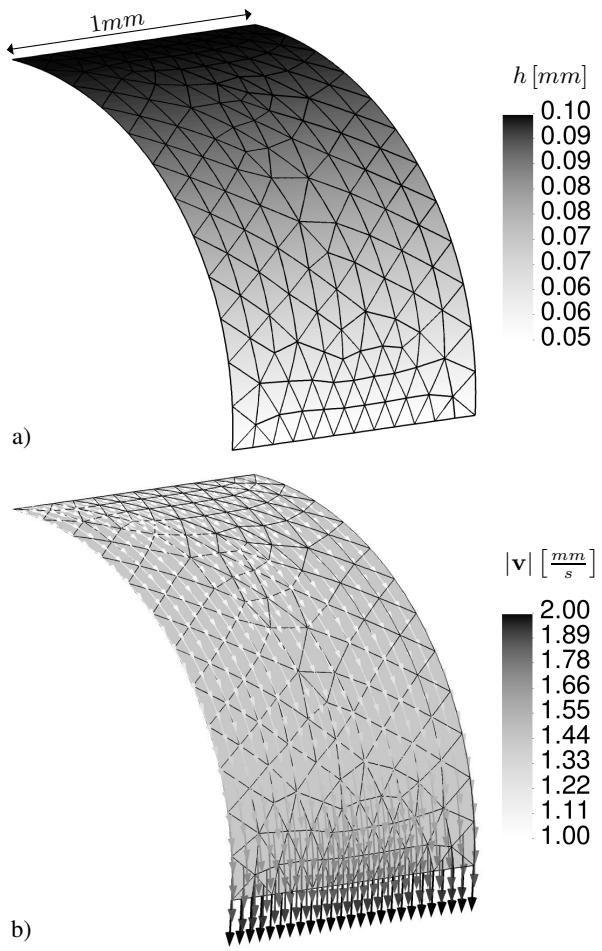

Fig. 5. Verification of mass conservation in curved elements with variable thickness. a) thickness distribution; b) velocity field

solve the problem in one step in this example. Initially $p^n = 0$ so that the mass balance reads

$$\int_\Omega \operatorname{div}(\mathbf{v})\ \mathrm{dV} + \int_\Omega c p^1\ \mathrm{dV} = -\int_\Omega \frac{\Delta h}{h}\ \mathrm{dV}\,. \tag{43}$$

For obtaining the incompressible solution with $\int_\Omega \operatorname{div}(\mathbf{v})\ \mathrm{dV} = 0$ the artificial compressibility parameter c has to be chosen as

$$c = \frac{2t_0}{Eh}\,. \tag{44}$$

For the planned hip joint model with porous cartilage layers the artificial compressibility parameter might not be determined so easily. In order to show

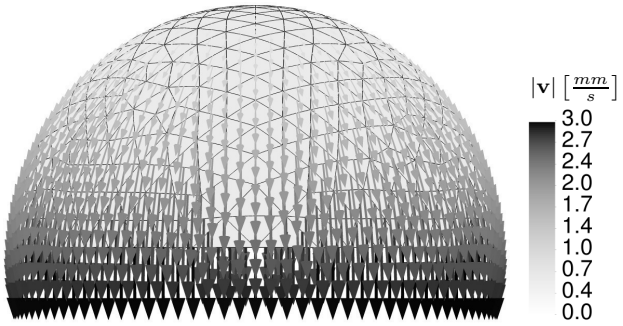

Fig. 6. Verification of source terms. Fluid velocity field

the convergence behaviour for a case in which the ideal value for c is not known the problem described above is computed with an artificial compressibility parameter which differs from the ideal value by 10% ($c = 1.1\frac{2t_0}{Eh}$). The development of the gap volume, the pressure and the stop criterion during the iteration are depicted in Figure 8. The iteration was stopped when

$$\max(|p^{n+1} - p^n|) \leq 10^{-7}\frac{N}{mm^2}\,. \tag{45}$$

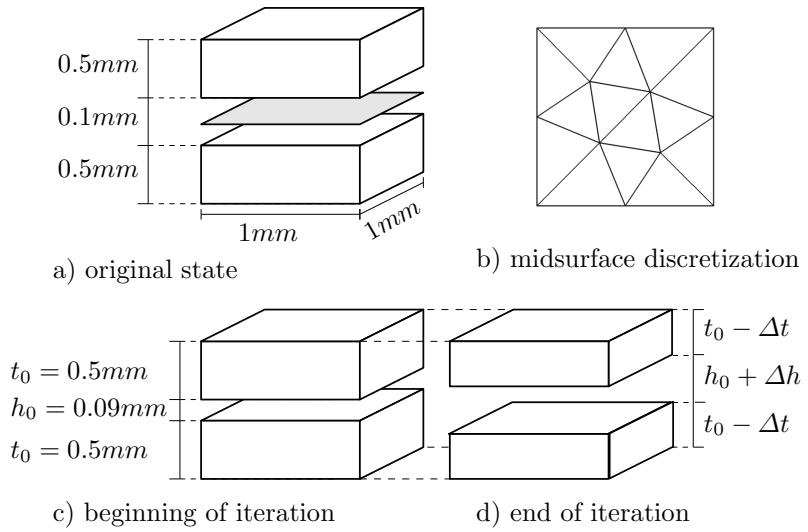

Fig. 7. Application of the artificial compressibility method. a)two blocks with their midsurface in the original state; b) discretisation of the midsurface; c) state at the start of the iteration after the upper block has been displaced; d) state at the end of the iteration where the gap has the same size as in the original state and the blocks have deformed

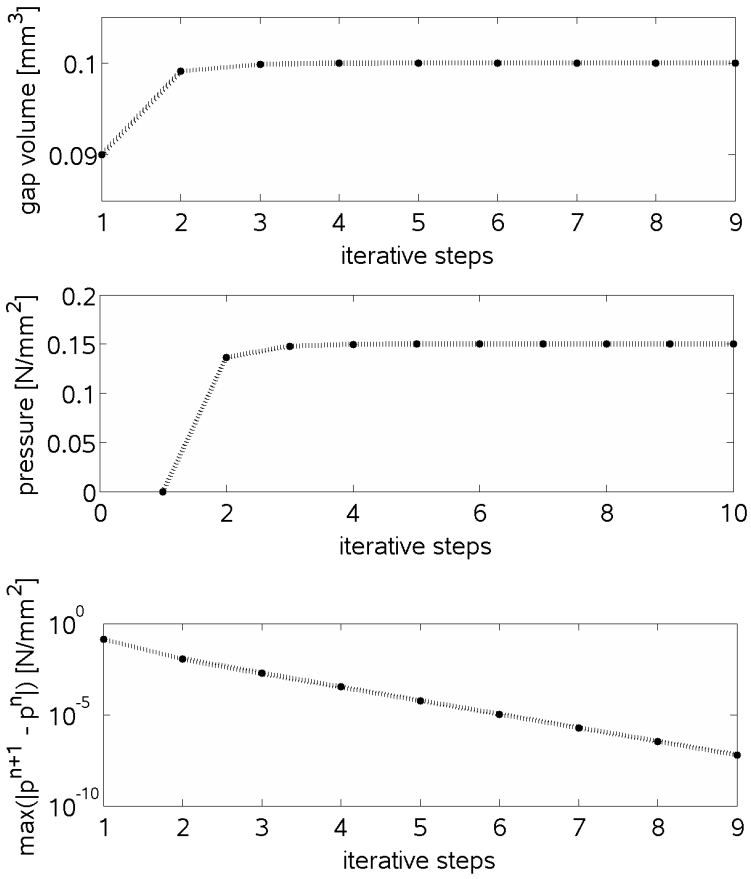

Fig. 8. Application of the artificial compressibility method. a) development of the gap volume; b) development of the pressure; c) development of the criterion on logarithmic scale

In Figure 8 it can be observed that the gap volume converges to its original value of $0.1mm^3$ and that the pressure converges to the analytically determined value of $0.15\frac{N}{mm^2}$.

4 Conclusions and Outlook

In this paper a contact element developed for the contact analysis in synovial joints is outlined. The midsurface between the cartilage layers is chosen to geometrically represent the synovial gap and the synovial fluid. The thickness of the synovial gap varies over this surface. The description of the synovial fluid as an incompressible viscous fluid is based on the stationary Stokes flow equations. As the problem is solved on a curved surface convective coordi-

nates are introduced. The convective normal vector is scaled with the local thickness. This scaling leads to the mass balance being fulfilled even if the thickness varies over the domain.
The contact algorithm consists of a staggered iteration scheme for solving the fluid structure interaction problem. Within this iteration the computed solid displacements change the thickness distribution of the fluid domain. In order to account for these thickness changes, source terms representing the corresponding displaced volume are introduced.
The joint capsule prevents the fluid from flowing out of the synovial gap so that a fluid structure interaction problem with a fully enclosed fluid has to be solved. For this purpose an artificial compressibility is introduced which vanishes during the iteration.
For the numerical simulation of hip joint contact a three-dimensional finite element model of the involved osseous structures, namely the femoral head and the pelvic bone was generated. The next step is to include the cartilage layers into the model. The fluid exchange between the synovial gap and the cartilage layers will also be taken into account. The cartilage will therefore be modelled as a fluid saturated porous medium. A contact description incorporating fluid exchange then allows for investigations of nutrient transport in the hip joint.

Acknowledgements. Financial support for this research project is provided by the German Research Foundation (DFG) under Grant NA 330/6-2.

References

[1] Anderson, A. E.; L.Peters, C.; Tuttle, B. D. & Weiss, J. A.: Subject-Specific Finite Element Model of the Pelvis: Development, Validation and Sensitivity Studies. *Journal of Biomechanical Engineering* **127** (2005), 364–373.
[2] Bachtar, F.; Chen, X. & Hisada, T.: Finite element contact analysis of the hip joint. *Medical & Biological Engineering & Computing* **44** (2006), 643–651.
[3] Brezzi, F. & Fortin, M.: *Mixed and Hybrid Finite Element Methods.* Springer-Verlag New York Inc. 1991.
[4] Brown, T. D. & DiGioia, A. M.: A contact-coupled finite element analysis of the natural adult hip. *Journal of Biomechanics* **17** (1984), 437–448.
[5] Chernyakova, Y. M. & Pinchuk, L. S.: The Synovial Joint as an Intelligent Friction Unit. *Journal of Friction and Wear* **28** (2007), 389–394.
[6] Dalstra, M. & Huiskes, R.: Load transfer across the pelvic bone. *Journal of Biomechanics* **28** (1995), 715–724.
[7] Donea, J. & Huerta, A.: *Finite Element Methods for Flow Problems.* John Wiley & Sons Ltd. 2003.

[8] Ferguson, S.; Bryant, J.; Ganz, R. & Ito, K.: The influence of the acetabular labrum on hip joint cartilage consolidation: a poroelastic finite element model. *Journal of Biomechanics* **33** (2000), 953–960.

[9] Genda, E.; Konishi, N.; Hasegawa, Y. & Miura, T.: A computer simulation study of normal and abnormal hip joint contact pressure. *Arch Orthop Trauma Surg* **114** (1995), 202–206.

[10] Hassett, G. & Spector, T. D.: Osteoarthritis. The Medicine Publishing Company Ltd. (2002).

[11] Hlaváček, M.: The influence of the acetabular labrum seal, intact articular superficial zone and synovial fluid thixotropy on squeeze-film lubrication of a spherical synovial joint. *Journal of Biomechanics* **35** (2002), 1325–1335.

[12] Hood, P. & Taylor, C.: Navier-Stokes equations using mixed interpolation. In Oden, J. (ed.): *Finite element methods in flow problems*, UAH Press 1974, pp. 121–132.

[13] Kumagai, M.; Kim, Y.; N.Inoue; Genda, E.; Hua, K.; Liong, B.; Koo, T. & Chao, E.: 3-D dynamic hip contact pressure distribution in daily activities. In *2003 Summer Bioengineering Conference, June 25-29, Sonesta Beach Resort in Key Biscayne, Florida*, 2003.

[14] Küttler, U.; Förster, C. & Wall, W. A.: A solution for the incompressibility dilemma in partitioned fluid-structure interaction with pure dirichlet fluid domains. *Computational Mechanics* **38** (2006), 417–429.

[15] Mabuma, J.; Markert, B. & Ehlers, W.: Continuum-mechanical meodelling of hip cartilage under physio-dynamical loading. In *PAMM Proceedings in Applied Mathematics and Mechanics*, 2010, vol. 10, pp. 693–694.

[16] Macirowski, T.; Tepic, S. & Mann, R. W.: Cartilage Stresses in the Human Hip Joint. *Journal of Biomechanical Engineering* **116** (1994), 10–18.

[17] Mackerle, J.: Finite element modeling and simulations in orthopedics: a bibliography 1998 - 2005. *Computer Methods in Biomechanics and Biomedical Engineering* **9** (2006), 149–199.

[18] Phillips, A.; P.Pankaj; Howie, C.; Usmani, A. & Simpson, A.: Finite element modelling of the pelvis: Inclusion of muscular and ligamentous boundary conditions. *Medical Engineering and Physics* **29** (2007), 739–748.

[19] Raback, P.; Ruokolainen, J.; Lyly, M. & Jrvinen, E.: Fluid-structure interaction boundary conditions by artificial compressibility. In *ECCOMAS Computational Fluid Dynamics Conference 2001, Swansea, Wales, UK*, 2001.

[20] Radin, E.; Burr, D.; Caterson, B.; Fyhrie, D.; Brown, T. & Boyd, R.: Mechanical determinants of osteoarthrosis. *Semin Arthritis Rheum [Suppl 2]* **21** (1991), 12–21.

[21] Rapperport, D. J.; Carter, D. D. R. & Schurman, D. J.: Contact finite element stress analysis of the hip joint. *Journal of Orthopaedic Research* **3** (1985), 435–446.

[22] Wei, H.-W.; Sun, S.-S.; Jao, S.-H. E.; Yeh, C.-R. & Cheng, C.-K.: The influence of mechanical properties of subchondral plate, femoral head and neck on dynamic stress distribution of the articular cartilage. *Medical Engineering and Physics* **27** (2005), 295–304.

[23] Wu, J.; Herzog, W. & Epstein, M.: Evaluation of the finite element software ABAQUS for biomechanical modelling of biphasic tissues. *Journal of Biomechanics* **31** (1998), 165–169.

[24] Yoshida, H.; Faust, A.; Wilckens, J.; Kitagawa, M.; Fetto, J. & Chao, E. Y.-S.: Three-dimensional dynamic hip contact area and pressure distribution during activities of daily living. *Journal of Biomechanics* **39** (2006), 1996–2004.

Multiphasic Modelling of Human Brain Tissue with Application to Convection-Enhanced Delivery of Therapeutics

W. Ehlers & A. Wagner

Institute of Applied Mechanics (CE), Chair of Continuum Mechanics,
University of Stuttgart, Pfaffenwaldring 7, 70569 Stuttgart, Germany

Abstract. A convenient constitutive model of the complex brain-tissue aggregate is presented in the framework of the well-established Theory of Porous Media (TPM) which is suitable for various numerical simulations of medical relevance. The continuum-mechanical model bases on an elastically deformable solid constituent, which is provided by the nervous tissue cells and the blood vessel walls. This skeleton is completely permeated by two viscous, materially incompressible pore-liquid constituents, the interstitial fluid and the blood plasma. The liquids are mobile within the solid skeleton and exhibit a significant anisotropic perfusion behaviour which has to be taken into account. Special attention is applied to the so-called convection-enhanced drug delivery which is a modern clinical application in their infancies, where an extra-vascular infusion of therapeutic agents for the effective treatment of malignant brain tumours is carried out. Therefore, the interstitial fluid is treated as a real mixture of a liquid solvent and a dissolved therapeutic solute. Due to the strong coupling of the solid-liquid-transport problem, the resulting set of coupled partial differential equations is spatially discretised using mixed finite elements with an implicit *Euler* time-integration scheme to solve the considered problem in a monolithic manner. The presented numerical accessibility enables the possibility for un-bloody studies concerning the infusion process.

1 Introduction

Without doubt, the brain is one of the most important organs for humans. Its key role as control centre for men is compromised by an amount of brain diseases, such as strokes or cerebral tumours. The occurring irregularities can appear suddenly and often result in life-threatening effects. Therefore, a profound understanding of the complex human brain is of great scientific interest. Due to the fact that the microscopic composition of the nervous brain tissue consists of several different components, it is surprising that the first serious approach to model human brain tissue in the sense of a multi-phase material was only carried out in 2006 by the group of Holzapfel [12]. Therein, the modelling approach of human brain tissue incorporates the compartments of brain tissue and interstitial fluid but neglects the blood constituent. This was sufficient for the considered *in vitro* studies. However, this somehow incomplete approach is commonly used until today even for *in vivo* studies of

human brain tissue. Therefore, an entire modelling approach including also the blood constituent is presented in this contribution in order to describe *in vivo* brain tissue properly. As far as we are aware, this is done here for the first time.
The application of the presented model to an example of medical relevance is motivated by the fact that brain cancer is probably the most serious disease. The treatment of cancer improves, but there is still an urgent clinical need for an advanced therapy of brain tumours such as malignant gliomas. The blood-brain barrier (BBB) effectively separates the delicate brain tissue from the intra-vascular space. Hence, drug delivery to malignant brain tumours via the bloodstream is hindered. Therefore, modern clinical applications proceed from a direct infusion of a solution containing the therapeutic agents in the extra-vascular space of the brain tissue using implanted catheters, which are individually connected to medication pumps. This pioneering method is called convection-enhanced drug delivery (CED) and was first proposed by Bobo *et al.* [5]. In comparison with diffusion-based applications, convection-enhanced technology distributes therapeutic agents to a significantly larger tissue volume, resulting in a greater efficacy [5, 13, 14]. The CED models presented by Smith & Humphrey [20], Chen & Sarntinoranont [7] and Linninger *et al.* [16] includes a lot of main processes during an infusion, but a proper description of the coupling effects and the deformable porous tissue skeleton is missing. The possibility to simulate a simplified infusion process has been provided in the meantime by a commercial surgical planning software (iPlan® Flow, Brainlab, Feldkirchen, Germany, `http://www.brainlab.com`). Hence, the prediction of drug distribution in human brain tissue seems to be achieved. Nevertheless, all investigations up to now have been insufficient to predict the distribution profile of the applied therapeutics adequately. In our opinion, the main reasons for this are the decoupled solution strategies as well as the lack of a proper description of the deformable tissue. These shortcomings will be addressed here in order to build a sound basis for further investigations.

2 Tissue Properties of Human Brain Matter

2.1 Anatomy of the Human Brain

From an anatomical point of view, the cerebrum of the human brain can be macroscopically regarded as an assembly of several lobes. Under the cerebrum, the cerebellum and the brain stem are placed, see Figure 1. In general, the grey matter at the cerebral cortex of the brain encloses the white matter in the inside of the brain. At the right side of Figure 1, one can recognise a part of the inner cavity of the brain, the ventricles, which are filled with cerebrospinal fluid (CSF). Additionally, there is the well branched blood vessel system, which is responsible for an overall oxygen transport to the brain tissue and provides the evacuation of pollutants out of the brain. A microscopic

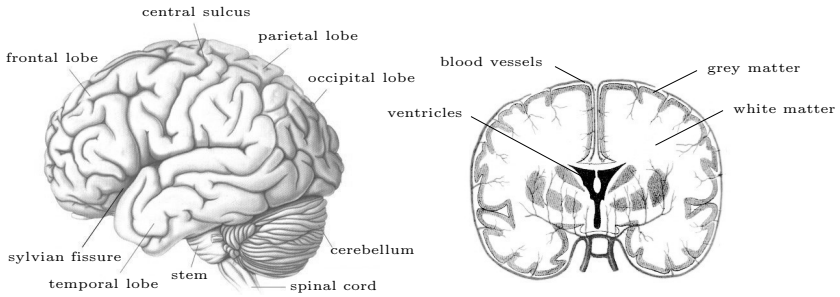

Fig. 1. Geometry of the human brain (left), adapted from Bear *et al.* [4], and frontal cross section (right), adapted from Lippert [17]

view in Figure 2 points out that the cell bodies (nucleus) of the neurons are located in the grey matter, whereas, in the white matter, the myelin sheath of neurons (axons) are found. The permeability of white matter changes in accordance with the directional alignment and density of fibres. Therefore, white matter diffusion is anisotropic and white matter properties are heterogeneous. The permeability in grey matter is almost the same in all directions and can be assumed to be isotropic.

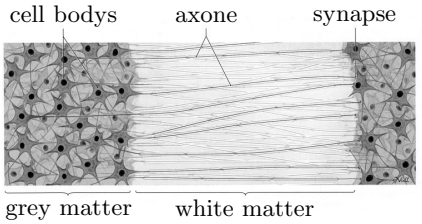

Fig. 2. White and grey matter, adapted from Schünke *et al.* [19]

2.2 General Physical Behaviour of Brain Tissue

Franceschini *et al.* [12] showed with *in vitro* experiments that human brain tissue (samples from the parietal lobe) behaves like a porous fluid-saturated medium. Therefore, a uni-axial strain machine with properly defined draining conditions (free drainage at the bottom and top surface; side surface impermeable and rigid) was used, see Figure 3 (left). The tissue samples are loaded by the stress $q = 8.846\,\mathrm{kN/m^2}$ (corresponding to an external force of 6 N distributed over the top surface). By use of this device, it was possible to distinguish between a viscous behaviour of a single-phase material and an ongoing consolidation process of a multiphase material, see Figure 3 (right). This experiment was recalculated [25] with a biphasic model (bloodless tissue

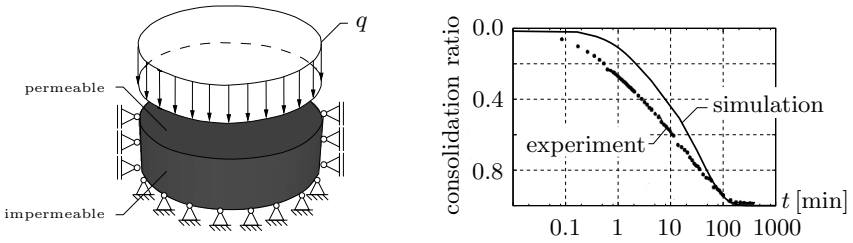

Fig. 3. Boundary conditions (left) and results (right) of the oedometric test

and interstitial fluid) using the finite element software [1]PANDAS in order to survey the general physical behaviour. The vertical displacement u_1 of the top surface rises due to the ongoing consolidation process, see Figure 4 (left). The external stress q causes at first a high effective pressure p^{IR} of the interstitial fluid and is transferred to the solid skeleton by an increase of the solid extra stress $T^S_{E\,11}$ during the efflux of the interstitial fluid on the drained surfaces, see Figure 4 (right).

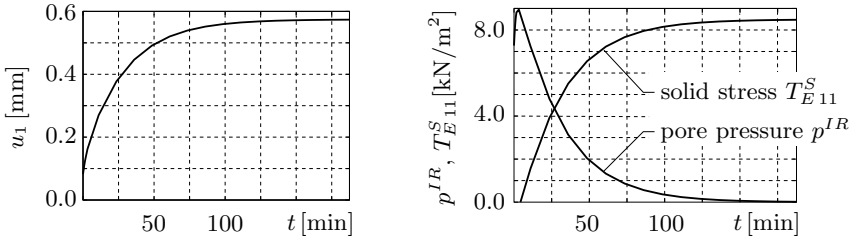

Fig. 4. Displacements on the top surface u_1 (left) and evolution of the interstitial fluid pressure p^{IR} and the solid extra stress $T^S_{E\,11}$ (right)

3 A Biphasic Four-Component Modelling Approach for Human Brain Tissue

3.1 Modelling Concept and Theoretical Fundamentals

Due to the complex and partially unknown local composition of the nervous brain tissue, a continuum-mechanical modelling process based on the well-founded TPM, e. g. Ehlers [9, 10], is absolutely meaningful to describe human brain tissue in a sufficient way. For the issues under consideration, a biphasic four-component model is proposed based on a note of Wagner & Ehlers [26], cf. Figure 5. It consists of an elastically deformable solid skeleton φ^S provided by the tissue cells, which is perfused by two liquid phases, the blood plasma φ^B and the interstitial fluid φ^I. In order to be able to describe the

[1] **P**orous media **A**daptive **N**onlinear finite element solver based on **D**ifferential **A**lgebraic **S**ystems (http://www.get-pandas.com)

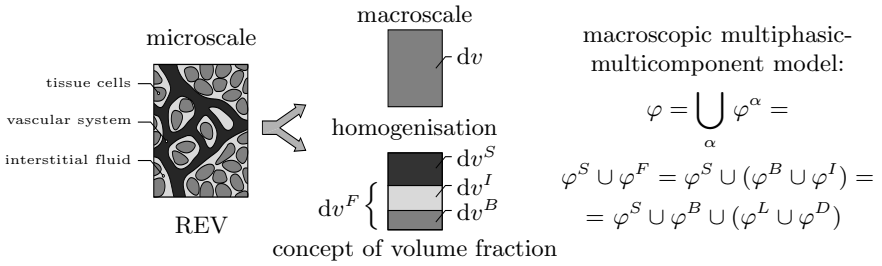

Fig. 5. Representative elementary volume (REV) with exemplary displayed microstructure of brain tissue and multi-phasic modelling approach

distribution process of the inserted therapeutic agent, the interstitial fluid phase is furthermore treated as a real chemical mixture of two components. This solution consists of a liquid solvent φ^L and the dissolved therapeutic solute φ^D.

Immiscible Components and Volume Fractions The homogenisation of the microscopic physical quantities over a representative elementary volume (REV) leads to a model of superimposed and interacting constituents. In order to account for the local compositions of the aggregate, scalar structure parameters, $n^\alpha = \mathrm{d}v^\alpha/\mathrm{d}v$, are introduced according to the concept of volume fractions. The volume fractions n^α of the constituents are defined as the local ratios of the partial volume elements $\mathrm{d}v^\alpha$ with respect to the volume element $\mathrm{d}v$ of the overall aggregate. Assuming fully saturated conditions (no vacant space within the domain) leads to the well-known saturation condition

$$\sum_\alpha n^\alpha = n^S + \underbrace{n^B + n^I}_{n^F} = n^S + n^B + \underbrace{n^L + n^D}_{n^I} = 1\,. \tag{1}$$

Furthermore, saturation-like measures

$$\bar{s}^\xi = \frac{n^\xi}{n^F} \qquad \text{with} \quad \xi = \{B,\, I\} \tag{2}$$

are introduced, describing the volumetric amount n^ξ of a single liquid in comparison to the overall liquid volume fraction n^F. Here, one has to mention that the liquids are not situated in the same pore space, but in the common extracellular space. Therefore, the measures $\bar{s}^\xi$ are not saturations in the classical meaning. In the context of the homogenisation process of porous materials, there are two different densities to be introduced. The realistic (material) density $\rho^{\alpha R} = \mathrm{d}m^\alpha/\mathrm{d}v^\alpha$ is defined by the local mass element $\mathrm{d}m^\alpha$ with respect to its partial volume element $\mathrm{d}v^\alpha$, while the partial density $\rho^\alpha = \mathrm{d}m^\alpha/\mathrm{d}v$ is defined by the local mass element $\mathrm{d}m^\alpha$ divided by the volume element $\mathrm{d}v$ of the overall aggregate. This leads to the dependency

$$\rho^\alpha = n^\alpha \rho^{\alpha R}\,. \tag{3}$$

That means, the property of material incompressibility ($\rho^{\alpha R} = \text{const.}$) will not necessarily lead to the property of bulk incompressibility of this constituent, since the partial density functions ρ^α can still chance due to a variation in the volume fractions n^α. Moreover, the sum of all partial densities ρ^α yields the density ρ of the overall aggregate.

Miscible Components and Molar Concentrations The basic relations and definitions for the overall interstitial fluid φ^I, which is a real mixture (chemically spoken a solution) of the miscible constituents φ^β (with $\beta = \{L, D\}$) will be given here based on Ehlers [10]. In this solution, the constituent with the largest amount is called the solvent φ^L, while the other component is denoted as solute (i. e. the dissolved therapeutic molecules φ^D). Proceeding from the fact that volume fractions cannot be measured in case of this real mixture, the mixture components are considered by their partial densities ρ_I^β, defined with respect to the interstitial pore space (pore densities). Thus

$$\rho^\beta =: n^I \, \rho_I^\beta, \quad \text{where} \quad \rho_I^\beta = c_m^\beta \, M_m^\beta \quad \text{and} \quad \rho^{IR} = \sum_{\beta=L,D} \rho_I^\beta \, . \tag{4}$$

Therein, the molar concentration $c_m^\beta = \mathrm{d}n_m^\beta / \mathrm{d}v^I$, the molar mass M_m^β and the local number of moles $\mathrm{d}n_m^\beta$ are included. Since M_m^β is a constant of the species φ^β, the pore density ρ_I^β and, thus, the effective pore-fluid density ρ^{IR} can change through a variation in the molar concentration c_m^β.

Kinematics In order to guarantee independent motion functions, each constituent follows its own individual motion $\mathbf{x} = \boldsymbol{\chi}_\alpha(\mathbf{X}_\alpha, t)$ and has its own velocity field $\overset{\prime}{\mathbf{x}}_\alpha = \mathrm{d}\boldsymbol{\chi}_\alpha(\mathbf{X}_\alpha, t)/\mathrm{d}t$ with respect to different reference positions $\mathbf{X}_\alpha$. Based on the fundamental assumptions of the TPM, it is assumed that any spatial point $\mathbf{x}$ of the current configuration is simultaneously occupied by material points of all constituents. In porous media theories, it is generally convenient to proceed from a *Lagrange*an description of the solid matrix via the solid displacement $\mathbf{u}_S = \mathbf{x} - \mathbf{X}_S$ as the primary kinematic variable. In contrast, the pore-fluid flow is better expressed in a modified *Euler*ian setting via the seepage velocities $\mathbf{w}_\xi = \overset{\prime}{\mathbf{x}}_\xi - \overset{\prime}{\mathbf{x}}_S$ describing the fluid velocities in relation to the velocity of the deforming solid skeleton. For the overall interstitial fluid mixture, the pore diffusion velocity of φ^β is given by $\mathbf{d}_{\beta I} = \overset{\prime}{\mathbf{x}}_\beta - \overset{\prime}{\mathbf{x}}_I$.

3.2 Balance Relations and Constitutive Settings

The governing equations for the multi-phasic tissue bases on the metaphysical principles given in Truesdell [21]. Postulating quasi-static processes ($\overset{\prime\prime}{\mathbf{x}}_\alpha = \mathbf{0}$) at a common constant temperature (approximately 37°C for living biological

tissues) and exclude mass exchanges (such as phase transitions and chemical reactions) leads to a purely mechanical model governed by the following mass and momentum balances

$$\left.\begin{aligned} 0 &= (\rho^\alpha)'_\alpha + \rho^\alpha \operatorname{div} \overset{\prime}{\mathbf{x}}_\alpha \,, \\ \mathbf{0} &= \operatorname{div} \mathbf{T}^\alpha + \rho^\alpha \, \mathbf{b}^\alpha + \hat{\mathbf{p}}^\alpha \end{aligned}\right\} \quad \text{where} \quad \left\{\begin{aligned} \alpha &= \{S,\, B,\, L,\, D\} \\ \varphi^I &= \bigcup_{\beta=L,D} \varphi^\beta \,. \end{aligned}\right. \tag{5}$$

Therein, $\mathbf{T}^\alpha$ denotes the partial *Cauchy* stresses, $\mathbf{b}^\alpha$ the body forces and $\hat{\mathbf{p}}^\alpha$ the direct momentum production terms. The formulation of the mass balances given in Equation $(5)_1$ is valid for healthy tissue. However, results from clinical applications of CED by Voges *et al.* [23] indicates that uptake of therapeutic agents into the blood vessel system can occur in the immediate vicinity of a brain tumour. To include this leakage into the modelling approach would require a density production term for the liquid constituents, which is not carried out in this contribution.

Concentration Balances of the Interstitial Fluid Components The local mass balances of the components φ^β of the overall interstitial fluid can be written according to Equation (5) as

$$(\rho^\beta)'_\beta + \rho^\beta \operatorname{div} \overset{\prime}{\mathbf{x}}_\beta = 0 \,. \tag{6}$$

An insertion of appropriate relationships given in Section 3.1 leads to

$$(n^I c_m^\beta)'_S + \operatorname{div} (n^I c_m^\beta \, \mathbf{w}_\beta) + n^I c_m^\beta \operatorname{div} (\mathbf{u}_S)'_S = 0 \,. \tag{7}$$

The concentration balance can be rearranged with the help of the time derivative of the saturation condition (1). It follows with the expression

$$(n^I)'_S = (n^S + n^B) \operatorname{div} (\mathbf{u}_S)'_S + \operatorname{div} (n^B \mathbf{w}_B) \tag{8}$$

that the concentration balance of the therapeutic agent φ^D can also be written in the alternative form

$$n^I (c_m^D)'_S + c_m^D \operatorname{div} (\mathbf{u}_S)'_S + \operatorname{div} (n^I c_m^D \, \mathbf{w}_D) + c_m^D \operatorname{div} (n^B \mathbf{w}_B) = 0 \,. \tag{9}$$

Volume Balance of the Overall Interstitial Fluid The overall interstitial fluid is composed by the components φ^β. The mass balance of the overall interstitial fluid φ^I can be obtained by a summation over the particular mass balances of its components φ^β yielding

$$(\rho^I)'_I + \rho^I \operatorname{div} \overset{\prime}{\mathbf{x}}_I = 0 \,. \tag{10}$$

The volume balance of the overall interstitial fluid is not derived from Equation (10) due to the fact that ρ^{IR} is not necessarily constant, cf. Section 3.1. Therefore, we rather proceed from the mass balance of the liquid solvent φ^L

with the assumptions that the volume fraction of the drug is negligible in comparison to the volume fraction of the liquid solvent ($n^D \ll n^L \to n^L \approx n^I$) and, moreover, the velocity of the liquid solvent is approximately the same as from the interstitial fluid ($\overset{\prime}{\mathbf{x}}_L \approx \overset{\prime}{\mathbf{x}}_I$), see Ehlers [10]. The resulting volume balance reads

$$(n^I)'_S + \operatorname{div}(n^I \mathbf{w}_I) + n^I \operatorname{div}(\mathbf{u}_S)'_S = 0\,. \tag{11}$$

Volume Balance of the Blood Plasma The local mass balance of the blood plasma φ^B is rewritten in the time derivative of φ^B with respect to the solid motion and yields by use of the divergence theorem

$$(\rho^B)'_S + \operatorname{div}(\rho^B \mathbf{w}_B) + \rho^B \operatorname{div}(\mathbf{u}_S)'_S = 0\,. \tag{12}$$

Since the material density ρ^{BR} of the blood phase is constant, a combination of (3) and (12) leads to the volume balance of the blood phase, viz.:

$$(n^B)'_S + \operatorname{div}(n^B \mathbf{w}_B) + n^B \operatorname{div}(\mathbf{u}_S)'_S = 0\,. \tag{13}$$

Momentum Balance of the Overall Aggregate The quasi-static balance of momentum of the overall aggregate is derived by the sum of all particular momentum balances of the constituents φ^α. A uniform body force $\mathbf{b}$ for all constituents is assumed, and the summation over all direct momentum production terms $\hat{\mathbf{p}}^\alpha$ leads to zero. Thus,

$$\mathbf{0} = \operatorname{div}\mathbf{T} + \rho\,\mathbf{b}\,, \qquad \text{where} \quad \begin{cases} \mathbf{T} = \mathbf{T}^S + \mathbf{T}^I + \mathbf{T}^B \\ \rho = n^S\rho^{SR} + n^I\rho^{IR} + n^B\rho^{BR}\,. \end{cases} \tag{14}$$

Therein, $\mathbf{T}$ denotes the overall *Cauchy* stress tensor, and ρ is the density of the overall body.

Constitutive Settings In general, the above set of coupled partial-differential equations incorporates several independent fields. To close the set of governing equations, constitutive relations are required for the partial *Cauchy* stresses $\mathbf{T}^\alpha$, the direct momentum production terms $\hat{\mathbf{p}}^\xi$ of the pore-liquid components and $\hat{\mathbf{p}}^D$ of the therapeutic agent component. In addition, there is the need to formulate a further constitutive equation for a saturation function $\bar{s}^B$ of the blood constituent in order to be able to determine the volume fractions of all constituents.

The overall *Cauchy* stress $\mathbf{T}$ is derived within the concept of effective stress. Osmotic effects are basically not considered. In the partial stress tensors $\mathbf{T}^\xi = \mathbf{T}^\xi_E - n^\xi p^{\xi R}\,\mathbf{I}$ of the pore liquids, the extra-stresses $\mathbf{T}^\xi_E$ are neglected, see Ehlers [9]. The friction of the liquids in the pore compartments is considered in an implicit manner within the *Darcy* permeabilities. The partial

stress $\mathbf{T}^S = \mathbf{T}^S_E - n^S \mathcal{P}\,\mathbf{I}$ of the solid skeleton is used with the relation $\mathcal{P} = \bar{s}^B\, p^{BR} + \bar{s}^I\, p^{IR}$ for the summation of all particular stresses yielding

$$\mathbf{T} = \mathbf{T}^S_E - \underbrace{\frac{n^B}{(1-n^S)}}_{\bar{s}^B}\, p^{BR}\,\mathbf{I} - \underbrace{\frac{n^I}{(1-n^S)}}_{\bar{s}^I}\, p^{IR}\,\mathbf{I}\,. \tag{15}$$

The description of the elastically deformable solid skeleton is carried out using a linear elastic *Hooke*an law

$$\mathbf{T}^S_E \approx \boldsymbol{\sigma}^S_E = 2\,\mu^S\,\boldsymbol{\varepsilon}_S + \lambda^S\,(\boldsymbol{\varepsilon}_S \cdot \mathbf{I})\,\mathbf{I}\,, \tag{16}$$

which describes the solid extra stress as a function of the solid displacement vector $\mathbf{u}_S$ concerning small strains

$$\boldsymbol{\varepsilon}_S = \tfrac{1}{2}\,(\operatorname{grad}\mathbf{u}_S + \operatorname{grad}^T\mathbf{u}_S)\,. \tag{17}$$

Of course, the material modelling of the solid tissue behaviour could be extended to finite strains with viscous effects, but until now, a proper agreement concerning the elastic material parameters μ^S and λ^S is still missing. Hence, the modelling benefit would not exceed due to the inaccuracy of the viscous parameters.

Insertion of the postulated liquid extra momentum production terms

$$\hat{\mathbf{p}}^\xi_E = -n^\xi\,\gamma^{\xi R}(\mathbf{K}^\xi)^{-1}\,(n^\xi\,\mathbf{w}_\xi) \tag{18}$$

into the liquid momentum balances $(5)_2$ yields the *Darcy*-like filter laws

$$n^\xi\,\mathbf{w}_\xi = -\frac{\mathbf{K}^\xi}{\gamma^{\xi R}}\,(\operatorname{grad} p^{\xi R} - \rho^{\xi R}\,\mathbf{b})\,, \tag{19}$$

where $\gamma^{\xi R}$ is the effective fluid weight and $\mathbf{K}^\xi = \gamma^{\xi R}\,\mathbf{K}^{S\xi}/\mu^{\xi R}$ is the *Darcy* permeability. As already seen, two different intrinsic permeabilities $\mathbf{K}^{S\xi}$ are introduced, one for the tissue perfusion by blood and one by the interstitial fluid. Furthermore, one can also include anisotropic perfusion through the specific choice of the coefficients of the permeability tensors, see Section 3.3. The seepage velocity of the therapeutic agent $\mathbf{w}_D = \mathbf{d}_{DI} + \mathbf{w}_I$ is additively combined by the distribution of the drug via the interstitial fluid flow $\mathbf{w}_I$ and a concentration-driven pore diffusion velocity $\mathbf{d}_{DI}$. The distribution law for the therapeutic agent constituents can be derived in analogy to (19), as shown in Acartürk [1], with the neglect of non-existent electric potentials. Insertion of a constitutively introduced extra production term

$$\hat{\mathbf{p}}^D_E = -n^I R\,\Theta\,(\mathbf{D}^D)^{-1}\,(n^I c^D_m\,\mathbf{d}_{DI}) \tag{20}$$

of the therapeutic agent constituent into the therapeutic agent momentum balance $(5)_2$ leads to a *Fick*-like distribution law

$$n^I c^D_m\,\mathbf{d}_{DI} = -\,\mathbf{D}^D\operatorname{grad} c^D_m\,. \tag{21}$$

Therein, $\mathbf{D}^D$ denotes the effective drug diffusion tensor which can be obtained by diffusion-weighted magnetic resonance imaging, see Section 3.3. It has been left out until now that, generally, also all volume fractions of the constituents are basically unknown. The evolution of the volume fraction $n^S = n^S_{0S}\,(\det \mathbf{F}_S)^{-1}$ of the solid skeleton can be derived by a formal integration of the volume balance of the materially incompressible solid skeleton and the knowledge of the initial solidity n^S_{0S}. The volume fraction of the therapeutic agent can be neglected ($n^D \approx 0$), but the volume fractions of the pore liquids remain unknown. Therefore, only the saturation condition, Equation (1), is available. Hence, one additional constitutive equation has to be found in order to describe the division for the volume fractions of the liquids during a deformation process. A simple but definitely meaningful choice is a constant blood volume fraction, such as $n^B = n^B_{0S} = 0.05$. Herein, the inherent stability of the blood-vessel system is taken into account, and a change in solidity would only interact with the volume fraction of the interstitial fluid. This allows the determination of the interstitial volume fraction via $n^I = 1 - n^S - n^B_{0S}$. Further possibilities appear by the development of pressure-saturation relations, where the pressure difference $\Delta p = p^{BR} - p^{IR}$ is introduced. A proposal for a constitutive trigonometric saturation-like function reads

$$\bar{s}^B(\Delta p) = \tfrac{1}{\pi}\left(\arctan\left(\Delta p - 1\right)\right) + 0.5 \tag{22}$$

and is shown in Figure 6. This leads to a replacement of the interstitial fluid if the pressure difference Δp is positive and soft elastic blood vessel walls are assumed. Therefore, the liquid with the lower pressure can be simpler pushed away in the case of a deformation. This knowledge allows now for the determination of the particular volume fractions

$$n^B = \bar{s}^B\, n^F \;\rightarrow\; n^I = (1 - \bar{s}^B)\, n^F = 1 - n^S - n^B. \tag{23}$$

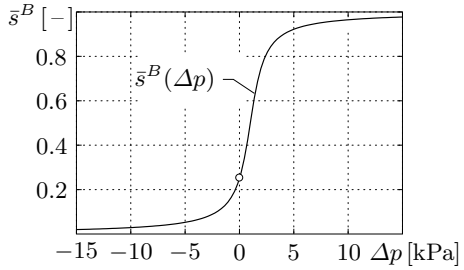

Fig. 6. Trigonometric, pressure-saturation relation

3.3 Investigation of Perfusion Parameters

Isotropic Representation For isotropic permeability properties, the permeability tensors for the liquid constituents simplify to $\mathbf{K}^{\xi} = K^{\xi}\,\mathbf{I}$. Herein, $K^{\xi} = k^{\xi} \,/\, \gamma^{\xi R}$ denotes the specific permeability with k^{ξ} as hydraulic conductivity. That means, only scalar permeability material parameters are required.

Anisotropic Representation Actually, the tissue properties of white matter are strongly characterised by its heterogeneous and anisotropic nature. In contrast to the isotropic properties which are valid for the grey matter, the diffusion coefficient in white matter blows up to a second order tensor describing anisotropic perfusion. The physical quantities, particularly the diffusion tensor $\mathbf{D}^{\mathrm{D}}$ and the permeability $\mathbf{K}_{0S}^{SI}$ of the interstitial fluid, can be obtained by patient-specific diffusion-weighted magnetic resonance imaging (DW-MRI). Basser *et al.* [3] proposed the first approach for the estimation of permeability characteristics from spin-echo experiments. This outstanding feature made it possible to obtain informations about the micro-structure of human brain tissue. Until today, a wide range of new applications and improvements are developed, and DW-MRI is established as an essential tool in modern medicine. To apply the previously presented model to a realistic scenario, information about the white matter, where the therapeutic agent is infused, is needed. Due to the fact that every human being is unique, patient-specific parameters have to be found *in vivo* in order to include them in the modelling approach. For a better illustration of the tissue anisotropy, one can visualise the diffusion at each voxel as an ellipsoid in order to distinguish between white and grey matter areas and cerebrospinal fluid spaces due to the shape and the size of the ellipsoids. Additionally, one can identify the white matter fibres in order to detect the connectivity of brain areas. But we do not focus here on the visualisation methods but on the diffusion parameters which are used in the further calculations. The symmetric, positive definite apparent water-diffusion tensor $\mathbf{D}^{\mathrm{n}}_{\mathrm{awd}}$ from raw diffusion tensor imaging can be written at each voxel as

$$\mathbf{D}^{\mathrm{n}}_{\mathrm{awd}} \;=\; D^{\mathrm{n}}_{ik}\,\mathbf{e}_i \otimes \mathbf{e}_k \;=\; \begin{bmatrix} D^{\mathrm{n}}_{11} & D^{\mathrm{n}}_{12} & D^{\mathrm{n}}_{13} \\ D^{\mathrm{n}}_{21} & D^{\mathrm{n}}_{22} & D^{\mathrm{n}}_{23} \\ D^{\mathrm{n}}_{31} & D^{\mathrm{n}}_{32} & D^{\mathrm{n}}_{33} \end{bmatrix} \mathbf{e}_i \otimes \mathbf{e}_k \,, \tag{24}$$

where n denotes the voxel number. This tensor can be further fragmented into eigenvectors and eigenvalues for each voxel and calibrated for the determination of tissue properties, as proposed in Sarntinoranont *et al.* [18] or Linninger *et al.* [16]. The basic assumption behind the calibration procedure is that $\mathbf{D}_{\mathrm{awd}}$ possesses the same eigenvectors as $\mathbf{D}^{\mathrm{D}}$ and $\mathbf{K}_{0S}^{SI}$, as proposed by Tuch *et al.* [22]. This is a reasonable assumption in brain tissue, but one should have in mind that the water molecules detected in DW-MRI can diffuse through the tissue cells, whereas the infused macro-molecules of the

therapeutic agent cannot, see Vorisek & Sykova [24]. This can probably cause a small inaccuracy in the distribution modelling. The calibration approach proceeds from the decomposition of the diffusion tensor at each voxel into eigenvalues $\gamma^{\mathrm{n}}_{i,\mathrm{awd}}$ and eigenvectors $\mathbf{v}^{\mathrm{n}}_i$, leading to the representation

$$\mathbf{D}^{\mathrm{n}}_{\mathrm{awd}} = \begin{bmatrix} \gamma^{\mathrm{n}}_{1,\mathrm{awd}} & 0 & 0 \\ 0 & \gamma^{\mathrm{n}}_{2,\mathrm{awd}} & 0 \\ 0 & 0 & \gamma^{\mathrm{n}}_{3,\mathrm{awd}} \end{bmatrix} \mathbf{v}^{\mathrm{n}}_i \otimes \mathbf{v}^{\mathrm{n}}_i \,, \tag{25}$$

with the mean of the eigenvalues

$$\bar{\gamma}^{n}_{\mathrm{awd}} = (\gamma^{\mathrm{n}}_{1,\mathrm{awd}} + \gamma^{\mathrm{n}}_{2,\mathrm{awd}} + \gamma^{\mathrm{n}}_{3,\mathrm{awd}})/3 \,. \tag{26}$$

Reference values from the literature for the permeability of the therapeutic agent $\bar{D}^{\mathrm{D}}$ and the permeability for the interstitial fluid $\bar{K}^{I}$ are used to scale the eigenvalues of $\mathbf{D}^{\mathrm{n}}_{\mathrm{awd}}$ via

$$\gamma^{\mathrm{n}}_{i,\mathbf{D}^{\mathrm{D,n}}} = \bar{D}^{\mathrm{D}} \frac{\gamma^{\mathrm{n}}_{i,\mathrm{awd}}}{\bar{\gamma}^{\mathrm{n}}_{\mathrm{awd}}} \quad \text{and} \quad \gamma^{\mathrm{n}}_{i,\mathbf{K}^{\mathrm{I,n}}} = \bar{K}^{\mathrm{I}} \frac{\gamma^{\mathrm{n}}_{i,\mathrm{awd}}}{\bar{\gamma}^{\mathrm{n}}_{\mathrm{awd}}} \,. \tag{27}$$

This procedure provides the effective drug diffusion tensor $\mathbf{D}^{\mathrm{D,n}}$ and the anisotropic permeability tensor $\mathbf{K}^{SI,\mathrm{n}}_{0S}$ for each evaluated voxel:

$$\mathbf{D}^{\mathrm{D,n}} = \sum_{i=1}^{3} \gamma^{\mathrm{n}}_{i,\mathbf{D}^{\mathrm{D,n}}} (\mathbf{v}_i \otimes \mathbf{v}_i) \quad \text{and} \quad \mathbf{K}^{SI,\mathrm{n}}_{0S} = \sum_{i=1}^{3} \gamma^{\mathrm{n}}_{i,\mathbf{K}^{\mathrm{I,n}}} (\mathbf{v}_i \otimes \mathbf{v}_i) \,. \tag{28}$$

Herein, $\mathbf{D}^{\mathrm{D,n}}$ accounts for both, the molecular properties of the therapeutic agent and the tissue anisotropy. The permeability is obviously higher in the direction of the white-matter fibre tracts. Since the eigenvalues correspond in their physical meaning to the transport magnitudes in the directions perpendicular and parallel to the aligned fibre directions, this will lead to a coincidence of two eigenvalues, see Kim *et al.* [15]. Due to the irregular distribution of the anisotropic perfusion parameters, it is impossible to define a closed analytical form for the perfusion parameters. A short overview of the implementation algorithm of the anisotropic permeabilities is shown in Figure 7 (left). It is not that easy to find freely available datasets of DW-MRI. Normally, they are belonging to the patients and are rarely carried out for healthy people. The data set used here was obtained from the internet (`http://www.sci.utah.edu/~gk/DTI-data/`) in order to demonstrate the feasibility of the implementation. The dataset consists of a human-readable Ascii header file (.nhdr), which provides the information about the corresponding binary file (.raw), where the voxel data is stored. A custom Matlab code reads the binary data, provides the possibility for data visualisation and converts it into a plain Ascii file. Some data cosmetics have to be derived in between, such as all datasets with negative eigenvalues are shifted out (because the tensor is not positive definite). Thus, the dataset is thinned out

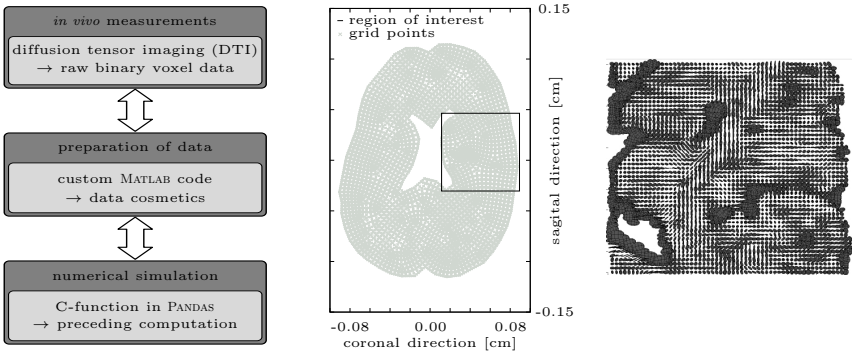

Fig. 7. Sketch of the implementation algorithm (left), area of interest for anisotropic permeabilities (middle) and visualisation of diffusion tensor ellipsoids (right)

until the area of interest remains in order to save calculation time. This "look-up table" is independent from the finite-element mesh. Here, the data points shown in Figure 7 (right) are considered. In this case, the special focus lies in description of the infusion process. Hence, only data sufficiently close to the infusion site have a ruling influence. The corresponding diffusion-tensor data with constant coefficients in the manner of a "look-up table" is then loaded in a preceding calculation step in the FE software tool PANDAS and allocated at each *Gauss* point for the numerical simulation, afterwards.

4 Numerical Implementation

Recapitulating Chapter 3, human brain tissue is fully described by the presented multiphasic modelling approach and can be solved numerically. The primary variables of an initial-boundary-value problem (IVBP) are the solid displacements $\mathbf{u}_S$ (associated to the momentum balance (14) of the overall aggregate), the effective pore pressures $p^{\xi R}$ (corresponding to the volume balances (11), (13) of the liquids), and the concentration c_m^D (belonging to the concentration balance (7) of the therapeutic agent).

4.1 Weak Formulation

In order to solve the system of strongly coupled differential equations numerically, the local (strong) forms of the governing balance equations have to be transferred into weak formulations. Ongoing from weighting the quasi-static formulation of the balance of momentum (14) by the corresponding vectorial

test function $\delta\mathbf{u}_S$, an integration over the spatial domain Ω leads to the weak formulation

$$\mathcal{G}_{\mathbf{u}_S} \equiv \int_\Omega \mathbf{T} \cdot \operatorname{grad} \delta\mathbf{u}_S \, \mathrm{d}v - \int_\Omega \rho\, \mathbf{b} \cdot \delta\mathbf{u}_S \, \mathrm{d}v - \int_{\Gamma_\mathbf{t}} \overline{\mathbf{t}} \cdot \delta\mathbf{u}_S \, \mathrm{d}a = 0\,. \quad (29)$$

Herein, $\overline{\mathbf{t}} = \mathbf{T}\,\mathbf{n}$ denotes the stress vector acting on the boundary of the overall aggregate, and $\mathbf{n}$ is the outward-oriented unit normal. That allows an explicit consideration of *Neumann* boundary conditions for initial-boundary-value problems. The liquid balance equations (11) and (13) are analogously multiplied with an independent scalar test function $\delta p^{\xi R}$, an integration over the spatial domain Ω leads to weak formulation of the liquid volume balances

$$\begin{aligned} \mathcal{G}_{p^\xi} \equiv \int_\Omega \delta p^{\xi R} \left[(n^\xi)'_S + n^\xi \operatorname{div}(\mathbf{u}_S)'_S \right] \mathrm{d}v - \\ - \int_\Omega n^\xi \mathbf{w}_\xi \cdot \operatorname{grad} \delta p^{\xi R} \, \mathrm{d}v + \int_{\Gamma_{v\xi}} \delta p^{\xi R}\, \bar{v}^\xi \, \mathrm{d}a = 0\,, \end{aligned} \quad (30)$$

where $\bar{v}^\xi = n^\xi \mathbf{w}_\xi \cdot \mathbf{n}$ is the volume efflux out of the domain. The resulting weak formulation for the concentration balance of the therapeutic agents $\mathcal{G}_{c_m^D}$ is derived analogously from Equation (7) and reads

$$\begin{aligned} \mathcal{G}_{c_m^D} \equiv \int_\Omega \delta c_m^D \left[(n^I c_m^D)'_S + n^I c_m^D \operatorname{div} (\mathbf{u}_S)'_S \right] \mathrm{d}v - \\ - \int_\Omega n^I c_m^D \mathbf{w}_D \cdot \operatorname{grad} \delta c_m^D \, \mathrm{d}v + \int_{\Gamma_{\bar{\jmath}^D}} \delta c_m^D \, \bar{\jmath}^D \, \mathrm{d}a = 0\,, \end{aligned} \quad (31)$$

where $\bar{\jmath}^D = n^I c_m^D \, \mathbf{w}_D \cdot \mathbf{n}$ is the molecule efflux of the therapeutic agent.

4.2 Spatial Discretisation and Mixed Finite Elements

The spatial discretisation of coupled problems within the framework of the finite element method requires mixed finite element formulations, see e. g. Ellsiepen [11]. This is particularly necessary for the strongly coupled biphasic four-component model of human brain tissue. Therefore, in addition to the primary variable solid displacement $\mathbf{u}_S$, all other primary variables, namely, the interstitial fluid pressure p^{IR}, the blood pressure p^{BR} and the molar concentration c_m^D of the therapeutic agent have to be approximated simultaneously. By doing so, the spatial domain occupied by the overall aggregate is subdivided into finite elements yielding an approximation of the continuous domain by the discrete domain. This discretisation yields a finite-element mesh with nodes for the geometry approximation, on which the following discrete test and field functions are defined:

$$
\begin{aligned}
\mathbf{u}_S(\mathbf{x},t) &\approx \mathbf{u}_S^h(\mathbf{x},t) = \bar{\mathbf{u}}_S^h(\mathbf{x},t) + \sum_{j=1}^{N_{\mathbf{u}_S}} \boldsymbol{\phi}^j_{\mathbf{u}_S}(\mathbf{x})\, \mathbf{u}_S^j(t)\,, \\
p^\xi(\mathbf{x},t) &\approx p^{\xi h}(\mathbf{x},t) = \bar{p}^{\xi h}(\mathbf{x},t) + \sum_{j=1}^{N_{p^\xi}} \phi^j_{p^\xi}(\mathbf{x})\, p^{\xi j}(t)\,, \\
c_m^D(\mathbf{x},t) &\approx c_m^{Dh}(\mathbf{x},t) = \bar{c}_m^{Dh}(\mathbf{x},t) + \sum_{j=1}^{N_{c_m^D}} \phi^j_{c_m^D}(\mathbf{x})\, c_m^{Dj}(t)\,.
\end{aligned}
\tag{32}
$$

A standard Galerkin method is applied using the same ansatz functions for the test and the field functions. The main difficulty in using such a mixed formulation lies behind the choice of the proper shape (ansatz) functions. The chosen shape functions are not arbitrary but have to fulfil the so-called *inf-sup* condition for the stability of the numerical solution as discussed in the work of Brezzi & Fortin [6]. In the present study, a possible choice for a stable numerical solution is made, namely, quadratic shape functions for the approximation of the solid displacement $\mathbf{u}_S$ and linear shape functions for the pore-liquid pressures p^{IR}, p^{BR} and the molar concentration c_m^D. Therefore, the previously mentioned stability condition is fulfilled. This type of mixed finite elements is known as extended *Taylor-Hood* elements (Figure 8).

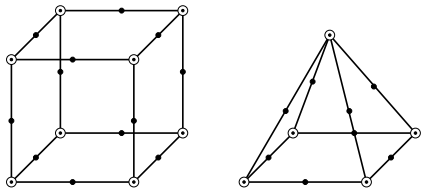

Fig. 8. Extended *Taylor-Hood* Elements: • displacement $\mathbf{u}_S^h$; ⊙ displacement $\mathbf{u}_S^h$, pressures $p^{\xi h}$ and concentration c_m^{Dh}

4.3 Coupled Solution Procedure

The weak formulations of the governing balance equations are given in an integral representation. For the numerical treatment of such integrals, the *Gauss* quadrature is appropriate, see Zienkiewicz & Taylor [27]. The benefit is the possibility to transform a continuous integral to a numerically accessible summation. Within this contribution, the hexahedral *Taylor-Hood* elements are fully integrated with 27 *Gauss* points. Since the continuous weak forms are now spatially discretised, the semi-discrete system will be written in an abstract formulation following Ammann [2]. For this, all degrees of freedom

(DOF) of the system, these are the N_n nodal unknowns of each primary variable, are gathered in a vector $\boldsymbol{u}$ such that

$$\boldsymbol{u} = [(\mathbf{u}_S^1, p^{IR,1}, p^{BR,1}, c_m^{D,1}),\ \ldots\ , (\mathbf{u}_S^{N_n}, p^{IR,N_n}, p^{BR,N_n}, c_m^{D,N_n})]^T\,. \quad (33)$$

The vectorial quantity $\mathbf{u}_S$ has three elements, one for each spatial direction. Following this and expressing the only appearing material time derivative with respect to the deforming solid skeleton $(\,\cdot\,)'_S$ via $(\,\cdot\,)'$, the so-called semi-discrete system can be written in an abstract description as

$$\boldsymbol{F}(t, \boldsymbol{u}, \boldsymbol{u}') = [\,\boldsymbol{M}\,\boldsymbol{u}' + \boldsymbol{k}(\boldsymbol{u}) - \boldsymbol{f}\,] \stackrel{!}{=} \mathbf{0}\,, \quad (34)$$

where $\boldsymbol{u}(t_0) = \boldsymbol{u}_0$. Therein, $\boldsymbol{M}$ is the generalised mass matrix, $\boldsymbol{k}$ the generalised stiffness vector and $\boldsymbol{f}$ the generalised force vector consisting of the *Neumann* boundary conditions. For a more detailed discussion on the topic solving the above equation, the interested reader is referred to the works of Diebels *et al.* [8] or Ellsiepen [11]. The above derived semi-discrete system still needs to be discretised in the time domain. For this purpose, the implicit (backward) *Euler* method defined by the backward *Taylor* series evaluated at the current time step t_{n+1} will be used:

$$\boldsymbol{u}_n = \boldsymbol{u}_{n+1} - \boldsymbol{u}'_{n+1}(t_{n+1} - t_n) \quad \longrightarrow \quad \boldsymbol{u}'_{n+1} = \frac{\boldsymbol{u}_{n+1} - \boldsymbol{u}_n}{t_{n+1} - t_n}\,. \quad (35)$$

Therein, n denotes the old time step. Since this scheme is unconditionally stable, this is the time-integration strategy, which is applied to the set of differential-algebraic equations (34) introduced above.

5 Numerical Examples

Initial-boundary-value problems (IBVP) can now be numerically evaluated in order to show the applicability of the modelling approach. We focus in this proposal on the numerical simulation of the distribution process of therapeutic agents, which are inserted into the brain tissue to treat malignant brain tumours. One prefix numerical example introduces the governing effects during an insertion of therapeutic agents. Afterwards, the main application is carried out in the numerical simulation of CED. Gravity forces are furthermore neglected in all numerical examples.

5.1 Extra-Vascular Insertion of Therapeutic Agents

Of course, a therapeutic agent could be applied intravenous, that means, it is allocated by the blood circulation. After reaching the target area, the widely diluted therapeutic agent has to pass in addition the BBB to enter the tissue. Unfortunately, this passing is not possible for the macro-molecules of the commonly used therapeutic agents. Therefore, the problem is addressed

from the other side by an insertion of the therapeutic agent directly into the extra-vascular space in order to bypass the BBB. Here, two different basic approaches can be distinguished. On the one hand, the implantation of so-called release systems can be realised (this guarantees at a certain spatial point a constant concentration). The disadvantage using release systems is that particles are distributed solely by diffusion and the resulting concentrations in the tissue reach therapeutically effective levels only within small tissue compartments. This comes from the fact that this distribution is mainly dependent on the concentration gradient and the molecular size of the inserted therapeutic agents. Hence, the effective diffusivity decreases in general with an increasing molecular weight. On the other hand, a long-lasting infusion can be realised by an influx of a solution containing the dissolved therapeutic agent. The transport of the infused molecules is then additionally driven by the present liquid flow of the solution. A comparison of these two methods in Figure 9 shows, that the distribution of a therapeutic agent is more efficient if the particles are transported within the interstitial fluid flow. One can clearly see that an infusion reaches larger target areas and supplies them with the administered drugs.

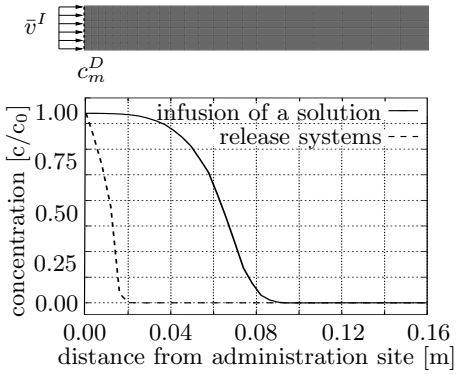

Fig. 9. Geometry (top) and comparison of the methods (bottom)

5.2 Simulation of Convection-Enhanced Delivery of Therapeutics

As was seen in Section 5.1, the application of an infusion of a solution containing the dissolved therapeutic agent is attractive for an effective treatment of malignant brain tumours, where a sufficient distribution is needed. This leads to modern clinical applications, such as the CED, with which we want to deal in detail in this numerical example. As already mentioned, the treatment of tumours with therapeutic agents administered through the vascular system is not effective in the human brain due to the BBB which protects the brain tissue against pollutants, as which the therapeutic agent is also seen.

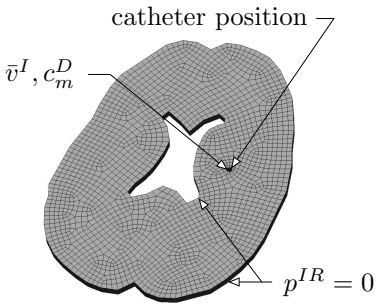

parameter	value	unit
$\mu^S =$	3.571	[kN/m^2]
$\lambda^S =$	14.286	[kN/m^2]
$n_{0S}^S =$	0.75	[-]
$n_{0S}^B =$	0.05	[-]
$n_{0S}^I =$	0.20	[-]
$\mu^{IR} =$	$0.89 \cdot 10^{-3}$	[Ns/m^2]

Fig. 10. Geometry of a horizontal brain section and the catheter position with the corresponding boundary conditions for the CED (left); material parameters (right)

Therefore, the practising surgeon drills small holes into the skull and place up to three catheter directly into the brain parenchyma. The therapeutic agents are then directly infused into the extra-vascular space within a solution. The pressure gradient generated by external medical pumps initiates an interstitial fluid flow and, therefore, the distribution of the therapeutic agents. This distribution process will now be numerically examined at a realistic geometry, a horizontal section of the human brain. For the spatial discretisation of the domain, approximately 2100 extended hexahedral 3-d *Taylor-Hood* elements are used, as described in Section 4.2. One has to mention that all formulations are derived in a 3-d geometry, even if a quasi 2-d geometry (one element in the thickness direction) is chosen to study the infusion process. As is shown in Figure 10, the catheter is virtually placed in the brain tissue, and over the surface, the corresponding boundary conditions for an infusion of a solution containing the dissolved therapeutic agent are applied. To be more precise, an influx of the interstitial fluid volume $\bar{v}^I$ containing the therapeutic agent with an inlet concentration c_m^D. The chosen values in Table 1 correspond to an usual application dose. On the outside of the brain (cortex) and the inner ventricles, the interstitial fluid pressure is set to zero, and an efflux of interstitial fluid and therapeutic agents over these surfaces is possible. The horizontal brain section is isostatically bedded in the inside, whereas the outer surface is allowed to deform. In Figure 10, the key material parameters for the computation are given. Therein, the material parameters for the elastic solid skeleton are chosen accordingly to publications of Chen & Sarntinoranont [7]. But one has to mention, that these *in vivo* elastic pa-

Table 1. Application dose of convection-enhanced drug delivery

load case	influx of liquid $\bar{v}^I$	inlet concentration c_m^D
infusion (CED)	$3.33 \cdot 10^{-7}$ [m^3/m^{2}s] ($\widehat{=} Q = 2.5$ [μl/min])	$3.7 \cdot 10^{-6}$ [mol/l]

rameters vary with several orders of magnitude in literature and are still not well determined. This might influence the distribution process of therapeutic agents only a little, but the influence for the stress states during an infusion process is crucial. Due to the fact that the local pressure should not exceed dangerous values, there are recently efforts to obtain the elastic properties from elastography, a MRI technique based on functional MRI. In contrast, the initial volume fractions of the constituents are generally accepted. The blood phase has around five volume per cent. The values for the interstitial fluid vary between 15-20 % and the remaining part results in the solidity. One has to mention that the human brain consists approximately of 80 % of water, but the dominant part of the water is bounded in the cells, this leads to a smaller porosity as probably suspected. The anisotropic parameters for the diffusion tensor $\mathbf{D}^{\mathrm{D}}$ of the therapeutic agent and the permeability $\mathbf{K}_{0S}^{SI}$ for the interstitial fluid are location-dependent and determined as shown in Section 3.3. This leads to the full anisotropic information at every *Gauss* point. During the simulation, an adaptive time increment $\Delta \mathrm{t}_n$ is used for the *Euler* time-integration scheme. In total, a time frame of about three days was investigated. Figure 11 shows the anisotropic spread of the therapeutic agent represented by the colour coding of the concentration of the therapeutic agent at different time steps. Here, only the region of interest close to the infusion point is depicted. One can see that the therapeutic agent is distributed as expected in an irregular manner due to the anisotropic permeability parameters. So the propagation front is not smooth. During the distribution

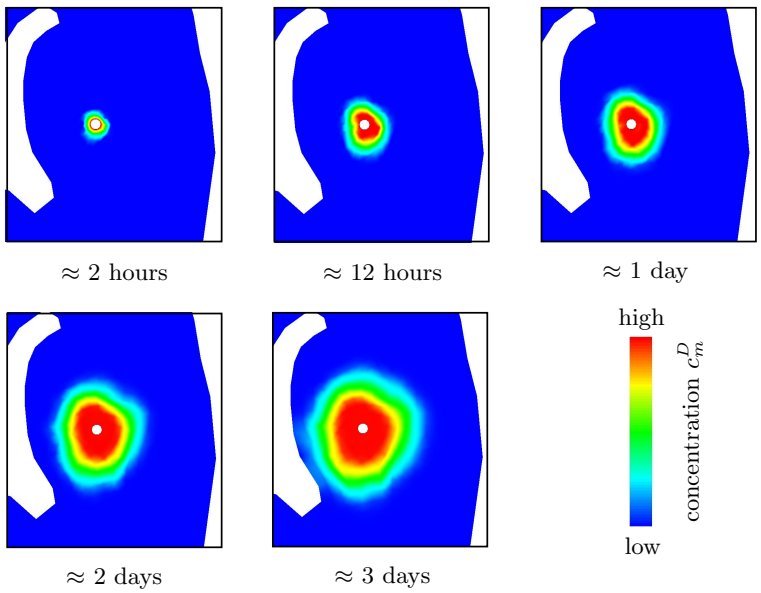

Fig. 11. Anisotropic distribution of the therapeutic agent during CED

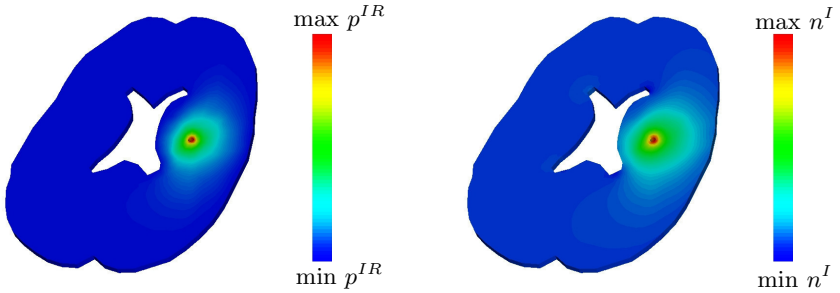

Fig. 12. Interstitial fluid pressure p^{IR} (left) and volume fraction n^I of the interstitial fluid (right) during the infusion process

process, preferred flow directions can be observed. But the channels with less concentration are closed due to the concentration gradients. In Figure 12, the pressure distribution of the interstitial fluid is presented, which naturally maximises at the infusion site of the catheter. The infusion pressure depends strongly on the rate of infusion, the stiffness of the solid skeleton and the permeabilities. The largest value of the interstitial fluid volume fraction in Figure 12 is also found at the infusion site of the catheter, since the solid constituent is displaced as a result of the infused solution.

6 Conclusions

An appropriate constitutive model based on the TPM was presented, which is able to describe human brain tissue in a meaningful way and is also suitable to map the process of infusion of therapeutic agents. This proposed model was implemented in the software package PANDAS making the numerical simulation of IBVP possible. As application under consideration, the convection-enhanced delivery method for the treatment of brain tumours was discussed. An important step was done in the meaningful consideration of anisotropies and heterogeneities of the white matter tracts, as this influences the observed irregular distribution of the infused therapeutic agents. Interesting topics on which the authors currently work are influences of the penetrated catheter, such as back-flow along the catheter shaft. The investigated model is able to describe the physical effects in a qualitative correct manner but it is still necessary to obtain correct material parameters in order to be able to predict the realistic distribution of the therapeutic agent and to support the surgeons.

Acknowledgements. The diffusion tensor MRI brain dataset by courtesy of Gordon Kindlmann (Scientific Computing and Imaging Institute, University of Utah) and Andrew Alexander (W. M. Keck Laboratory for Functional Brain Imaging and Behavior, University of Wisconsin-Madison).

References

[1] Acartürk, A.: *Simulation of Charged Hydrated Porous Media*. Dissertation, Bericht Nr. II-18 aus dem Institut für Mechanik (Bauwesen), Universität Stuttgart 2009.

[2] Ammann, M.: *Parallel Finite Element Simulations of Localization Phenomena in Porous Media*. Dissertation, Bericht Nr. II-11 aus dem Institut für Mechanik (Bauwesen), Universität Stuttgart 2005.

[3] Basser, P. J.; Mattielo, J. & Lebihan, D.: Estimation of effective self-diffusion tensor from the NMR spin-echo. *Journal of Magnetic Resonance* **103** (1994), 247–254.

[4] Bear, M. F.; Connors, B. W. & Paradiso, M. A. (eds.): *Neuroscience: Exploring the Brain*. Lippincott Williams and Wilkins, Philadelphia 2007, third edn.

[5] Bobo, R. H.; Laske, D. W.; Akbasak, A.; Morrison, P. F.; Dedrick, R. L. & Oldfield, E. H.: Convection-enhanced delivery of macromolecules in the brain. *Proceedings of the National Academy of Sciences* **91** (1994), 2076–2080.

[6] Brezzi, F. & Fortin, M.: *Mixed and Hybrid Finite Element Methods*. Springer-Verlag, New York 1991.

[7] Chen, X. & Sarntinoranont, M.: Biphasic finite element model of solute transport for direct infusion into nervous tissue. *Annals of Biomedical Engineering* **35** (2007), 2145–2158.

[8] Diebels, S.; Ellsiepen, P. & Ehlers, W.: Error-controlled Runge-Kutta time integration of a viscoplastic hybrid two-phase model. *Technische Mechanik* **19** (1999), 19–27.

[9] Ehlers, W.: Foundations of multiphasic and porous materials. In Ehlers, W. & Bluhm, J. (eds.): *Porous Media: Theory, Experiments and Numerical Applications*. Springer-Verlag, Berlin 2002, pp. 3–86.

[10] Ehlers, W.: Challenges of porous media models in geo- and biomechanical engineering including electro-chemically active polymers and gels. *International Journal of Advances in Engineering Sciences and Applied Mathematics* **1** (2009), 1–24.

[11] Ellsiepen, P.: *Zeit- und ortsadaptive Verfahren angewandt auf Mehrphasenprobleme poröser Medien*. Dissertation, Bericht Nr. II-3 aus dem Institut für Mechanik (Bauwesen), Universität Stuttgart 1999.

[12] Franceschini, G.; Bigoni, D.; Regitnig, P. & Holzapfel, G. A.: Brain tissue deforms similarly to filled elastomers and follows consolidation theory. *Journal of Mechanics and Physics of Solids* **54** (2006), 2592–2620.

[13] Groothuis, D. R.; Benalcazar, H. & Allen, C. V.: Comparison of cytosine arabinoside delivery to rat brain by intraveneous, intrathecal, intraventricular and intraparenchymal routes of administration. *Brain Research* **856** (2000), 281–290.

[14] Kawakami, K.; Kawakami, M. & Kioi, M.: Distribution kinetics of targeted cytotoxin in glioma by bolus or convection-enhanced delivery in a murine model. *Journal of Neurosurgery* **101** (2004), 1004–1011.

[15] Kim, J. H.; Mareci, T. H. & Sarntinoranont, M.: A voxelized model of direct infusion into the corpus callosum and hippocampus of the rat brain: model development and parameter analysis. *Medical and Biological Engineering and Computing* **48** (2010), 203–214.
[16] Linninger, A. A.; Somayaji, M. R.; Mekarsk, M. & Zhang, L.: Prediction of convection-enhanced drug delivery to the human brain. *Journal of Theoretical Biology* **250** (2008), 125–138.
[17] Lippert, H. (ed.): *Lehrbuch Anatomie*. Elsevier, München 2006.
[18] Sarntinoranont, M.; Chen, X.; Zhao, J. & Mareci, T. M.: Computational model of interstitial transport in the spinal cord using diffusion tensor imaging. *Annals of Biomedical Engineering* **34** (2006), 1304–1321.
[19] Schünke, M.; Schulte, E. & Schumacher, U. (eds.): *Prometheus: LernAtlas der Anatomie, Kopf und Neuroanatomie*. Georg Thieme Verlag, Stuttgart 2006.
[20] Smith, J. H. & Humphrey, J. A.: Interstitial transport and transvascular fluid exchange during infusion into brain and tumor tissue. *Microvascular Research* **73** (2007), 58–73.
[21] Truesdell, C.: *Rational Thermodynamics*. Springer-Verlag, New York 1984, second edn.
[22] Tuch, D. S.; Wedeen, V. J. & Dale, A. M.: Conductive tensor mapping of the human brain using diffusion tensor MRI. *Proceedings of the National Academy of Sciences USA* **98** (2001), 11697–11701.
[23] Voges, J.; Reszka, R. & Gossmann, A.: Imaging-guided convection-enhanced delivery and gene therapy of glioblastoma. *Annals of Neurology* **54** (2003), 479–487.
[24] Vorisek, I. & Sykova, E.: Measuring diffusion parameters in the brain: comparing the real-time iontophoretic method and diffusion-weighted magnetic resonance. *Acta Physiologica* **195** (2009), 101–110.
[25] Wagner, A. & Ehlers, W.: A porous media model to describe the behaviour of brain tissue. *Proceedings in Applied Mathematics and Mechanics* **8** (2008), 10201–10202.
[26] Wagner, A. & Ehlers, W.: Continuum-mechanical analysis of human brain tissue. *Proceedings in Applied Mathematics and Mechanics* **10** (2010), 99–100.
[27] Zienkiewicz, O. C. & Taylor, R. L.: *The Finite Element Method. The Basis*. Butterworth-Heinemann, Oxford 2000, fifth edn.

Hill-Type Muscles: From Virtual to Artificial Muscle

S. Schmitt[1,2], D. Häufle[1], T. Rupp[1,2] & M. Günther[1,2,3]

[1] Department of Sports and Exercise Science,
University of Stuttgart, Allmandring 28, 70569 Stuttgart, Germany
[2] Stuttgart Research Centre for Simulation Technology,
University of Stuttgart, Pfaffenwaldring 7a, 70569 Stuttgart, Germany
[3] Institute of Sports Science, Science of Motion,
University of Jena, Seidelstrasse 20, 07749 Jena, Germany

Abstract. The construction of artificial muscles, nowadays, is one of the most challenging developments in biomedical science. The application of artificial muscles is focussed both on the construction of orthotics and prosthetics for rehabilitation and prevention purposes and on building humanoid walking machines for robotics research. Research in biomechanics, a vital and broad field for over 80 years now (A.V. Hill 1922: Nobel prize in physiology for his discoveries related to the production of heat in the muscle), explains the function and design of real biological muscles and therefore lays the fundament for the development of functional artificial muscles. Recently, the hyperbolic Hill-type force-velocity relation was derived from simple mechanical components. It was shown that a contractile element (CE) consisting of a mechanical energy source (active element, AE), a parallel damper element (PDE), and a serial element (SE) exhibits operating points with hyperbolic force-velocity dependency. In this contribution, the macroscopic ansatz to derive the Hill relation is revisited and based on these ideas a technical proof of this concept is presented. Therein, AE and PDE were implemented as electric motors, SE as a mechanical spring. The force-velocity relation of this artificial CE was determined in quick release experiments. This artificial CE exhibited hyperbolic force-velocity dependency. Therefore, this proof of concept can be seen as a well-founded starting point for the development of Hill-type artificial muscles. Moreover, we show how the use of an antagonistic muscle actuator can help in stabilising a single inverted pendulum model in favour of a control approach using a linear torque generator.

1 Introduction

Human and animal movement is driven by muscle, a biological elastic actuator. A glance at the complexity and variety of the generated movements shows that muscle is a versatile, powerful, and flexible actuator [3, 12, 26, 30]. This is achieved because muscle can operate in different modes depending on the contraction dynamics and the structural implementation [21, 25]. From a robotics and prosthetics point of view, it would be desirable to have an artificial actuator with similar capabilities [11]. The construction of artificial muscles, nowadays, is one of the most challenging developments in biomedical science [1, 19]. The application of artificial muscles is focused both on the

construction of orthotics and prosthetics for rehabilitation and prevention purposes and on building humanoid walking machines for robotics research [5, 20].
Research in biomechanics, a vital and broad field for over 80 years now (A.V. Hill 1922: Nobel prize in physiology and medicine for his discovery relating to the production of heat in the muscle), explains the function and design of real biological muscles and therefore lays the fundament for the development of functional artificial muscles. Nevertheless, structure and functioning of biological muscles are not (yet) fully understood.
In biology, microscopic muscle models are able to predict muscle characteristics and functioning of biological muscles quite well [16, 17, 22, 23, 27, 29, 32, 33]. Unfortunately and as a trade-off, they require a large number of parameters. In a bionics approach it is an enormous challenge to realise all these properties of biological muscle in one artificial muscle at once [1].
Macroscopic muscle models are commonly based on phenomenology. Macroscopic muscle models are indeed of (limited) predictive character but do not incorporate any structural knowledge. Recently, the non-linear (hyperbolic-like) Hill-type force-velocity relation was derived from simple mechanical components [9]. It was shown that a contractile element (CE) consisting of a mechanical energy source (active element AE), a parallel damper element (PDE), and a serial element (SE) exhibits operating points with non-linear (hyperbola-like) force-velocity dependency. In this concept, the force-velocity relation is no longer a phenomenological outcome of a black box (i. e. the CE) but rather a physical outcome of the interaction of the three elements AE, PDE, and SE. Based on this concept, it is now possible to describe in detail which structural arrangement is necessary to get a biology-like force-velocity relation on a macroscopic level. Therefore, this concept can be interpreted as a basic engineering design for the CE of a Hill-type artificial actuator. In this manuscript, the meaning of the structural arrangement of the simple mechanical components already published, will be revisited. Furthermore, it will be shown by one first example of a technical embodiment, how this concept can help to construct more biologically-motivated artificial muscles. A first demonstration of how an artificial muscle could help in the stabilisation of a technical machine is theoretically shown by an antagonistic pair of our muscle. The control of an inverted pendulum can be improved by the use of a muscle-like drive in favour of a linear torque generator.

2 Material and Methods

Derivation of the Hill Parameters In a recent paper [9] it was demonstrated that the phenomenologically found [14] hyperbolic force-velocity relation of a concentrically contracting assembly of activated muscle fibres can be derived from the simple mechanical arrangement (Figure 1A) of an arbitrary force generating (active) element (AE) to which a damper (PDE) is

connected in parallel and a serial element (SE) in series fulfilling the force eqilibrium

$$F_M = F_{SE} = F_{AE} + F_{PDE}\,, \tag{1}$$

where the symbol "F" denotes a force produced by the element denoted by a corresponding index, and the kinematic relation for the lengths (symbols "l") of the elements AE, PDE, and SE

$$l_{AE} = l_{PDE} = l_M - l_{SE} \tag{2}$$

with l_M representing the muscle length. Note that a dot symbol "$\dot{l}$" denotes the first time derivative of a length l, i. e. an element's contraction velocity. In order to end up with a hyperbolic relation, two further assumptions had to be made. First, the force of the PDE was assumed to be

$$F_{PDE} = d_{PDE} \cdot \dot{l}_{PDE} = d_{PDE} \cdot \dot{l}_{AE} = d_{PDE} \cdot (\dot{l}_M - \dot{l}_{SE})\,, \tag{3}$$

where the damping coefficient of the PDE depends linearly on the current muscle force $F_M = F_{SE}$:

$$d_{PDE}(F_M) = D_{PDE,\max} \cdot \left((1 - R_{PDE}) \cdot \frac{F_M}{F_{AE,\max}} + R_{PDE} \right). \tag{4}$$

$D_{PDE,\max}$ is the maximum (at $F_M = F_{AE,\max}$) and R_{PDE} the normalised (to $D_{PDE,\max}$) minimum (force independent) value of $d_{PDE}(F_M)$. Second, the gearing ratio

$$\kappa_v = \frac{\dot{l}_{SE}}{\dot{l}_M} \tag{5}$$

between internal (SE) and external (muscle) velocities was represented by an arbitrary parameter value κ_v.

The characteristics of the SE did not have to be specified. The AE is the source of mechanical energy. It may depend on length and on the macroscopic chemical state of the muscle, i. e. the relative number of actively force-producing crossbridges quantified by the normalised muscle activation $0 \leq q \leq 1$.

In order to meet the conditions of our artificial muscle experiments presented in this paper, we had to modify the just reviewed model [9] with respect to only one feature. In contrast to Equation (6) in [9], which related the isometric force $F_M(\dot{l}_M = 0) = F_{M,0}$ (see Equation (1) for $\dot{l}_M = 0$) as a linear function of contraction velocity $\dot{l}_M$ to the AE force F_{AE}, we now assume the identity

$$F_{M,0} = F_{AE}\,. \tag{6}$$

Equation (6) is as consistent to the set of model equations (1,2,3,4,5) as is equation 6 in [9] to this very set.
Substituting Equation (3), the explicit dependency of $d_{PDE}(F_M)$ on force F_M and model parameters (Equation (4)), and Equation (5) into Equation (1) makes the latter force equilibrium Equation (1) to constitute a hyperbola

$$(F_M + A) \cdot \dot{l}_M = -B \cdot (F_{M,0} - F_M) \tag{7}$$

with the Hill parameters A,B and the isometric force $F_{M,0}$ being positive and $\dot{l}_M$ consistently being negative in the shortening (concentric) case. The Hill parameters are

$$A = \frac{R_{PDE}}{1 - R_{PDE}} \cdot F_{AE,\max}\,, \tag{8}$$

$$B = \frac{1}{1 - R_{PDE}} \cdot \frac{1}{1 - \kappa_v} \cdot \frac{F_{AE,\max}}{D_{PDE,\max}} = \frac{R_{PDE}}{1 - R_{PDE}} \cdot \frac{F_{AE,\max}}{F_{AE}} \cdot \dot{l}_{M,\max} \tag{9}$$

with the corresponding maximum shortening velocity

$$\begin{aligned} \dot{l}_{M,\max} &= \frac{B}{A} \cdot F_{M,0} = \frac{B}{A_{rel}} \\ &= \frac{1}{R_{PDE}} \cdot \frac{1}{1 - \kappa_v} \cdot \frac{F_{AE}}{D_{PDE,\max}}\,. \end{aligned} \tag{10}$$

The unloaded muscle ($F_M = 0$) would contract concentrically with $\dot{l}_M = -\dot{l}_{M,\max}$.

$$A_{rel} = \frac{A}{F_{M,0}} = \frac{F_{AE,\max}}{F_{AE}} \cdot \frac{R_{PDE}}{1 - R_{PDE}} \tag{11}$$

is defined as the Hill parameter A normalised to the current isometric force $F_{M,0} = F_{AE}$. Note that, for given $F_{M,0} = F_{AE}$, a concurrent parameter variation fulfilling $B/A = const$ meets the constraint $\dot{l}_{M,\max} = const$, whereat solely the curvature is changed. In our model, this is equivalent to $(1 - \kappa_v) \cdot D_{PDE,\max} \cdot R_{PDE} = const$.

Technical Embodiment The hardware implementation (Figure 1B) was done analogously. Both AE and PDE were realised each with an electric motor (Maxon ECmax40) [13]. The motor torque (T_{Motor}) was controlled by Maxon digital EC-motor control units (DEC 70/10). Both motors were mounted from opposite sides to the same disc with radius $r_{\mathrm{disk}} = 0.05\,m$. The disc was used to coil up a steel rope and exert a force

$$F_{AE} + F_{PDE} = r_{\mathrm{disk}} \cdot (T_{\mathrm{Motor}AE} + T_{\mathrm{Motor}PDE}) \tag{12}$$

on the rope. The force characteristics of the PDE and AE (Eqs. 3 and 6) were implemented in Matlab Simulink through Real Time Workshop and

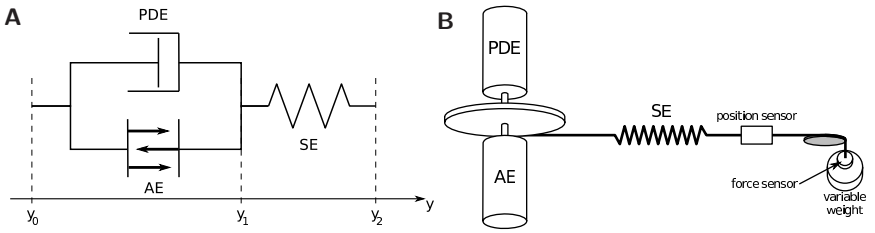

Fig. 1. A) Theoretical construct of the CE [9]. The CE consists of three elements: active element AE, parallel damping element PDE, and serial element SE. $y_0 = 0$ is the origin of the CE, y_1 represents the length of the AE/PDE and y_2 the length of the whole CE. By choosing $\kappa_v = 0.0$ in theory, we can turn the SE off in order to represent a contractile element without any compliance. **B)** Hardware design. AE and PDE were realised with electric motors, SE with a mechanical spring. A variable weight was used for the external loading of the CE.

Real Time Windows Target. In this way, the motors could exert the specified force on the steel rope as required by the theoretical construct. For the SE a spring ($k_{SE} = 2401\,Nm^{-1}$) was tied to a steel rope. Another motor could exert a defined external force on the CE construct. As sensor signals, the motor shaft positions φ_{Motor} were recorded by optical encoders (Scancon 2RMHF 5000 pulses/revolution), representing the internal degree of freedom y_1 and the total CE length y_2. A load cell (Transducer Techniques MLP 25 with amplifier TM0-1-24) was used to calibrate motor torques and exerted forces. All sensor data was recorded with Matlab Simulink via a Sensoray 626 AD I/O at $1\,kHz$.

To investigate the force-velocity characteristics of the artificial CE two types of experiments had to be performed. The first experiment was an isometric contraction (contraction with constant CE length: $y_2 - y_0 = \text{const.}$). Hereto, the CE end was fixed with the electromagnet guaranteeing a constant CE length. Then the AE activation was set to $A_{\text{AE}} = 1$ (maximum activation) and the shortening of the AE (rotation of the motors) was recorded. The time from the beginning of the activation until the end of AE shortening t_{isom} and the maximum isometric force $F_{CE}(t_{\text{isom}}) = F_{CE,\max}$ were evaluated.

Isotonic quick release experiments were performed to guarantee a defined $\kappa_v = 0$. Each isotonic quick release contraction experiment started like an isometric contraction. Only that the CE was released at $t_{\text{QR}} > t_{\text{isom}}$ ($t_{\text{QR}} = 3\,s$) by releasing the electro magnet. CE contraction velocity and force were evaluated shortly after t_{QR} at $t_{\text{eval}} = 3.5\,s$. The values $v_{CE}(t_{\text{eval}})$ and $F_{CE}(t_{\text{eval}})$ were extracted. The experiment was performed with different external forces, ten repetitions each. The curve $F_{CE}(t_{\text{eval}})$ vs. $v_{CE}(t_{\text{eval}})$ for all external forces represents the force-velocity characteristics of the artificial CE (Figure 3A, crosses).

Table 1. Muscle parameters (A, B, $F_{\max}$, $l_{CE,\mathrm{opt}}$) determined in experiments (see reference) and muscle model parameters (R_{PDE}, $(1-\kappa_v)D_{PDE}$) respectively calculated (see methods section).

muscle	A [N]	B [m/s]	$F_{\max}$ [N]	$l_{CE,\mathrm{opt}}$ [m]	R_{PDE}	$(1-\kappa_v)D_{PDE}$	Ref.
piglet gastrocnemius	3.0	0.015	30.0	0.015	0.003	2200	[10]
cat soleus	4.8	0.042	21.0	0.033	0.011	620	[4]
cat tenuissimus	0.05	0.057	0.18	0.032	0.600	4	[20]
rat gastrocnemius	2.68	0.042	13.4	0.013	0.167	386	[34]
rat tibialis anterior	4.3	0.053	4.3	0.027	0.076	162	[20]
frog sartorius	0.18	0.012	0.67	0.031	0.287	72	[20]

Representing the Variety of Biological Muscles In a further evaluation of our theoretical approach we scaled the model parameters to represent various biological muscles of different animals (Figure 3B). The model parameters R_{PDE} and $(1-\kappa_v)D_{PDE}$ were calculated (Eqs. 8, 9) from A and B values determined in experiments for different biological muscles (Table 1).

Control of the Inverted Pendulum A model of an inverted pendulum was used to investigate the effects that muscle-like actuator characteristics could have on the control of robotic stance. For quiet stance, the task was to keep an upright posture, while deflecting the ground to which the pendulum was suspended with a hinge joint. The model consisted of two rigid segments connected with a hinge joint (Figure 2). S1 had a mass of $m = 50\,kg$, an

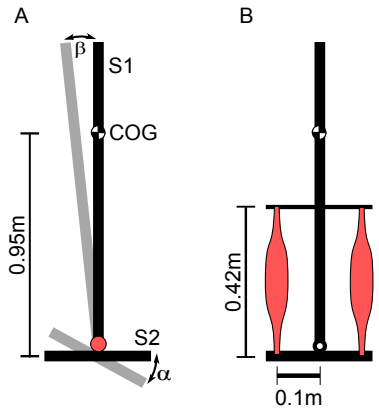

Fig. 2. Model of the inverted pendulum. S1 represents the leg-trunk segment, S2 the foot. COG indicates the centre of gravity location of S1. α is the angle of the foot (perturbation) and β the deviation from the upright position of S2. **A)** the joint is actuated by a direct torque generator with linear characteristics. **B)** model actuated by two antagonistic muscles.

Table 2. The parameters for the muscle model were based on Tibialis Anterior muscle [8]. The muscle model used for the study was described in detail elsewhere [10].

$L_{CE,\mathrm{opt}}$	$F_{\max}$	ΔW	ν_{CE}	$A_{rel,0}$	$B_{rel,0}$	$l_{SEE,0}$	$\Delta U_{SEE,\mathrm{nll}}$	$\Delta U_{SEE,\mathrm{l}}$	$\Delta F_{SEE,0}$	D_{SE}	R_{SE}
0.1m	10000N	0.57	4.0	0.25	$2.25s^{-1}$	0.23m	0.1825	0.073	10000N	0.3	0.01

inertia of $J = 45\,kgm^2$, the centre of gravity is at $h_{COG} = 0.95\,m$. The initial orientation of the leg/trunk segment S1 was vertical and horizontal for the foot segment S2. The pendulum could be perturbed by rotating S2 about the joint by the angle α. Two perturbations were considered: (a) a linear ramp increase of $\alpha = 1t \leq 1^\circ$ (for $0 \leq t \geq 1$, where t is the time) and $\alpha = 1^\circ$ (elsewhere), (b) a sinusoidal oscillation $\alpha = 1^\circ \sin(2\pi t)$, and (c) a sinusoidal oscillation $\alpha = 1^\circ \sin(0.2\pi t)$.

The hinge joint could be actuated either by a direct torque generator or by an antagonistic pair of muscles (Figure 2). The muscles were represented by two macroscopic muscle models. These muscle models incorporate the contraction dynamics described earlier, as well as a serial and a parallel elastic element representing the tendon and the passive elastic properties of soft muscle tissue. The muscle model was described in detail elsewhere [9]. The parameters used for the muscle models are listed in Table 2. Both muscles were connected to a simple geometry as depicted in Figure 2.

Muscles and direct torque generator were controlled based on a feedback signal measuring the deviation of segment S1 from the vertical orientation. A physiological delay of $\Delta t = 0.1\,s$ was considered. Three different controllers were applied: (1) no feedback is provided, (2) a simple proportional feedback (P-controller), and (3) a PID-controller. Matlab Simulink embedded ODE5 (Dormand-Prince) solver with $1\,ms$ step size was used to solve the differential equations.

3 Results

The relation between muscle output force and its contraction velocity is the common criterion for comparison of macroscopic muscle models. Therefore and firstly, we calculated the F-v curve (Figure 3A). The F-v curve of our functional artificial muscle shows a very good match with both the prediction from theory and biological experiments.

By comparing our artificial muscle prototype's force-velocity relation as shown above, we consider our approach as quite successful. The functional artificial muscle prototype exhibits contraction dynamics similar to Hill's model characteristics (Figure 3A).

In a model of the inverted pendulum, muscle-like non-linear actuator characteristics were compared against a direct torque generator (linear character-

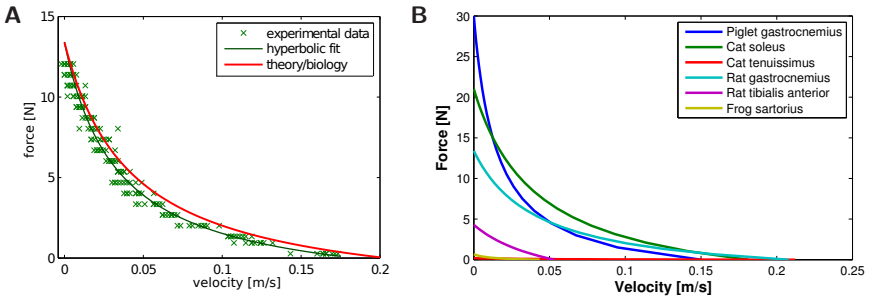

Fig. 3. A) Ten F(t) and v(t) plots for quick-release contraction experiments using 19 different external forces were recorded. Based on those F(t) and v(t) plots the force-velocity curve (crosses) was calculated. In direct comparison with the biological experiments and the predictions from theory, the artificial muscle data shows a good match for both, with $\kappa_v = 0$. A hyperbola fit of the artificial muscle data results in $R^2 = 0.97$. **B)** The strength of the approach presented here is shown by a comparison of F(v) curves calculated for different biological muscle parameters. The respective F-v curve can be plotted just by taking A and B values from experiments and using those A's and B's the parameters R_{PDE} and $(1 - \kappa_v)D_{PDE}$ which are necessary to build a technical muscle of that type can be calculated.

istics). The muscle-driven model did not topple, not even without feedback (first row, Figure 4). Also in case of the simple P controller (middle row) the muscle-driven model performed better during all perturbations and was able to cope better with the feedback delay of $\Delta t = 0.1\,s$. Only for the PID controller solutions were found, where the direct torque controller performed better (bottom row, Figure 4). Here shown is a solution with high gain for the integral part of the PID controller. Therefore, slow perturbations could be compensated very effectively.

4 Discussion

Element Representation For the active element (AE) which was formulated in theory [9] a brushless dc electric drive was used. The trade-offs of these actuators are the power-to-weight ratio and the necessity of a power supply, either over cable or by battery. Madden [24] gives an overview of current state-of-the-art of technical artificial muscles, their potential and their trade-offs. For our concept as of today, we are planning to use translational drives, which directly couple the driving forces to the movement direction, in favour of using rotational drives which translate rotational to translational movement over a drive disc. Translational drives are commercially available. However, for all electric drives one challenge remains: the storage of energy. Fortunately (or unfortunately), this is also a big issue in the automotive industry for the construction of electric vehicles. Therefore, we think that it is

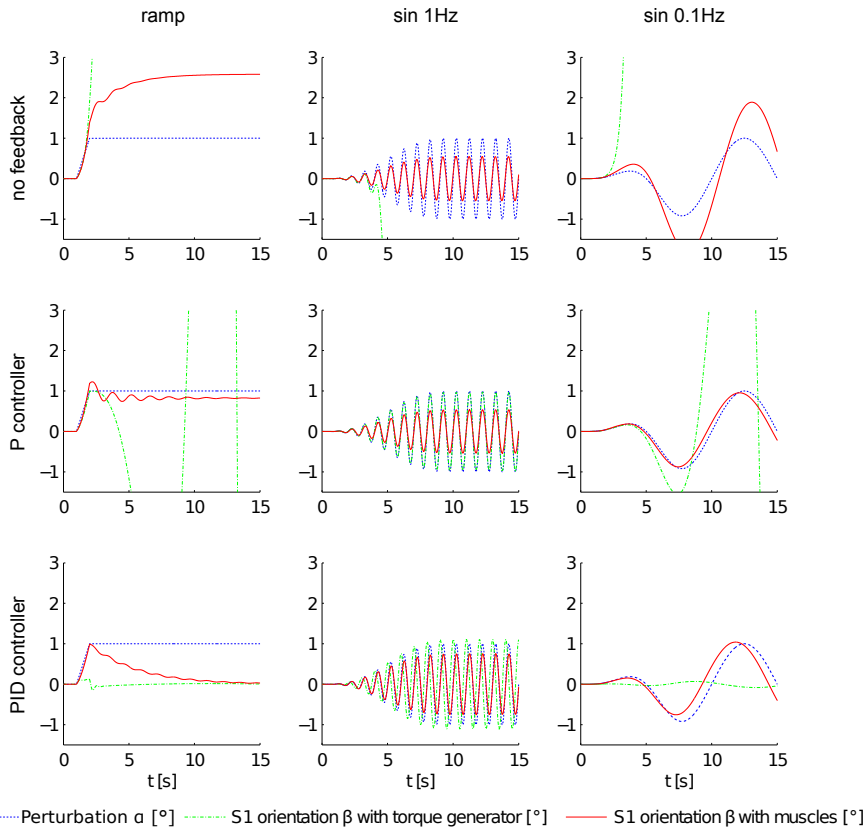

Fig. 4. Model reactions to perturbations in foot orientation α. Control target is the upright posture ($\beta = 0°$). Left column shows the reaction to a ramp perturbation, middle column to a $1\,Hz$, and right column to a $0.1\,Hz$ sinusoidal perturbation. Top row is without feedback, middle row with a simple P controller (direct torque controller gain: P 500; muscle controller gain: P 1), and bottom row with a PID controller (direct torque controller gains: P 500, I 50, D 500; muscle controller gains: P 1, I 0.3, D 0.3). The feedback signal is delayed by $\Delta t = 0.1\,s$.

likely to see great improvement in the storage technology in the near future. That would also help the use of electric drives as active element in functional artificial muscles.

The passive damping element (PDE) develops forces during the contraction, even over a very short period of time, which exceeds the output forces exerted by multiple times. The question is, are there comparable forces internal to the artificial muscle in other technical embodiments? Unfortunately, this is commonly not reported in literature. In our approach we use an electric drive to produce the damping forces which is in fact a non-passive damper. Are

there any materials or other approaches possible instead of the here presented approach by using an electric drive?
The serial element (SE), fortunately, seems to be the simplest challenge for a technical representation. This element should imply non-linear force-displacement characteristics. Even a steel rod would show the dynamic characteristics similar to that of the serial element predicted in theory. However, as must-have, this element needs to incorporate damping characteristics, yet very small [10]. It is to see how the artificial muscle prototype behaves when including a serial element like observed in biology and postulate in theory [9].

What is Gained Using this Approach? Understanding biological muscle characteristics and design is of great interest in biological science. Muscle models in general help in mathematically formulating muscle characteristics. The model structure is in essence purely mechanical and therefore can serve as a functional starting point of bionic muscle design. Phenomenological models based on biological experiments were the first to define muscle characteristics, e. g. [14]. Constantly improving lab techniques observed muscle phenomena even in great detail, e. g. [23]. Microscopic muscle models deduced from basic assumptions of muscle structure and/or functional relationships of single variables come into play shortly after, e. g. [15]. However, the benchmark of muscle dynamics used for those microscopic models is still the phenomenological Hill relation [14]. One approach just recently succeeded in defining the macroscopic muscle characteristics without the need of any phenomenological information. In contrast, this approach was validated against the well known experiments instead of being based on it [9]. Here, we used those findings to build a technical muscle and succeeded in the reproduction of crucial characteristics of biological muscle. With this approach, now, the macroscopic model can be iteratively improved accompanied with the technical muscle. In that, technical models can partly replace biological experiments.

Hill-Type Models for Control Hill-type muscle models, as an alternative to joint torque generators, have been implemented in (multi-body) computer models in order to generate movement. In this regard different control theories, i. e. physiologically motivated ones, e. g. equilibrium point hypothesis [2, 7], virtual model control [28], and others, e. g. as described above, come into operation. Hence, multi-body models with Hill-type muscles as actuators allow for using control theories to generate movement, thereby quantitatively testing control approaches [6, 31] and determining relevant control parameters [18] as well as comparing existing and/or newly developed control theories.
In this study different control approaches, i. e. no feedback, P-controller and PID-controller (see method section), were implemented and compared in two different inverted pendulums models, i. e. one with muscles and the other one

with direct torque generators. From this comparison of controls and actuators, it can be concluded, that the implementation of muscle-like characteristics changes the model's inherent stability and, thus, leads to a modification of successful control strategies to generate a similar movement. Furthermore, the presented arrangement of technical elements for the CE also allows for the investigation of structural changes in biological muscle used for movement control.
For further and more detailed conclusion, the presented approach will be implemented as muscle-like actuators in more complex (human) models to investigate (physiological motivated) control strategies and structural changes of muscle.

Acknowledgements. This work was supported by a Research Seed Capital (RisSC) - Tranche 2009 from the Ministery of Science, Research and Arts of Baden-Wuerttemberg, the University of Stuttgart (Kapitel 1403 Tit.Gr. 74) and by the German Research Foundation (DFG) within the Cluster of Excellence in Simulation Technology (EXC310/1) at the University of Stuttgart.

References

[1] Baughman, R.: Materials science. Playing nature's game with artificial muscles. *Science (New York, NY)* **308** (2005), 63–5.
[2] Bizzi, E.; Hogan, N.; Mussa-Ivaldi, F. A. & Giszter, S.: Does the nervous sytem use equilibrium-point control to guide single and multiple joint movements? *Behavioral and Brain Sciences* **15** (1992), 603–613.
[3] Close, R. I.: Dynamic properties of mammalian skeletal muscles. *Physiological Reviews* **52** (1972), 129–97.
[4] Cole, G. K.; van den Bogert, A. J.; Herzog, W. & Gerritsen, K. G.: Modelling of force production in skeletal muscle undergoing stretch. *Journal of Biomechanics* **29** (1996), 1091–1104.
[5] Dillmann, R.; Albiez, J.; Gassmann, B.; Kerscher, T. & Zöllner, M.: Biologically inspired walking machines: design, control and perception. *Philosophical Transactions Series A, Mathematical, Physical, and Engineering Sciences* **365** (2007), 133–51.
[6] Eilenberg, M. F.; Geyer, H. & Herr, H.: Control of a powered ankle-foot prosthesis based on a neuromuscular model. *IEEE Transactions on Neural Systems and Rehabilitation Engineering* **18** (2010), 164–73.
[7] Feldman, A. G.: Functional tuning of the nervous system with control of movement and maintenance of a steady posture. ii. controllable parameters of the muscles. *Biophysics* **11** (1966), 565–578.
[8] Günther, M. & Ruder, H.: Synthesis of two-dimensional human walking: a test of the lambda-model. *Biological Cybernetics* **89** (2003), 89–106.
[9] Günther, M. & Schmitt, S.: A macroscopic ansatz to deduce the Hill relation. *Journal of Theoretical Biology* **263** (2010), 407–18.

[10] Günther, M.; Schmitt, S. & Wank, V.: High-frequency oscillations as a consequence of neglected serial damping in Hill-type muscle models. *Biological Cybernetics* **97** (2007), 63–79.
[11] Hannaford, B.; Jaax, K. & Klute, G.: Bio-inspired Actuation and Sensing. *Autonomous Robots* **11** (2001), 267–272.
[12] Häufle, D. F. B.; Grimmer, S. & Seyfarth, A.: The role of intrinsic muscle properties for stable hopping - stability is achieved by the force-velocity relation. *Bioinspiration & Biomimetics* **5** (2010), 016004.
[13] Häufle, D. F. B.; Günther, M.; Blickhan, R. & Schmitt, S.: Proof of concept: model based bionic muscle with hyperbolic force-velocity relation. In *Proceedings of the first International Conference of Applied Biomechanics and Bionics*, 2010, pp. 1–7.
[14] Hill, A. V.: The heat of shortening and the dynamic constants of muscle. *Proceedings of the Royal Society of London. Series B* **126** (1938), 136–195.
[15] Huxley, A.: A note suggesting that the cross-bridge attachment during muscle contraction may take place in two stages. *Proceedings of the Royal Society of London B* **183** (1973), 83–86.
[16] Huxley, A.: Mechanics and models of the myosin motor. *Philosophical Transactions of the Royal Society of London B* **355** (2000), 433–440.
[17] Huxley, H.: Fifty years of muscle and the sliding filament hypothesis. *European Journal of Biochemistry* **271** (2004), 1405–1415.
[18] Kistemaker, D. A.; Van Soest, A. J. & Bobbert, M. F.: A model of open-loop control of equilibrium position and stiffness of the human elbow joint. *Biological Cybernetics* **96** (2007), 341–50.
[19] Klute, G.; Czerniecki, J. & Hannaford, B.: Mckibben artificial muscles: pneumatic actuators with biomechanical intelligence. *Advanced Intelligent Mechatronics, 1999. Proceedings. 1999 IEEE/ASME International Conference* (1999), 221–226.
[20] Klute, G. K.; Czerniecki, J. M. & Hannaford, B.: Artificial muscles: Actuators for biorobotic systems. *International Journal of Robotics Research* **21** (2002), 295–309.
[21] Lieber, R. L.: Skeletal muscle is a biological example of a linear electroactive actuator. *Proceedings of SPIE's 6th Annual International Symposium on Smart Structures and Materials* (1999), 1–7.
[22] Lombardi, V.; Piazzesi, G.; Ferenczi, M.; Thirlwell, H.; Dobbie, I. & Irving, M.: Elastic distortion of myosin heads and repriming of the working stroke in muscle. *Nature* **374** (1995), 553–555.
[23] Lombardi, V.; Piazzesi, G.; Reconditi, M.; Linari, M.; Lucii, L.; Stewart, A.; Sun, Y.; Boesecke, P.; Narayanan, T.; Irving, T. & Irving, M.: X-ray diffraction studies of the contractile mechanism in single muscle fibres. *Philosophical Transactions of the Royal Society of London B* **359** (2004), 1883–1893.
[24] Madden, J. D.: Mobile robots: motor challenges and materials solutions. *Science* **318** (2007), 1094–7.

[25] Maganaris, C. N.: Force-length characteristics of in vivo human skeletal muscle. *Acta Physiologica Scandinavica* **172** (2001), 279–85.

[26] McMahon, T. A.: *Muscles, reflexes, and locomotion*. Princeton University Press 1984.

[27] Piazzesi, G. & Lombardi, V.: A cross-bridge model that is able to explain mechanical and energetic properties of shortening muscle. *Biophysical Journal* **68** (1995), 1966–1979.

[28] Pratt, J.; Chew, C.-M.; Torres, A.; Dilworth, P. & Pratt, G.: Virtual model control: An intuitive approach for bipedal locomotion. *International Journal of Robotics Research* **20** (2001), 129–143.

[29] Reconditi, M.; Linari, M.; Lucii, L.; Stewart, A.; Sun, Y.; Boesecke, P.; Narayanan, T.; Fischetti, R.; Irving, T.; Piazzesi, G.; Irving, M. & Lombardi, V.: The myosin motor in muscle generates a smaller and slower working stroke at higher load. *Nature* **428** (2004), 578–581.

[30] Sandow, A.: Skeletal muscle. *Annual Review of Physiology* **32** (1970), 87–138.

[31] Selk Ghafari, A.; Meghdari, A. & Vossoughi, G.: Feedback control of the neuromusculoskeletal system in a forward dynamics simulation of stair locomotion. *Proceedings of The Institution of Mechanical Engineers Part H* **223** (2009), 663–75.

[32] Telley, I.; Denoth, J. & Ranatunga, K.: Inter-sarcomere dynamics in muscle fibres. A neglected subject? *Advances in Experimental Medicine and Biology* **538** (2003), 481–500.

[33] Tskhovrebova, L. & Trinick, J.: Role of titin in vertebrate striated muscle. *Philosophical Transactions of the Royal Society of London B* **357** (2002), 199–206.

[34] van Zandwijk, J. P.; Bobbert, M. F.; Baan, G. C. & Huijing, P. A.: From twitch to tetanus: performance of excitation dynamics optimized for a twitch in predicting tetanic muscle forces. *Biological Cybernetics* **75** (1996), 409–17, ISSN 0340-1200.

Modelling Cortical Bone Properties Using Homogenisation of Double Porous Medium

E. Rohan[1,2], R. Cimrman[1] & S. Naili[2]

[1] Department of Mechanics, Faculty of Applied Sciences,
University of West Bohemia, Univerzitní 8, 30614 Plzeň, Czech Republic
[2] Université Paris-Est Créteil Val de Marne Faculté des Sciences et Technologie,
Laboratoire Modelilisation et Simulation Multi Echelle,
61, Avenue du General de Gaulle, 94010 Créteil Cedex, France

Abstract. The paper describes the homogenisation approach to the cortical bone modelling featured by multi-level treatment. The homogenisation of the Biot continuum with double porosity provides upscaling from the osteon level to the macroscopic scale, where some memory effects are the consequences of the microflow in the dual porosity. To obtain the material properties of the osteon matrix, the hierarchical two-level homogenisation is proposed to upscale in two steps: from the scale of canaliculi to an intermediate scale of individually distinguishable lacunae, then to the level of the osteon matrix considered as the dual porosity which separates the Haverse/Volkmann vascular channels. The mathematical structure of the model is presented and some preliminary numerical illustrations are included.

1 Introduction

This paper concerns the homogenisation based modelling of the mechanical behaviour of fluid-saturated cortical bone tissue. The purpose of developing the multiscale model reported here is to provide an efficient computational tool which can be used firstly to study influence of the bone structure on the mechanical properties, namely on the stiffness and the overall strength, secondly to study the mechano-transduction: how the macroscopic loading determines local deformation and microflows in the hierarchical porous structure. The latter phenomenon is tightly related to evolutionary processes which on a longer time scale lead to tissue remodelling and growth.

There are two types of bone tissues: cortical and trabecular ones. Cortical bone is a compact tissue constituting bone envelope. The investigation of cortical bone is important since it accounts for about 80% of the skeleton, supports most of the load of the body, and is mainly involved in osteoporotic fractures of many kinds. The fluid in cortical bone plays a role in carrying nutrients and wastes from the bone cells (osteocytes) buried in the bony matrix.

Cortical bone tissue presents a structure composed of mineralised cylinders called osteons. These osteons, which are a few hundred micrometers in diameter and can be 12 mm long, are centred on Haversian canals whose diameters

are on the order of $40-100$ μm [5]. Osteons run primarily in the longitudinal axis of the bone. Volkmann canals are similar to Haversian canals except that they run between osteons, and thus, essentially along the transverse direction of bone. These macrochannels contain the vasculature, the nerves and interstitial fluid. Alternatively, the function of Haversian canals might be to serve as either pathways for nutrient transport or as drainage canals, regulated by the vasomotor function of the sphincter at the arterial end. As a result, the interstitial fluid may flow at different speeds depending on the location [5]. Moreover, there are other extravascular pores in the solid matrix of the bone. For instance, lacunæ are occupied by osteocyte cells. They can be seen as ellipsoidal cavities with diameters of $10-30$ μm. The canaliculi are small cylindrical channels whose diameters are on the order of 0.1 μm. They form a network connecting lacunæ and the Haversian/Volkmann vascular canals. Cytoplasmic osteocyte cell process occupies the central zone of each canaliculus so that the interstitial fluid pathway corresponds to an annular geometry. The canaliculus scale will be referred to as the mesoscale hereafter. Classical mechanical descriptions of cortical bone use the poroelasticity theory [7, 11], cf. [10]. To take into account explicitly the bone multi-scale morphology [16], combination of several modelling techniques appropriate for different hierarchies were considered in [8]

The purpose of this paper is to summarise recent contributions of the authors to the biomechanical application of the homogenisation theory to modelling fluid-saturated porous media. In particular, we propose to use the hierarchical homogenisation framework, see [14], to describe cortical bone properties. Multi-level poroelastic models seem to be an appropriate way to treat fluid movement and bone fluid pressures at the different scales. The previous considerations suggest the use of a double-porosity poroelastic model.

In Section 2 we consider upscaling the bone properties from the mesoscale associated with osteons, whereby the lacuno-canalicular system is respected by the dual porosity with anisotropic properties featuring the Biot model. In Section 3 we propose an upscaling procedure involving three levels: the submicroscale of the canalicular network, the osteon matrix porosity (microscale) including the lacunae and, finally, the "mesoscale" of the whole osteon.

1.1 Double Porosity and the Darcy Law

The double porous media are frequent in nature. Besides various examples in geomechanics, there are many instances of such media in biology and biomechanics. Models based on the double porosity were used in perfusion biomechanics [12]. The dual porosity is presented also by the canalicular network of the so-called matrix constituting the structure of cortical bone tissue, see Figure 2, [15].

In general, the *double porous* media [1, 2] are formed by two different porosities, which are qualitatively different; the *primary* porosity is featured by pores which are substantially larger than those of the *dual* porosity. In the

context of the bone microstructures, the two porosities are associated with the osteon level and with the canalicular level of the structure with characteristic lengths of $\ell^{\mu_1} = 100\mu m$ and $\ell^{\mu_2} = 10\mu m$, respectively.

The flow in the *dual porosity* can be treated using the Darcy law with the *high contrast permeability*, cf. [9]. In the context of the homogenisation procedure, the permeability coefficients depend on the characteristic scale of the representative volume. Canaliculi form a system of parallel cylindrical canals in the solid structure (see Figure 1, left). Assuming the Poiseuille flow in these canals, the mean velocity $\bar{v}$ of the parabolic profile with the pressure gradient $\partial p/\partial x$ in the canal direction x is given by

$$\bar{v} = -\frac{\pi R^2}{8\nu}\frac{\partial p}{\partial x} = -K_\nu^R \frac{\partial p}{\partial x} \quad \text{with} \quad K_\nu^R = \frac{\pi R^2}{8\nu}\,, \tag{1}$$

where R is the canal radius, ν is the kinematic viscosity and the scalar K_ν^R represents the permeability of the single canal.

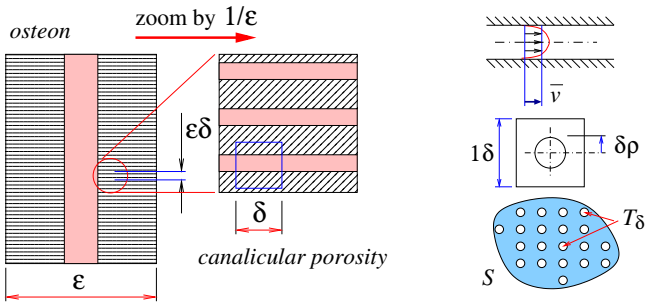

Fig. 1. Left: schematic illustration of the osteon double porous structure. Right: a scheme explaining the permeability δ^2-dependence due to the velocity profile in an array of canals. The total perfused area S is perforated by canals with total cross-section T_δ (bottom), each canal has the cross-section $\pi\rho^2\delta^2$; the square periodic cell is shown (middle) as well as the velocity profile in one canal. (top).

The relationship (1) reveals why in the *dual porosity*, the permeability coefficient is proportional to ε^2, where ε is the dimensionless scale parameter, see [15]. The osteon diameter $\ell^{\mu_1} = \varepsilon L$ and the canaliculus size $\ell^{\mu_2} = \delta\varepsilon L$ make the dual porosity associated with the *relative scale* δ. Moreover, for the bone porosities it holds that $\delta \sim \varepsilon$.

Therefore, we can use a relationship of the type $K_\nu^\varepsilon = \varepsilon^2 K_\nu^\rho$, which associates the porous ultrastructure characterised by the scale invariant permeability, K_ν^ρ, introduced in the spirit of (1) for $\rho \approx R$, with the dual porosity represented by K_ν^ε, which is characterised by scale ε.

1.2 The Biot Model of the Fluid-Saturated Porous Media

We shall recall the structure of the Biot model introduced in the framework of the phenomenological theory (only quasi-static loading assumed). It involves three essential constitutive laws: 1) the relationship between the drained solid skeleton "macroscopic" deformation $\boldsymbol{e}(\boldsymbol{u}(t,x))$ of the displacement field $\boldsymbol{u}(t,x)$, the fluid pressure in pores $p(t,x)$ and the total stress $\boldsymbol{\sigma}(t,x)$, 2) the relationship between the variation of the fluid content, skeleton deformation (mesoscopic level in our case), and the fluid pressure, 3) the Darcy law relating the seepage velocity, $\boldsymbol{w}(t,x)$, with fluid pressure $p(t,x)$. In the quasi-static case, two-field formulation is introduced in terms of $(\boldsymbol{u},p)$ which must satisfy the stress equilibrium a mass conservation equations,

$$\begin{aligned} &-\nabla\cdot(\mathbb{D}\,\boldsymbol{e}(\boldsymbol{u}))+\nabla\cdot(\boldsymbol{\alpha}p)=\boldsymbol{f}\,,\\ &\boldsymbol{\alpha}:\boldsymbol{e}(\dot{\boldsymbol{u}})-\nabla\cdot\boldsymbol{K}\nabla p+\frac{1}{\mu}\dot{p}=0\,, \end{aligned} \tag{2}$$

where $\mathbb{D}=(D_{ijkl})$, $i,j,k,l=1,...,3$ is the fourth-order tensor which is the drained anisotropic elasticity tensor of the porous matrix, $\boldsymbol{\alpha}=(\alpha_{ij})$ is the symmetric second-order tensor called the *Biot effective stress coefficient tensor*, μ is called the Biot's modulus and $\boldsymbol{K}=(K_{ij})$, $i,j=1,...,3$ is the anisotropic permeability tensor which is disproportional to the fluid dynamic viscosity. (Obviously, the symbol "$\cdot$" will denote the scalar product and the symbol ":" between tensors of any orders denotes their double contraction.) In Section 3 we show how these coefficients can be computed for a given micro- and mesostructure using the repeated (hierarchical) homogenisation.

2 Homogenisation of Fluid-Saturated Porous Media (FSPM)

The FSPM are treated usually in the framework of the *theory of porous media* (TPM), see e. g. [6], evolving from the models of soil consolidation (pioneered by K. von Terzaghi, enhanced by M. Biot) which is based on the phenomenological approach. The microstructure is respected just by local volume fractions of the different phases, thus *disregarding a more specific information* about topology and geometry of the microstructure.
The poroelasticity remains an interesting area still open to further research, since the universal concepts of the effective stresses, bulk pressures, the incompressibility and seepage phenomena need to be related to *lower-level processes undergoing in a specific microstructural arrangement*. In spite of increasing power of scientific computation, it is and will be still desirable to reduce computational requirements of "direct modeling" using model reduction techniques associated with upscaling and a multiscale decomposition. Among variety of such approaches, the *homogenisation of periodically heterogeneous material* seems to be an efficient tool.

The phenomenon of the *pore structural arrangement* is quite important feature of the fluid transport in porous structures. The two-scale homogenisation method allows describing the microstructure geometry which is then reflected in all effective parameters. In the model presented below we consider the Biot model to describe the bone behaviour at the osteon level, whereby existence of the lower level of porosity – the canaliculæ– is respected by the dual-porosity scaling.

2.1 Two Compartment Topology of the Microstructure

For modelling bone tissue formed by the Haversian–Volkmann channels and the canalicular matrix, the assumption of a two compartment topology of the microstructure appears to be convenient. In this section we summarise the homogenisation result which was obtained by asymptotic analysis of the problem of coupled diffusion and deformation in a dual porous medium featured by oscillating material coefficients. The medium is characterised by elasticity D^ε_{ijkl}, Biot coefficients α^ε_{ij}, permeability K^ε_{ij} and the Biot modulus μ^ε, where ε is a small parameter corresponding to the scale of the underlying microstructure. In [15] we considered the following problem imposed in an open bounded domain Ω: find displacement $\boldsymbol{u}^\varepsilon(t,\cdot) \in \boldsymbol{V}$ and pressure $p^\varepsilon(t,\cdot) \in H^1(\Omega)$ for almost all $t \in]0,T[$ such that:

$$\begin{aligned}
&\int_\Omega D^\varepsilon_{ijkl} e_{kl}(\boldsymbol{u}^\varepsilon) e_{ij}(\boldsymbol{v}) - \int_\Omega p^\varepsilon\, \alpha^\varepsilon_{ij} e_{ij}(\boldsymbol{v}) = \int_{\partial_\sigma \Omega} g_i\, v_i, d\Gamma\,, \quad \forall \boldsymbol{v} \in \boldsymbol{V}_0\,,\\
&\int_\Omega q\, \alpha^\varepsilon_{ij} e_{ij}(\frac{\mathrm{d}}{\mathrm{d}\,t}\boldsymbol{u}^\varepsilon) + \int_\Omega K^\varepsilon_{ij} \partial_j p^\varepsilon\, \partial_i q + \int_\Omega \frac{1}{\mu^\varepsilon}\frac{\mathrm{d}}{\mathrm{d}\,t} p^\varepsilon\, q = 0\,, \quad \forall q \in H^1(\Omega)\,,
\end{aligned} \tag{3}$$

where the initial conditions are satisfied: $\boldsymbol{u}(0,x) = 0$ and $p(0,x) = 0$ for almost all $x \in \Omega$. The boundary conditions employed in (3) correspond to impermeable surface of Ω, i. e. zero seepage through $\partial\Omega$, and traction forces prescribed on $\partial_\sigma\Omega \subset \partial\Omega$. The body is clamped on $\partial\Omega \setminus \partial_\sigma\Omega$, which is respected in a particular definition of sets $\boldsymbol{V}$ and $\boldsymbol{V}_0$; for the sake of simplicity we may consider $\boldsymbol{V} = \boldsymbol{V}_0 = \{\boldsymbol{v} \in \mathbf{H}^1(\Omega) |\ \boldsymbol{v} = 0 \text{ on } \partial\Omega \setminus \partial_\sigma\Omega\}$.
For finite scale $\varepsilon > 0$ domain Ω is decomposed into two principal non-overlapping parts, the channels Ω^ε_c and the matrix Ω^ε_m

$$\Omega = \Omega^\varepsilon_m \cup \Omega^\varepsilon_c \cup \Gamma^\varepsilon_{mc}, \quad \text{with} \quad \Omega^\varepsilon_m \cap \Omega^\varepsilon_c = \emptyset\,, \quad \Gamma^\varepsilon_{mc} = \overline{\Omega^\varepsilon_m} \cap \overline{\Omega^\varepsilon_c}\,, \tag{4}$$

where $\overline{\Omega}$ is the closure of Ω.
Domain Ω is generated as a periodic lattice using a representative periodic cell (RPC) denoted by Y, see Figure 2 (right). For simplicity we consider the RPC with the following definition: $Y = \Pi_{i=1}^3]0, \bar{y}_i[\subset \mathbb{R}^3$, $\bar{y}_i > 0$ can be chosen so that $|Y| = 1$ (i. e. unit volume of Y). Let Y_c be a (connected) subdomain of Y with Lipschitz boundary, so that $Y_m = Y \setminus \overline{Y_c}$.

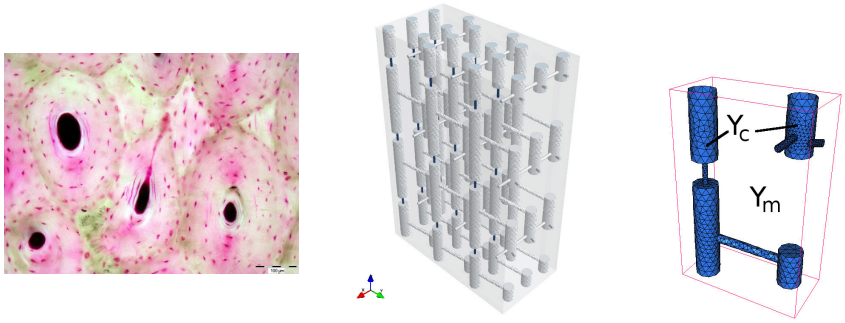

Fig. 2. Left: a micrograph of the osteon porosity arranged in cylindrical geometry. The Haversian canals form the centre of each osteon bounded by the cement line. The osteon matrix is penetrated by canalicular porous network arranged almost radially with respect to the osteon axis. (The colour image provided by courtesy of Zbyněk Tonar.) Right: microstructure decomposition w.r.t. the dual porosity: darker gray/blue: Ω_c, lighter gray/white: Ω_m, and the representative periodic cell Y decomposition.

This domain decomposition reflects the piecewise-continuous material coefficients; in general, we admit discontinuities in material coefficients on interface Γ_{mc}, so that, using the unfolding operator $\mathcal{T}_\varepsilon(\ )$, see [4],

$$\begin{aligned}
\mathcal{T}_\varepsilon\big(D^\varepsilon_{ijkl}(x)\big) &= \chi_m(y)D^m_{ijkl}(y) + \chi_c(y)D^c_{ijkl}(y)\,,\\
\mathcal{T}_\varepsilon\big(\alpha^\varepsilon_{ij}(x)\big) &= \chi_m(y)\alpha^m_{ij}(y) + \chi_c(y)\alpha^c_{ij}(y)\,,\\
\mathcal{T}_\varepsilon(\mu^\varepsilon(x)) &= \chi_m(y)\mu^m(y) + \chi_c(y)\mu^c(y)\,,\\
\mathcal{T}_\varepsilon\big(K^\varepsilon_{ij}(x)\big) &= \varepsilon^2\chi_m(y)K^m_{ij}(y) + \chi_c(y)K^c_{ij}(y)\,,
\end{aligned} \tag{5}$$

where χ_d, $d = m, c$ is the characteristic function of domain Y_d. All the parameters "$A^{m\varepsilon}, A^{c\varepsilon}$" introduced above have their values defined w.r.t. material points y in the microstructure – at that level these values are independent of ε. The dual porosity is respected by $\varepsilon^2\chi_m(y)K^m_{ij}(y)$ in $(5)_4$. This modelling ansatz leads to complex homogenised constitutive laws expressed using the homogenised material coefficients defined through the solutions of auxiliary microscopic problems. In what follows we record all the equations and problems constituting the model of the homogenised medium obtained for $\varepsilon \to 0$.

2.2 Homogenised Osteon – Two-Scale Model of the Cortical Bone

We record the result obtained in [15]. The two scale model consists of the *microscopic problems* at the level of osteons, which enable to compute homogenised coefficients involved in the *macroscopic model* describing a piece of the compact bone.

Microscopic Problems and Corrector Basis Functions The auxiliary microscopic problems, which are listed below, are imposed in the RPC; they comprise the steady and evolutionary problems. The associated solutions are the corrector basic functions of displacements, $\tilde{\boldsymbol{\omega}}^{ij}, \bar{\boldsymbol{\omega}}^{ij}, \tilde{\boldsymbol{\omega}}^{P}, \boldsymbol{\omega}^{*,P}$ and of pressures, $\tilde{\pi}^{ij}, \bar{\pi}^{ij}, \tilde{\pi}^{P}$. They are involved in the expressions of the homogenised material coefficients. We shall use the following abbreviated notation which conceals the dependence on spatial variables: $\pi(t,\cdot) =: \pi(t)$, $\boldsymbol{\omega}(t,\cdot) =: \boldsymbol{\omega}(t)$. In the sequel we shall use the following bilinear forms:

$$\begin{aligned} a_Y(\boldsymbol{u},\boldsymbol{v}) &= \fint_Y D_{ijkl}(y) e^y_{kl}(\boldsymbol{u})\, e^y_{ij}(\boldsymbol{v})\,, \quad b_Y(\varphi,\boldsymbol{v}) = \fint_Y \varphi\, \alpha_{ij}(y) e^y_{ij}(\boldsymbol{v})\,, \\ b_{Y^m}(\varphi,\boldsymbol{v}) &= \fint_{Y_m} \varphi\, \alpha^m_{ij}(y) e^y_{ij}(\boldsymbol{v})\,, \quad c_{Y_m}(\varphi,\psi) = \fint_{Y_m} K^m_{ij}(y)\partial^y_j\varphi\partial^y_i\psi\,, \\ d_{Y_m}(\varphi,\psi) &= \fint_{Y_m} (\mu^m)^{-1}\psi\,\varphi\,, \end{aligned} \tag{6}$$

where $\fint_{Y_d} \equiv |Y|^{-1}\int_{Y_d}$, $d = m, c$, and $\partial^y_j = \partial/\partial y_j$ (the same context used for small strain tensor e^y_{ij}). We define vectors $\boldsymbol{\Pi}^{rs} = (\Pi^{rs}_i)$ whose components $\Pi^{rs}_i = y_s\delta_{ir}$ are constituted by coordinates y_s, where δ_{ir} is the Kronecker symbol. By $\mathbf{H}^1_{\#}(Y)$ we denote the Sobolev space $[W^{1,2}(Y)]^3$ of Y-periodic vector functions, the analogous notation holds for scalar functions. Below we employ space (for any $Y_d \subset Y$)

$$H^1_{\#0}(Y_d) = \{v \in H^1_{\#}(Y_d) |\ v = 0 \text{ on } \partial Y_d \cap Y\}\,, \tag{7}$$

so that $H^1_{\#0}(Y_m)$ contains functions vanishing on the interface $\Gamma = \partial Y_m \cap \partial Y_c$.

Steady Problem for Strain-Associated Correctors We define couple $(\bar{\boldsymbol{\omega}}^{rs}, \bar{\pi}^{rs}) \in \mathbf{H}^1_{\#}(Y) \times H^1_{\#0}(Y_m)$ as the solution of the following problem

$$\begin{aligned} &a_Y(\bar{\boldsymbol{\omega}}^{rs},\, \boldsymbol{v}) = -a_Y(\boldsymbol{\Pi}^{rs},\, \boldsymbol{v}) \quad \forall \boldsymbol{v} \in \mathbf{H}^1_{\#}(Y)\,, \\ &c_{Y_m}(\bar{\pi}^{rs},\, q) = -b_{Y^m}(q,\, \bar{\boldsymbol{\omega}}^{rs} + \boldsymbol{\Pi}^{rs}) \quad \forall q \in H^1_{\#0}(Y_m)\,, \end{aligned} \tag{8}$$

Evolutionary Problem for Strain-Associated Correctors For any $t \in]0,T[$, the couple $(\tilde{\boldsymbol{\omega}}^{rs}(t,\cdot), \tilde{\pi}^{rs}(t,\cdot)) \in \mathbf{H}^1_{\#}(Y) \times H^1_{\#0}(Y_m)$ must satisfy

$$\begin{aligned} a_Y(\tilde{\boldsymbol{\omega}}^{rs},\, \boldsymbol{v}) - b_{Y^m}\left(\frac{\mathrm{d}}{\mathrm{d}\,t}\tilde{\pi}^{rs},\, \boldsymbol{v}\right) = 0 \quad \forall \boldsymbol{v} \in \mathbf{H}^1_{\#}(Y)\,, \\ b_{Y^m}(q,\, \tilde{\boldsymbol{\omega}}^{rs}) + c_{Y_m}(\tilde{\pi}^{rs},\, q) + d_{Y_m}\left(\frac{\mathrm{d}}{\mathrm{d}\,t}\tilde{\pi}^{rs},\, q\right) = 0 \quad \forall q \in H^1_{\#0}(Y_m)\,, \end{aligned} \tag{9}$$

where $\tilde{\pi}^{rs}(0) = -\bar{\pi}^{rs}$ and functions from $H^1_{\#0}(Y_m)$ vanish on the interface $\partial Y_m \cap \partial Y_c$.

Steady Problem for Pressure-Associated Correctors We define couple $(\boldsymbol{\omega}^{*,P},\, \tilde{\pi}^P(0)) \in \mathbf{H}^1_{\#}(Y) \times H^1_{\#0}(Y_m)$ as the solution of the following problem

$$\begin{aligned} &a_Y\left(\boldsymbol{\omega}^{*,P},\, \boldsymbol{v}\right) - b_{Y^m}\left(\tilde{\pi}^P(0),\, \boldsymbol{v}\right) = b_Y\left(1,\, \boldsymbol{v}\right) \quad \forall \boldsymbol{v} \in \mathbf{H}^1_{\#}(Y)\,, \\ &b_{Y^m}\left(q,\, \boldsymbol{\omega}^{*,P}\right) + d_{Y_m}\left(\tilde{\pi}^P(0),\, q\right) = -d_{Y_m}\left(1,\, q\right) \quad \forall q \in H^1_{\#0}(Y_m)\,. \end{aligned} \tag{10}$$

Evolutionary Problem for Pressure-Associated Correctors For any $t \in]0,T[$, we define couple $(\tilde{\boldsymbol{\omega}}^P(t,\cdot), \tilde{\pi}^P(t,\cdot)) \in \mathbf{H}^1_{\#}(Y) \times H^1_{\#0}(Y_m)$ as the solution of the following problem (initial condition $\tilde{\pi}^P(0)$ given by (10))

$$\begin{aligned} a_Y\left(\tilde{\boldsymbol{\omega}}^P,\, \boldsymbol{v}\right) - b_{Y^m}\left(\frac{\mathrm{d}}{\mathrm{d}\,t}\tilde{\pi}^P,\, \boldsymbol{v}\right) = 0 \quad \forall \boldsymbol{v} \in \mathbf{H}^1_{\#}(Y)\,, \\ b_{Y^m}\left(q,\, \boldsymbol{\omega}^P\right) + c_{Y_m}\left(\tilde{\pi}^P,\, q\right) + d_{Y_m}\left(\frac{\mathrm{d}}{\mathrm{d}\,t}\tilde{\pi}^P,\, q\right) = 0 \quad \forall q \in H^1_{\#0}(Y_m)\,. \end{aligned} \tag{11}$$

Problem for Pressure Correctors in Channels The following problem is imposed in channels Y_c: find $\eta^k \in H^1_{\#}(Y)/\mathbb{R}$, $k = 1,2,3$ satisfying

$$\int\!\!\!\!\!\!-_{Y_c} K^c_{ij}\partial^y_j(\eta^k + y_k)\,\partial^y_i\psi = 0 \quad \forall \psi \in H^1_{\#}(Y)\,. \tag{12}$$

Macroscopic Problem in the Time Domain The macroscopic problem is defined in terms of the homogenised material coefficients which are computed using the corrector basis functions introduced above. While the homogenised permeability $\mathcal{C}_{ij}$ is time-independent tensor,

$$\mathcal{C}_{ij} = \int\!\!\!\!\!\!-_{Y_c} K^c_{kl}\partial^y_l(\eta^j + y_j)\,\partial^y_k(\eta^i + y_i)\,, \tag{13}$$

all other homogenised counterparts of D_{ijkl}, α_{ij}, $1/\mu$, which below are denoted by $\mathcal{D}^{\mathrm{eff}}_{ijkl}$, $\alpha^{\mathrm{eff}}_{ij}$ and $\mathcal{M}^{\mathrm{eff}}$, respectively, involve their time-dependent parts which are responsible for the fading memory phenomenon present in the macroscopic problem. Below we employ the Heaviside function $H_+(t)$.
The *viscoelastic coefficients* can be decomposed into two symmetric 4-order tensors,

$$\mathcal{D}^{\mathrm{eff}}_{ijkl} = [\mathcal{E}_{ijkl} + \mathcal{H}_{ijkl}(t)]H_+(t)\,,$$

which are defined, as follows:

- the homogenised elastic tensor

$$\mathcal{E}_{ijkl} = a_Y\left(\boldsymbol{\Pi}^{kl} + \bar{\boldsymbol{\omega}}^{kl},\, \boldsymbol{\Pi}^{ij} + \bar{\boldsymbol{\omega}}^{ij}\right), \tag{14}$$

- the homogenised viscosity tensor of the fading memory

$$\mathcal{H}_{ijkl}(t) = c_{Y_m}\left(\frac{\mathrm{d}}{\mathrm{d}\,t}\tilde{\pi}^{kl}(t),\, \bar{\pi}^{ij}\right). \tag{15}$$

While symmetry $\mathcal{E}_{ijkl} = \mathcal{E}_{klij} = \mathcal{E}_{jikl}$ is evident, the symmetry $\mathcal{H}_{ijkl}(t) = \mathcal{H}_{klij}(t) = \mathcal{H}_{jikl}(t)$ results from the structure of (8), (9) and from the semi-group general properties.
The *Biot coefficients*,

$$\alpha_{ij}^{\mathrm{eff}}(t) = \mathcal{B}_{ij}H_+(t) + \mathcal{P}_{ij}(t)H_+(t)\,,$$

are decomposed into the constant and fading memory parts, as follows:

- the "elastic" homogenised Biot coefficients

$$\mathcal{B}_{ij} = \fint_Y \alpha_{ij} + b_Y\left(1,\, \bar{\boldsymbol{\omega}}^{ij}\right), \tag{16}$$

- the "fading memory" homogenised Biot coefficients

$$\mathcal{P}_{ij}(t) = b_Y\left(1,\, \tilde{\boldsymbol{\omega}}^{ij}(t)\right) + d_{Y_m}\left(\frac{\mathrm{d}}{\mathrm{d}\,t}\tilde{\pi}^{ij}(t),\, 1\right). \tag{17}$$

The effective *reciprocal Biot modulus*,

$$\mathcal{M}(t) = \mathcal{M}\delta_+(t) + \mathcal{N}(t)H_+(t)\,, \tag{18}$$

where $\delta_+(t)$ is the Dirac function, comprises two parts:

- the constant part,

$$\mathcal{M} = \fint_Y \frac{1}{\mu} + d_{Y_m}\left(\tilde{\pi}^P(0),\, 1\right) + b_Y\left(1,\, \boldsymbol{\omega}^{*,P}\right), \tag{19}$$

- and the part responsible for the fading memory effect:

$$\mathcal{N}(t) = d_{Y_m}\left(\frac{\mathrm{d}}{\mathrm{d}\,t}\tilde{\pi}^P(t),\, 1\right) + b_Y\left(1,\, \tilde{\boldsymbol{\omega}}^P(t)\right). \tag{20}$$

The ultimate form of the homogenised dual-porous Biot continuum is represented by the macroscopic model, where $\mathcal{H}(t), \mathcal{P}(t)$ and $\mathcal{N}(t)$ are responsible for the fading-memory effects. Their numerical representation and namely the numerical scheme for computing the associated convolution integrals is discussed in [13].

Formulation of the Macroscopic Problem Recalling assumed unloaded and stress-free initial structure, the homogenised problem reads, as: for a.a. $t \in]0,T[$ find $\boldsymbol{u} \in V$ and $p \in H^1(\Omega)$ with $p(0,\cdot) = 0$ such that

$$\int_\Omega \mathcal{E}_{ijkl} e_{kl}(\boldsymbol{u}) e_{ij}(\boldsymbol{v}) + \int_\Omega \int_0^t \mathcal{H}_{ijkl}(t-\tau) e_{kl}(\frac{\mathrm{d}}{\mathrm{d}\,\tau}\boldsymbol{u}(\tau))\, d\tau\, e_{ij}(\boldsymbol{v})$$
$$-\int_\Omega (\mathcal{B}_{ij} + \mathcal{P}_{ij}(0))\, p\, e_{ij}(\boldsymbol{v}) - \int_\Omega \int_0^t \frac{\mathrm{d}}{\mathrm{d}\,t}\mathcal{P}_{ij}(t-\tau) p(\tau)\, d\tau\, e_{ij}(\boldsymbol{v}) = \int_{\partial_\sigma \Omega} \boldsymbol{g}\cdot\boldsymbol{v}\, d\Gamma,$$

$$\int_\Omega (\mathcal{B}_{ij} + \mathcal{P}_{ij}(0))\, e_{ij}(\frac{\mathrm{d}}{\mathrm{d}\,t}\boldsymbol{u})\, q + \int_\Omega \int_0^t \frac{\mathrm{d}}{\mathrm{d}\,t}\mathcal{P}_{ij}(t-\tau) e_{ij}(\frac{\mathrm{d}}{\mathrm{d}\,\tau}\boldsymbol{u}(\tau))\, d\tau\, q$$
$$+\int_\Omega \mathcal{C}_{ij}\partial_j p \partial_i q + \int_\Omega q\mathcal{M}\frac{\mathrm{d}}{\mathrm{d}\,t}p + \int_\Omega q \int_0^t \mathcal{N}(t-\tau)\frac{\mathrm{d}}{\mathrm{d}\,\tau}p(\tau)\, d\tau = 0\,, \tag{21}$$

for all $\boldsymbol{v} \in V_0$ and $q \in H^1(\Omega)$.

2.3 Remarks and Numerical Illustrations

In this example we show for illustration purposes a few of the results published in [13]. We consider a cylindrical segment with the microstructure resembling the material of compact bone, see the micrograph at Figure 2 (left), with an "idealised" microstructure displayed at Figure 2 (right). The example was computed using the microscopic material parameters listed in Table 1, where μ_d and λ_d are the Lamé elasticity constants related to the solid skeleton (in the matrix and in the "porous" channels as well), α_{ij} are the stress coupling coefficients given by $\alpha_{ij}(y) \equiv \alpha_1\delta_{ij} + \alpha_2(1-\delta_{ij})$, μ is the Biot elasticity coefficient and K_{ij} is the permeability (involving the fluid viscosity). The permeability parameters of matrix are defined in the local coordinate system which is determined by the relative position of a given point w.r.t. the position of axis of the nearest Haverse channel. In the present implementation we assume parallel Haverse channels which, thus, generate just a 2D anisotropy: In any point we define the vectors $\boldsymbol{\tau}(y)$ and $\boldsymbol{\nu}(y)$ defining

Table 1. Microscopic material parameters.

coefficient	unit	in matrix, $y \in Y_m$	in channels $y \in Y_c$
$D_{ijkl}(y,t)$	GPa	$\mu_d = 3$, $\lambda_d = 17$	$\mu_d = 0.3$, $\lambda_d = 1.7$
$\alpha_{ij}(y,t)$	1	$\alpha_1 = 0.8$, $\alpha_2 = 0.05$	$\alpha_1 = 1.0$, $\alpha_2 = 0.0$
$\mu(y,t)$	GPa	7	4
$K_{ij}(y,t)$	$\mathrm{m}^2/(\mathrm{GPa\ s})$	$3\cdot 10^{-7}\,[2\nu_i(y)\nu_j(y) + \tau_i(y)\tau_j(y) + 0.2\,\delta_{3i}\delta_{3j}]$	$3\cdot 10^{-3}\delta_{ij}$

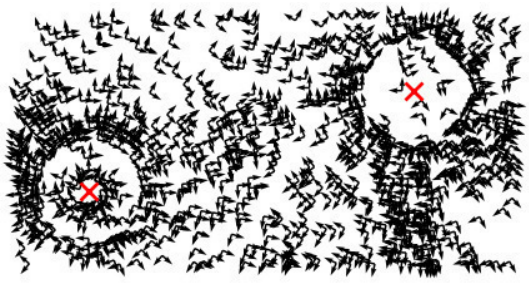

Fig. 3. The $\boldsymbol{\nu}(y)$ (radial) and $\boldsymbol{\tau}(y)$ (tangential) vectors defined for microstructure resembling the osteon. A random sampling of 1000 out of all quadrature points is shown. Top view of the RPC.

the local anisotropy axes of a particular microstructure with parallel Haverse channels, see Figure 3.
The macroscopic material parameters were obtained by the homogenisation procedure described above. For this both the stationary and time-dependent microscopic characteristic responses are needed; in Figure 4 we display se-

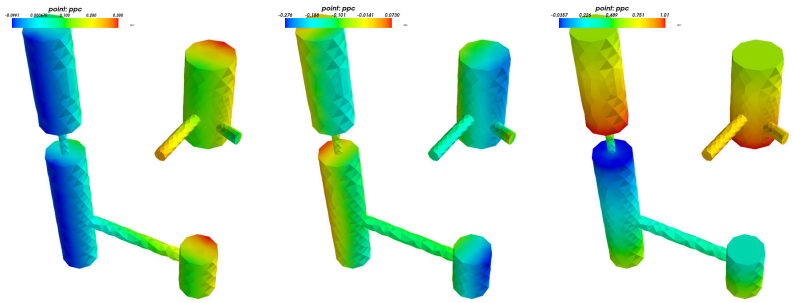

pressure correctors in channels: η^k, $k = 1, 2, 3$

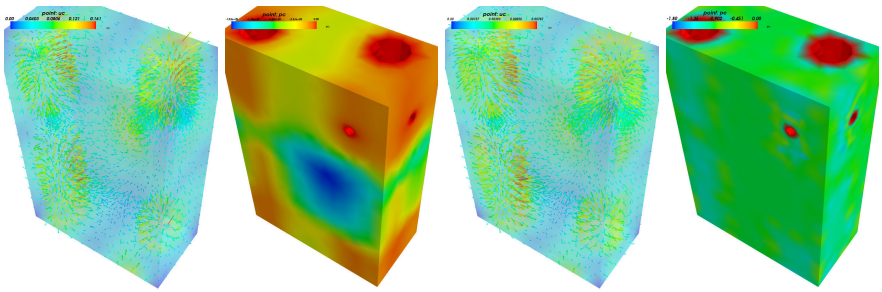

steady strain-associated correctors: $\bar{\boldsymbol{\omega}}^{rs}$, $\bar{\pi}^{rs}$ steady pressure-associated correctors: $\boldsymbol{\omega}^{*,P}$, $\tilde{\pi}^P(0)$

Fig. 4. Selected correctors solutions.

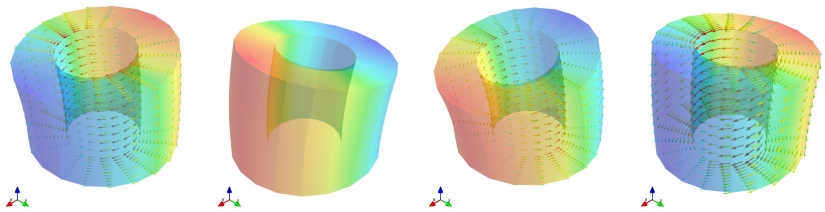

Fig. 5. Macroscopic solution in selected time steps - macroscopic deformation (magnified 2×), pressure distribution (colour scale), diffusion velocities (arrows).

lected solutions – the corrector basis functions – of the local microscopic problems solved in the reference cell Y. Using those, homogenised material parameters are computed and the macroscopic model is defined. In Figure 5 the macroscopic response of a cylindrical bone specimen is shown at different steps of loading.

3 Hierarchical Homogenisation for Canaliculo-Lacunar Porosity

The model described in the previous section is introduced in terms of material parameters characterizing the periodic "mesoscale" representing the osteons as the Biot continuum. We observed that the fading memory effects are induced in all homogenised coefficients by the microflows in the dual porosity. To describe its poroelastic properties we can use the information about its geometry and topology. Thus, to compute the material parameters at the osteon level, a homogenised model of the fluid-structure interaction in the lacuno-canalicular porosity can be used.
The pores of two different sizes – the canaliculi and lacunae, see Figure 6, are filled with a compressible fluid which can redistribute, since at both the microscopic and mesoscopic scales the pores form one system of connected channels. We apply the asymptotic homogenisation to upscale a simple microscopic fluid-structure interaction problem. The obtained poroelastic model with double-porosity describes the matrix behaviour at the mesoscopic level.

3.1 Hierarchical Approach – General Setting

We consider the steady state of a deformable porous medium saturated by a fluid, whereby the fluid drainage is controlled by a boundary flux. The porosity of the medium is formed at two levels, distinguishable by different sizes of pores, the primary and the secondary ones. They can be interconnected, or disconnected by an impermeable solid phase.

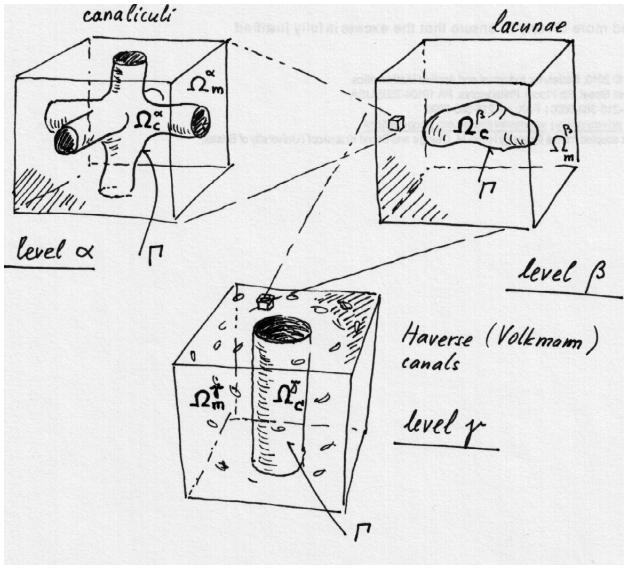

Fig. 6. Hierarchical arrangement of the dual porosity in the osteon "matrix"; levels α and β.

The two levels, further labelled by superscripts α and β are associated with two scales underlying the osteon matrix. Next we consider a "relative" micro- and macroscopic scales. At the microscopic scale of the level α, we consider an elastic solid phase called "matrix", whereas the fluid fills the "canals" (representing the canaliculi network) which can be drained, thus the fluid can be expelled from, or sucked in the higher level porosity. The behaviour of the matrix is assumed linearly elastic. The homogenisation procedure of this two-phase medium allows us to obtain a model describing the upscaled poroelastic level α.
Then, using the above mentioned (homogenised) α-poroelasticity model, we can describe the material occupying the matrix of the microstructure β; recall the relativity of the micro- and macroscales at this hierarchical homogenisation approach. At this "higher" level the canals can exchange the fluid with the microscopic pores of the α level, so that only one fluid pressure value characterises the steady state; this case corresponds to the structure of pores in the canaliculo-lacunar system of the compact bone tissue, see Figure 6. Upscaling of the β-level leads to effective poroelastic properties of the relative "macroscopic" level associated with the osteon matrix.

3.2 Homogenisation of Microscopic Scale – Upscaling Level α

At the level of canalicular porosity we consider the elastic solid phase perforated with the fluid-filled canaliculi, i.e with the canals.

3.3 Governing Equations

The geometrical configuration of the studied domain $\Omega^\alpha \subset \mathbb{R}^3$ is decomposed into the matrix and the canals occupying the domains $\Omega_m^{\alpha,\varepsilon}$ and $\Omega_c^{\alpha,\varepsilon}$, respectively, and their common boundary is $\Gamma^{\alpha,\varepsilon}$. More precisely, the following definitions are introduced

$$\Omega^\alpha = \Omega_m^{\alpha,\varepsilon} \cup \Omega_c^{\alpha,\varepsilon} \cup \Gamma^{\alpha,\varepsilon}, \quad \Omega_m^{\alpha,\varepsilon} \cap \Omega_c^{\alpha,\varepsilon} = \emptyset\,, \quad \Gamma^{\alpha,\varepsilon} = \overline{\Omega_m^{\alpha,\varepsilon}} \cap \overline{\Omega_c^{\alpha,\varepsilon}}. \tag{22}$$

The deformation of the matrix is governed by the problem involving the following equations: Find $(\boldsymbol{u}^{\alpha,\varepsilon}, \bar{p}^{\alpha,\varepsilon}) \in \mathbf{H}^1(\Omega_m^{\alpha,\varepsilon})/\mathbb{R} \times \mathbb{R}$ such that

$$\begin{aligned}
&\int_{\Omega_m^{\alpha,\varepsilon}} (\mathbb{D}^{\alpha,\varepsilon} : \boldsymbol{e}(\boldsymbol{u}^{\alpha,\varepsilon})) : \boldsymbol{e}(\boldsymbol{v}) + \bar{p}^{\alpha,\varepsilon} \int_{\Gamma_m^{\alpha,\varepsilon}} \boldsymbol{n}^{[m]} \cdot \boldsymbol{v} \, \mathrm{dS}_x \\
&\qquad = \int_{\partial_{\mathrm{ext}}\Omega_m^{\alpha,\varepsilon}} \boldsymbol{g}^{\alpha,\varepsilon} \cdot \boldsymbol{v} \, \mathrm{dS}_x + \int_{\Omega_m^{\alpha,\varepsilon}} \boldsymbol{f}^{\alpha,\varepsilon} \cdot \boldsymbol{v}\,, \\
&\int_{\partial\Omega_c^{\alpha,\varepsilon}} \tilde{\boldsymbol{u}}^{\alpha,\varepsilon} \cdot \boldsymbol{n}^{[c]} \, \mathrm{dS}_x + \gamma^\alpha \bar{p}^{\alpha,\varepsilon} |\Omega_c^{\alpha,\varepsilon}| = -J^{\alpha,\varepsilon}\,,
\end{aligned} \tag{23}$$

for all $\boldsymbol{v} \in \mathbf{H}^1(\Omega_m^{\alpha,\varepsilon})$, where $\boldsymbol{u}^{\alpha,\varepsilon}$ is the displacement vector of the matrix, $p^{\alpha,\varepsilon}$ is the fluid pressure, $\mathbb{D}^{\alpha,\varepsilon}$ is the elasticity fourth-order tensor of the matrix and γ^α is the fluid compressibility. The applied surface-force and volume-force fields are denoted respectively by $\boldsymbol{g}^{\alpha,\varepsilon}$ and $\boldsymbol{f}^{\alpha,\varepsilon}$. The outer unit normal vector of the boundary $\Omega_m^{\alpha,\varepsilon}$ is denoted by $\boldsymbol{n}^{[m]}$. Condition $(23)_2$ describes that the change of the porosity (the left-hand side term) – change of volume $|\Omega_c^{\alpha,\varepsilon}|$ is compensated by fluid compression and by the fluid out-flow $J^{\varepsilon,\alpha}$ through external boundary $\partial_{\mathrm{ext}}\Omega_c^{\alpha,\varepsilon} = \partial\Omega_c^{\alpha,\varepsilon} \cup \partial\Omega^\alpha$, i. e. outwards to Ω^α.

3.4 Homogenisation Result

Domain Ω^α is obtained from a periodic microstructure generated by the representative unit cell Y^α decomposed as follows

$$Y^\alpha = Y_m^\alpha \cup Y_c^\alpha \cup \Gamma_Y^\alpha\,, \quad Y_c^\alpha = Y^\alpha \setminus Y_m^\alpha\,, \quad \Gamma_Y^\alpha = \overline{Y_m^\alpha} \cap \overline{Y_c^\alpha}\,. \tag{24}$$

As a result, the domain Ω^α is defined by $\bigcup_{k\in\mathbb{K}^\varepsilon} \varepsilon(Y^\alpha + k)$ with $\mathbb{K}^\varepsilon = \{k \in \mathbb{Z}^3, \varepsilon(Y^\alpha + k) \subset \Omega^\alpha\}$. The upscaling procedure is described in [14].

Response at the Microscopic Scale The volume fraction of pores is defined by $\phi^\alpha = |Y_c^\alpha|/|Y^\alpha|$. We assume existence of a limit surface force $\boldsymbol{g}^\alpha$ and of a limit volume force $\boldsymbol{f}^\alpha$. Using characteristic displacements $\boldsymbol{\omega}^{ij}(y)$ and $\boldsymbol{\omega}^P(y)$, the fluctuations of displacement are described, namely $\boldsymbol{u}^1(x,y) = \boldsymbol{\omega}^{ij}(y)\partial_j u_i(x) - \boldsymbol{\omega}^P(y)\bar{p}$, where $\bar{p}$ is the constant fluid pressure in Ω^α. Functions $\boldsymbol{\omega}^{ij}(y)$ and $\boldsymbol{\omega}^P(y)$ are obtained as solutions of the following problems:

find $(\boldsymbol{\omega}^{ij}, \boldsymbol{\omega}^P) \in \mathbf{H}^1_{\#}(Y_m) \times \mathbf{H}^1_{\#}(Y_m)$ satisfying

$$\begin{aligned} a_{Y^m}\left(\boldsymbol{\omega}^{ij} + \boldsymbol{\Pi}^{ij},\, \boldsymbol{v}\right) &= 0\,, \quad \forall \boldsymbol{v} \in \mathbf{H}^1_{\#}(Y_m)\,, \\ a_{Y^m}\left(\boldsymbol{\omega}^{P},\, \boldsymbol{v}\right) &= \fint_{\Gamma_Y} \boldsymbol{v}\cdot\boldsymbol{n}^{[m]}\,\mathrm{dS}_y\,, \quad \forall \boldsymbol{v} \in \mathbf{H}^1_{\#}(Y_m)\,, \end{aligned} \tag{25}$$

where $a_{Y^m}(\boldsymbol{w},\, \boldsymbol{v}) = \fint_{Y_m} (\mathbb{D}\boldsymbol{e}_y(\boldsymbol{w})) : \boldsymbol{e}_y(\boldsymbol{v})$ and $\boldsymbol{\Pi}^{ij} = (\Pi^{ij}_k)$, $i,j,k = 1,2,3$ with $\Pi^{ij}_k = y_j\delta_{ik}$. For the sake of brevity we use the notation $Y := Y^\alpha$, thus dropping out the superscript α.

Model Obtained by Homogenisation The effective properties of the deformable porous medium are introduced using the characteristic response obtained at the microscopic scale. We define the following tensors, see [14],

$$\begin{aligned} A_{ijkl} &= a_{Y^m}\left(\boldsymbol{\omega}^{ij} + \boldsymbol{\Pi}^{ij},\, \boldsymbol{\omega}^{kl} + \boldsymbol{\Pi}^{kl}\right), \\ B_{ij} &= -\fint_{Y_m} \mathrm{div}_y \boldsymbol{\omega}^{ij}\,, \quad \hat{\boldsymbol{B}} := \boldsymbol{B} + \phi\boldsymbol{I}\,, \\ M &= a_{Y^m}\left(\boldsymbol{\omega}^{P},\, \boldsymbol{\omega}^{P}\right). \end{aligned} \tag{26}$$

Obviously, the tensors $\mathbb{A} = (A_{ijkl})$ and $\boldsymbol{B} = (B_{ij})$ are symmetric; moreover $\mathbb{A}$ is positive definite and $M > 0$.

Model of the Poroelasticity At this first-level of the homogenisation process, we obtain the model of the poroelasticity governing the skeleton displacements $\boldsymbol{u} \in \mathbf{H}^1(\Omega)$ defined in Ω and fluid pressure $\bar{p} \in \mathbb{R}$ which verify the following equations

$$\begin{aligned} &\int_\Omega \left(\mathbb{A}\boldsymbol{e}_x(\boldsymbol{u}) - \bar{p}\hat{\boldsymbol{B}}\right) : \boldsymbol{e}_x(\boldsymbol{v}) = \int_\Omega (1-\phi)\boldsymbol{f}\cdot\boldsymbol{v} + \int_{\partial\Omega} (1-\phi_S)\boldsymbol{g}\cdot\boldsymbol{v}\,\mathrm{dS}_x\,, \\ &\int_\Omega \hat{\boldsymbol{B}} : \boldsymbol{e}_x(\boldsymbol{u}) + \bar{p}(M+\phi\gamma)|\Omega| = -J \end{aligned} \tag{27}$$

for all $\boldsymbol{v} \in \mathbf{H}^1(\Omega)$, where J is the limit of the total flux $J^{\alpha,\varepsilon}$ outwards Ω^α. Note that all $\mathbb{A}, \hat{\boldsymbol{B}}, M, \phi, \phi_S$ and J are associated with upscaling from level α, therefore, they will be further labeled by superscript α.

3.5 Homogenisation of Mesoscopic Scale – Upscaling Level β

At the second upscaling stage, we consider the homogenised matrix associated with (27), now corresponding to the lacunar porosity level. Thus, the fluid-filled channels represent the lacunae. The geometrical configuration of the relative microstructure consists of two compartments: 1) the *matrix* $\Omega^{\beta,\varepsilon}_m$

which is formed by the porous medium associated with the upscaled microstructure of level α, 2) the *channels* $\Omega_c^{\beta,\varepsilon}$ which are filled with fluid and connected with pores of level α through the interface $\Gamma_m^{\beta,\varepsilon}$. Recall that the dimensionless parameter $\varepsilon \to 0$ now describes the ratio between the characteristic sizes of the lacunae and of the whole osteon.

Description at the Mesoscopic Scale Level As the description of the domain Ω^α, the domain Ω^β at the mesoscopic scale is split as follows: $\Omega^\beta = \Omega_m^{\beta,\varepsilon} \cup \Omega_c^{\beta,\varepsilon} \cup \Gamma^{\beta,\varepsilon}$, where $\Gamma^{\beta,\varepsilon}$ designates the interface between the subdomains. The structure is loaded on $\partial_{\rm ext}\Omega_m^{\beta,\varepsilon} = \partial\Omega^\beta \cap \partial\Omega_m^{\beta,\varepsilon}$ by a surface-force field $\hat{\boldsymbol{g}}^\alpha = \boldsymbol{g}^\alpha(1-\phi_S^\alpha)$ and by a volume-force field $\hat{\boldsymbol{f}}^\alpha = (1-\phi^\alpha)\boldsymbol{f}^\alpha$ acting on the matrix and drained on $\partial_{\rm ext}\Omega_c^{\beta,\varepsilon}$. The total outflow from Ω^β is $J^{\beta,\varepsilon}$; it incorporates the flux from the microporosity α through $\partial_{\rm ext}\Omega_m^{\beta,\varepsilon}$ and from the mesoscopic channels through $\partial_{\rm ext}\Omega_c^{\beta,\varepsilon}$. Note that on the interior part of $\partial\Omega_m^{\beta,\varepsilon}$ surface-force $\boldsymbol{g}$ considered in (27) is represented by the interstitial pressure in the β-porosity. So, the displacement $\boldsymbol{u}^{\beta,\varepsilon} \in \mathbf{H}^1(\Omega_m^{\beta,\varepsilon})$ and the pressure $\bar{p}^\varepsilon \in \mathbb{R}$ must satisfy the equation

$$\int_{\Omega_m^{\beta,\varepsilon}} \Big(\mathbb{A}^\alpha \boldsymbol{e}(\boldsymbol{u}^{\beta,\varepsilon}) - \bar{p}^\varepsilon \hat{\boldsymbol{B}}^\alpha\Big) : \boldsymbol{e}(\boldsymbol{v}) + \bar{p}^\varepsilon \int_{\Gamma^{\beta,\varepsilon}} (1-\phi_S^\alpha)\boldsymbol{v}\cdot\boldsymbol{n}^{[m]}\,\mathrm{dS}_x = \int_{\partial_{\rm ext}\Omega_m^{\beta,\varepsilon}} \hat{\boldsymbol{g}}^\alpha\cdot\boldsymbol{v}\,\mathrm{dS}_x + \int_{\Omega_m^{\beta,\varepsilon}} \hat{\boldsymbol{f}}^\alpha\cdot\boldsymbol{v}\,, \quad \forall\,\boldsymbol{v}\in\mathbf{H}^1(\Omega_m^{\beta,\varepsilon}), \tag{28}$$

and the volume conservation

$$\int_{\Omega_m^{\beta,\varepsilon}} \hat{\boldsymbol{B}}^\alpha : \boldsymbol{e}(\boldsymbol{u}^{\beta,\varepsilon}) + (1-\phi_S^\alpha)\int_{\partial\Omega_c^{\beta,\varepsilon}} \widetilde{\boldsymbol{u}^{\beta,\varepsilon}}\cdot\boldsymbol{n}^{[c]}\,\mathrm{dS}_x + \bar{p}^\varepsilon[(M^\alpha+\gamma\phi^\alpha)(1-\phi^{\beta,\varepsilon})+\gamma\phi^{\beta,\varepsilon}]|\Omega^\beta| = -J^\beta\,, \tag{29}$$

where we used the displacement extension $\widetilde{\boldsymbol{u}^{\beta,\varepsilon}}$ to channels $\Omega_c^{\beta,\varepsilon}$. We recall $1-\phi^{\beta,\varepsilon} = |\Omega_m^{\beta,\varepsilon}|/|\Omega^\beta|$, where $\phi^{\beta,\varepsilon} \to \phi^\beta := |Y_c^\beta|/|Y^\beta|$.

Homogenised Problem at the β Level Analysis of problem (28)-(29) when $\varepsilon \to 0$ leads to equations involving effective poroelastic properties of the 2nd level which are evaluated using the characteristic responses $\boldsymbol{\omega}^{ij}$ and $\boldsymbol{\omega}^P$.

In analogy with the level α, let $Y^\beta = Y_m^\beta \cup Y_c^\beta \cup \Gamma_Y^\beta$ be the reference periodic cell. The following local problems must be solved: find $\boldsymbol{\omega}^{ij}, \boldsymbol{\omega}^P \in \mathbf{H}^1_\#(Y_m^\beta)$, $i,j=1,2,3$, such that

$$\begin{aligned} &\int_{Y_m^\beta} [\mathbb{A}^\alpha \boldsymbol{e}_y(\boldsymbol{\omega}^{ij}+\boldsymbol{\Pi}^{ij})] : \boldsymbol{e}_y(\boldsymbol{v}) = 0\,, \quad \forall \boldsymbol{v}\in\mathbf{H}^1_\#(Y_m^\beta)\,, \\ &\int_{Y_m^\beta} [\mathbb{A}^\alpha \boldsymbol{e}_y(\boldsymbol{\omega}^P)] : \boldsymbol{e}_y(\boldsymbol{v}) = -\int_{Y_m^\beta} \hat{\boldsymbol{B}}^\alpha : \boldsymbol{e}_y(\boldsymbol{v}) + \int_{\Gamma_Y^\beta} (1-\phi_S^\alpha)\boldsymbol{v}\cdot\boldsymbol{n}^{[m]}\,\mathrm{dS}_y \end{aligned} \tag{30}$$

for all $\boldsymbol{v} \in \mathbf{H}^1_{\#}(Y_m^\beta)$. In what follows by $\boldsymbol{\omega}^{ij}$ and $\boldsymbol{\omega}^P$ we mean the solutions of (30) and not that of (25), in spite of the same notation. While the solutions of $(30)_1$ express fluctuations with respect to the unit strain of the macroscopic scale, the solutions of $(30)_2$ interpret the local response with respect to the unit pressure.
The effective poroelasticity properties of the upscaled mesoscale are represented by $\mathbb{A}^\beta = (A^\beta_{ijkl})$, $\boldsymbol{B}^\beta = (B^\beta_{ij})$ and M^β, given as follows

$$\begin{aligned} A^\beta_{ijkl} &= \int_{Y_m^\beta} [\mathbb{A}^\alpha \boldsymbol{e}_y(\boldsymbol{\omega}^{kl} + \boldsymbol{\Pi}^{kl})] : \boldsymbol{e}_y(\boldsymbol{\omega}^{ij} + \boldsymbol{\Pi}^{ij}) \,, \\ B^\beta_{ij} &= \int_{Y_m^\beta} \hat{\boldsymbol{B}}^\alpha : \boldsymbol{e}_y(\boldsymbol{\omega}^{ij} + \boldsymbol{\Pi}^{ij}) - (1 - \phi_S^\alpha) \fint_{Y_m^\beta} \mathrm{div}_y \boldsymbol{\omega}^{ij} \,, \\ M^\beta &= \int_{Y_m^\beta} [\mathbb{A}^\alpha \boldsymbol{e}_y(\boldsymbol{\omega}^P)] : \boldsymbol{e}_y(\boldsymbol{\omega}^P) \,. \end{aligned} \tag{31}$$

The response of the homogenised medium at macroscopic scale, i. e. upscaled mesoscale for $\varepsilon \to 0$, is represented by displacement field $\boldsymbol{u} \in \mathbf{H}^1(\Omega^\beta)$ and by the constant pressure $\bar{p} \in \mathbb{R}$ satisfying

$$\begin{aligned} \int_{\Omega^\beta} \left(\mathbb{A}^\beta \boldsymbol{e}_x(\boldsymbol{u}) - \bar{p} \hat{\boldsymbol{B}}^\beta \right) : \boldsymbol{e}_x(\boldsymbol{v}) &= \int_{\partial\Omega^\beta} (1 - \phi_S^\beta) \hat{\boldsymbol{g}}^\alpha \cdot \boldsymbol{v} \, \mathrm{dS}_x + \int_{\Omega^\beta} (1 - \phi^\beta) \hat{\boldsymbol{f}}^\alpha \cdot \boldsymbol{v} \,, \\ \int_{\Omega^\beta} \hat{\boldsymbol{B}}^\beta : \boldsymbol{e}_x(\boldsymbol{u}) + \bar{p} |\Omega^\beta| \hat{M}^\beta &= -J^\beta \,, \end{aligned} \tag{32}$$

for all $\boldsymbol{v} \in \mathbf{H}^1(\Omega^\beta)$ where

$$\begin{aligned} \hat{\boldsymbol{B}}^\beta &:= (1 - \phi_S^\alpha) \phi^\beta \boldsymbol{I} + \boldsymbol{B}^\beta \,, \\ \hat{M}^\beta &:= M^\beta + \phi^\beta \left[(M^\alpha + \gamma \phi^\alpha)(1 - \phi^\beta) + \gamma \phi^\beta \right] . \end{aligned} \tag{33}$$

3.6 Biot Poroelasticity Model for the Canaliculo-Lacunar Porosity by Upscaling

The coefficients involved in the macroscopic formulation (32) can be identified with the standard Biot poroelasticity model: indeed, we obtained equations of the 2-level homogenised poroelasticity

$$\begin{aligned} \boldsymbol{\sigma} &= \mathbb{A} \boldsymbol{e} - \hat{\boldsymbol{B}} p \,, \\ \zeta &= \hat{\boldsymbol{B}} : \boldsymbol{e} + \hat{M}(p - p_0) \,, \end{aligned} \tag{34}$$

where $\boldsymbol{\sigma} = (\sigma_{ij})$ is the total stress, p is the fluid pressure (assuming the reference pressure $p_0 := 0$), $\boldsymbol{u} = (u_i)$ is the displacement with respect to reference state, ζ is the fluid content increase (per unit volume with respect to the reference state). Thus, $\hat{\boldsymbol{B}}$ are the Biot stress coupling coefficients,

$\mathbb{A}$ is the effective elasticity stiffness, i. e. associated with the (drained) solid skeleton, and $\hat{M}$ expresses the overall Biot compressibility which incorporates both the fluid compressibility and the skeleton compressibility w.r.t. the fluid pressure increase.
It should be remarked that the definitions of the homogenised coefficients involved in (34) were introduced upon the assumption of locally constant pressure, thus excluding any fluid flow. Such conditions are also considered in experiments which are used to measure the coefficients of the Biot model. However, we can assume moderate pressure gradients on the (relative) macroscopic scale, thus, allowing for a "slow" fluid flow which does not induce pressure oscillations on characteristic scales of the microstructures. In other words, we neglected the fluid-structure interaction effects associated to flow dynamic effects, namely the "microscopic" pressure oscillations and the wall shear stress induced by flow of a viscous fluid.

Poroelasticity of the Canaliculo-Lacunar Porosity The idea is to use the two-level upscaling procedure resulting in the constitutive laws (34) with (33) and (26), (31) to introduce the material parameters of the osteon matrix occupying domain Y_m, see (5). Thus, for a given geometry of the representative periodic cells describing the canalicular porosity (level α) and the lacunae (level β) we can compute $D^m_{ijkl} := A_{ijkl}$, $\alpha^m_{ij} := \hat{B}_{ij}$ and $1/\mu^m := M$.
Although in this section we considered the static case only, so that no pressure gradients were considered, a slow flow leading to small pressure gradients can be covered by the model presented in (34); for this the fluid increase can be expressed by the Darcy flow. Namely, we can put $\zeta = -\mathrm{div}\boldsymbol{w} = \mathrm{div}(\boldsymbol{K}\nabla p)$ with the permeability $\boldsymbol{K} = (K_{ij})$ resulting from the homogenisation of the Stokes problem in $\Omega_c^{\beta,\varepsilon}$, whereas the flow in the dual porosity would be negligible. However, the permeability K^m_{ij} employed in (5) could be obtained more genuinely, as follows. Using homogenisation of the Stokes flow at level α, we would obtain the Darcy flow in the "matrix" of level β. The subsequent homogenisation step would give permeability coefficients which govern the Darcy flow in the dual porosity embedding the lacunae. Details will be described in a further publication.

3.7 Numerical Illustrations

In this section we present an example of upscaling with two microlevels α, β. The material properties are given just by the stiffness $\mathbb{D}^\alpha$ at the heterogeneous level α. The homogenised materials are then characterised by stiffness A^l_{ijkl}, Biot coefficients B^l_{ij} and Biot modulus M^l, $l = \alpha, \beta$.
The hierarchical procedure is intended to describe the osteon matrix and we shall pursue this alternative in future research. However, in the present example we consider the heterogeneous level β corresponding to the osteons, so that the upscaled model is relevant to the macroscopic scale where a specimen of the whole compact bone is loaded. Therefore, at the heterogeneous

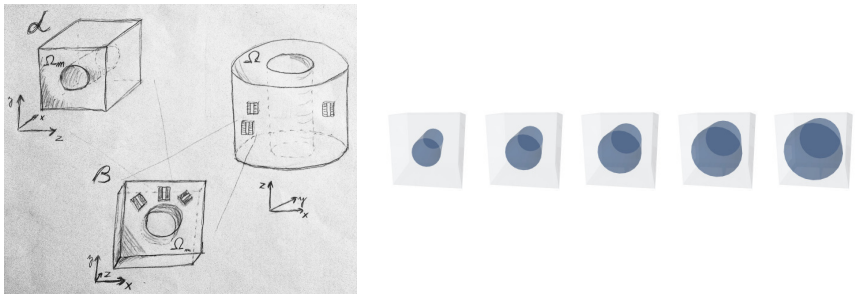

Fig. 7. Left: Two micro levels: α, β, macro level with β microstructure. Right: Microstructure channel radii in 20% – 40% of the reference cell size (= 1).

level β the upscaled microstructure from the level α is distributed in a local coordinate system and the homogenised material parameters of level α have to be transformed accordingly.

Both microlevels make use of the same reference cell geometry: a cube with cylindrical channel aligned with one axis. Here we show a simple parametric study demonstrating how change in the channel radius (simultaneously at α, β), see Figure 7 (right), influences the corrector solutions at α, β and consequently the homogenised material parameters as well as the macroscopic solutions of the homogenised problem (32) obtained for microstructures with different porosities, see Figure 7 (left).

Quantitative results are shown in Figure 8. Obviously, as the channel increases, the stiffness of the material decreases, leading to larger displacements and pressure. Illustrative results are shown in Figure 9.

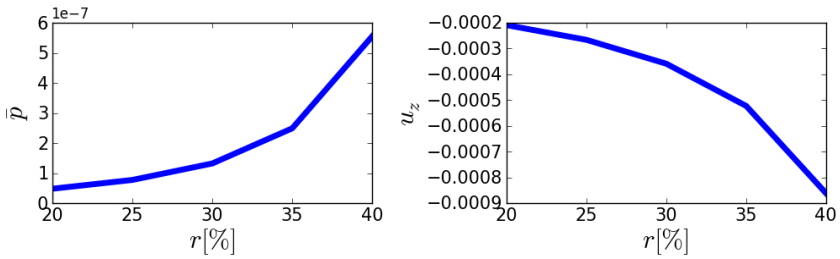

Fig. 8. Macroscopic pressure (left) and top displacement (right) depending on channel radius.

3.8 Conclusion

Using the hierarchical homogenisation, we developed the upscaled model of a nested poroelastic material, often called the "double-porosity" model. Since the model is intended to describe hierarchical structure of pores in the

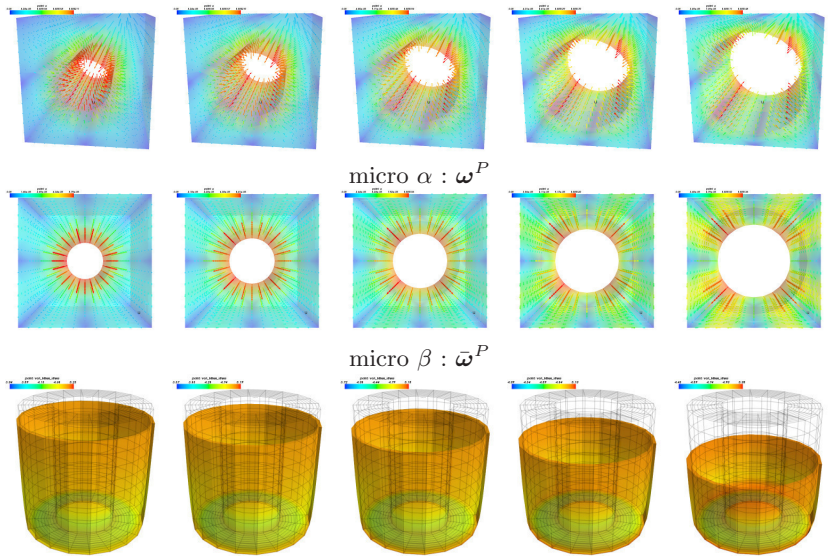

Fig. 9. Selected quantities of corrector solutions and macroscopic solution, depending on channel radius.

canaliculo–lacunar porosity, we consider two "microscopic" levels with connected pores [14]; as the result is for a static problem there is just one scalar fluid pressure associated with all levels. Formally the same expressions for the poroelastic coefficients and the same microscopic equations can be obtained for the case of closed inclusions, but then the pressure is a (macroscopic) field, i. e. $p = p(x)$, cf. [3].

The homogenisation procedure reported in this paper makes possible to treat an arbitrary geometry and topology of the pores, whereby the localization tensors and coefficients can be calculated as the response of the autonomous microscopic problems.

Further research will be focused on the numerical studies with real data describing the bone geometry at the level of osteons and with material data known from the literature. In [12] and [13] we proposed an algorithm for a solution recovery of the microscopic response on the osteon level. Using the homogenisation approach we establish a straightforward link between the mechanics valid on the microscopic level and the macroscopic behaviour which can be used to simulate experiments on tissue samples. Therefore, using inverse analyses formulated as optimization problems the microscopic material constants can be identified.

Acknowledgements. The research is supported by projects GACR 106/09/0740 of the Czech Republic and in part by the European Regional Devel-

opment Fund (ERDF), project "NTIS - New Technologies for Information Society", European Centre of Excellence, CZ.1.05/1.1.00/02.0090.

References

[1] Arbogast, T.; Douglas, J. & Hornung, U.: Derivation of the double porosity model of single phase flow via homogenization theory. *SIAM Journal on Mathematical Analysis* **21** (1990), 823–836.

[2] Auriault, J.-L. & Boutin, C.: Deformable porous media with double porosity. Quasi statics. I. Coupling effects. *Transport in Porous Media* **7** (1992), 63–82.

[3] Baffico, L.; Grandmont, C.; Maday, Y. & Osses, A.: Homogenization of elastic media with gaseous inclusions. *SIAM Multiscale Modeling and Simulation* **7** (2008), 432–465.

[4] Cioranescu, D.; Damlamian, A. & Griso, G.: The periodic unfolding method in homogenization. *SIAM Journal on Mathematical Analysis* **40** (2008), 1585–1620.

[5] Cowin, S. C.: *Bone mechanics handbook*. CRC Press, Boca Raton, FL 2001, 2nd edn.

[6] De Boer, R.: Contemporary progress in porous media theory. *Applied Mechanics Reviews* **53** (2000), 323–370.

[7] Gururaja, S.; Kim, H. J.; Swan, C. C.; Brand, R. A. & Lakes, R. S.: Modeling deformation-induced fluid flow in cortical bone's lacunar-canalicular system. *Annals of Biomedical Engineering* **33** (2005), 7–25.

[8] Hellmich, C.; Barth-Bélémy, J.-F. & Dormieux, L.: Mineralcollagen interactions in elasticity of bone ultrastructure a continuum micromechanics approach. *European Journal of Mechanics A/Solids* (2004), 783–810.

[9] Hornung, U.: *Homogenization and porous media*. Springer, Berlin 1997.

[10] Lemaire, T.; Naili, S. & Rémond, A.: Multi-scale analysis of the coupled effects governing the movement of interstitial fluid in cortical bone. *Biomechanics and Modeling in Mechanobiology* **5** (2006), 39–52.

[11] Rémond, A. & Naili, S.: Cyclic loading of a transverse isotropic poroelastic cylinder: a model for the osteon. *Comptes Rendus Mecanique* **332** (2004), 759–766.

[12] Rohan, E. & Cimrman, R.: Two-scale modelling of tissue perfusion problem using homogenization of dual porous media. *International Journal for Multiscale Computational Engineering* **8** (2010), 81–102.

[13] Rohan, E. & Cimrman, R.: Multiscale FE simulation of diffusion-deformation processes in homogenized dual-porous media. *Mathematics and Computers in Simulation* (2011), in Press.

[14] Rohan, E.; Naili, S.; Cimrman, R. & Lemaire, T.: Hierarchical homogenization of fluid saturated porous solid with multiple porosity scales. *Comptes Rendus Mecanique* (2012), submitted.

[15] Rohan, E.; Naili, S.; Cimrman, R. & Lemaire, T.: Multiscale modelling of a fluid saturated medium with double porosity: Relevance to the compact bone. *Journal of the Mechanics and Physics of Solids* **60** (2012), 857–881.

[16] Zysset, P. K.: A review of morphology-elasticity relationships in human trabecular bone: theories and experiments. *Journal of Biomechanics* **36** (2003), 1469–1485.

Refining a Bottom-up Computational Approach for Spider Silk Fibre Mechanics

S. P. Patil[1,2], B. Markert[2] & F. Gräter[1]

[1] Molecular Biomechanics,
Heidelberg Institute for Theoretical Studies, 69118 Heidelberg, Germany
[2] Institute of Applied Mechanics (CE), Chair of Continuum Mechanics,
University of Stuttgart, Pfaffenwaldring 7, 70569 Stuttgart, Germany

Abstract. Spider silk has attracted the attention of many scientists due to its combination of high strength, ductility, and light weight. Spider silk has a semi-crystalline structure consisting of stiff β-sheet crystals surrounded by amorphous glycine-rich domains. We present an overview on these mechanical properties of spider silks, and introduce a continuum mechanics-based finite element model to study silk structure and the material properties of each component in the spider silk. Here, we focus on recent refinements in this finite element model, including plastic and viscous effects of the crystalline and the amorphous phases, respectively. The ultimate goal of studying the properties of this amazing material is to find ways to design an artificial material with similar properties.

1 Introduction

The spider webs can take a variety of forms, with one of the most common type being the orb-web. The different families of spiders like *Araneus* or *Nephila* build orb-webs, while other families of spiders construct tangle and sheet webs [8, 22]. Orb-web spinning spiders produce a number of different high performance structural fibres (see Figure 1). These fibres have excel-

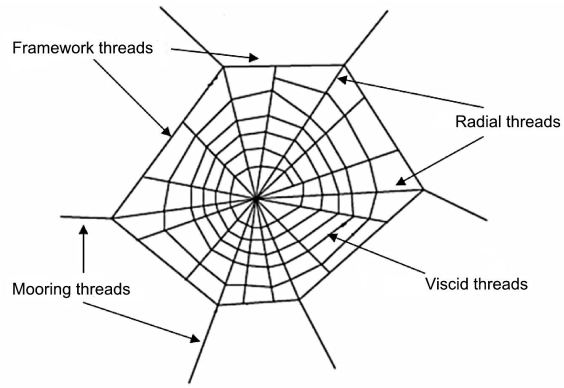

Fig. 1. Schematic diagram of a spider web.

lent mechanical properties, which are comparable to the very best synthetic fibres produced today. The dragline, minor ampullate and viscid silks form the major portions of the orb-web. The dragline silk is dominating the web structure, which occurs in the form of mooring threads, framework and pretensioned radial threads [11]. Different threads of spider silks in the web are capable to withstand adverse conditions and impact created by fast moving prey. The perfume-coated dragline helps to find their mates, swing from place to place, or store the food and eggs [28].
Minor ampullate silk has a high elasticity and low strength and it is produced by median spinneret [20]. Viscid silks produced by the flagelliform glands of *Nephila Clavipes* are highly compliant.

1.1 Mechanical Properties and Applications of Spider Silk

Many biologists and material scientists have been fascinated by the extraordinary mechanical properties of spider silk. Its strength and toughness are superior to those of common metallic and non-metallic structural materials. Table 1 compares Young's modulus, strength and energy to break of different materials. The dragline spider silk protein is a relatively soft material compared to most metals and alloys, which have a comparable Young's modulus of about 10 GPa. Nevertheless, its yield strength is about 1 GPa, which is half of high tensile steel, but a toughness estimated to be close to 10^5 J/kg, which is 100 times of that of high tensile steel. Silk is frequently compared to Kevlar, the material used for bulletproof vests. Although the tensile strength of spider silk is a factor of four less than that of Kevlar (4 GPa), the energy it takes to break silk is about three times greater (10^5 J/kg). Even some extremely soft proteins, like spider viscid silk, possess remarkable combinations of yield strength and toughness. The Young's modulus of spider viscid silk is only 3 MPa, but its yield strength is about 0.5 GPa and its toughness is about 10^5 J/kg. To summarise the mechanical properties of spider silk, it is stronger than steel, tougher than Kevlar, and more resilient than its synthetic

Table 1. Mechanical properties for selected materials [12].

material	Young's modulus [N/m^2]	strength [N/m^2]	energy to break [J/kg]
dragline spider silk	$1 \cdot 10^{10}$	$1 \cdot 10^{9}$	$1 \cdot 10^{5}$
Kevlar	$1 \cdot 10^{11}$	$4 \cdot 10^{9}$	$3 \cdot 10^{4}$
cellulose fibres	$3 \cdot 10^{10}$	$8 \cdot 10^{8}$	$9 \cdot 10^{3}$
high tensile steel	$2 \cdot 10^{11}$	$2 \cdot 10^{9}$	$1 \cdot 10^{3}$
tendon	$1 \cdot 10^{9}$	$1 \cdot 10^{8}$	$5 \cdot 10^{3}$
bone	$2 \cdot 10^{10}$	$2 \cdot 10^{8}$	$3 \cdot 10^{3}$
rubber	ca. 10^{6}	$1 \cdot 10^{8}$	$8 \cdot 10^{4}$
viscid silk	$3 \cdot 10^{6}$	$5 \cdot 10^{8}$	$1 \cdot 10^{5}$

rivals.
A range of applications of spider silk has been envisioned. Spider silk protein can be used to coat medical implants for better performance and biocompatibility [21]. Due to its low inflammatory potential and antithrombic nature, it can be used for surgical thread, biomembranes, and scaffolds for tissue engineering [2, 17]. Recombinant spider silk has potential applications in sutures for eye surgery, artificial tendon, ligaments for knee construction [14, 16]. The ability to dissipate energy at very high strain rates makes spider silk suitable for body armour systems and ideal for ballistic protection [3, 18]. Spider silk of *Nephila madagascariensis* can be used as hollow optical fibres to carry light beams in nanoscale optical circuits or as nanoscale test tubes [19].

1.2 Silk Structure

Natural spider silk is composed of several proteins with repetitive sequence motifs [10, 30]. These motifs are composed of a polyalanine $(A)_n$ or polyalanylglycine segment $(AG)_n$, where n ranges from 6 to 9 amino acids [13]. These short peptides organise themselves into mechanically strong crystal blocks measuring 2-5 nm on a side [9]. These are called crystalline subunits and constitute 10-25% of the fibre volume in spider silk [13, 23]. These polyalanine segments are followed by glycine-rich regions made of $(GGX)_n$ segments and similar motifs, where n ranges from 16 to 20 [13], and X is any amino acid. This is called amorphous phase, which is predominantly disordered [1, 7, 10]. The longer peptide sequences are oriented along the fibre axis in stretching experiments [5, 13, 26].
The excellent mechanical properties of spider silk have been attributed to the specific secondary structures of proteins in the repeating units of spider silk proteins [20], which assemble into a hierarchical structure as shown in a simplified sketch in Figure 2.
The goal of our work is to understand the mechanical properties of spider silk fibres using a continuum mechanics-based finite element method approach.

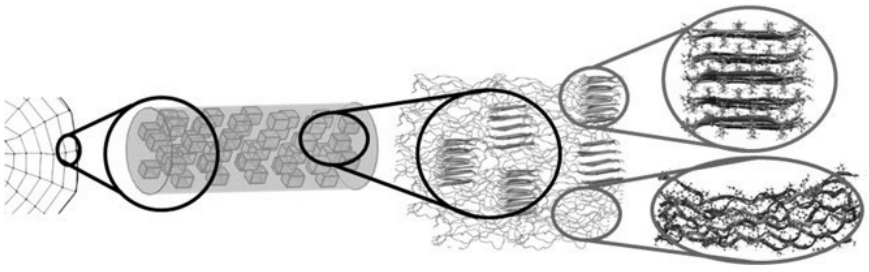

Fig. 2. Schematic diagram of the spider silk architecture from macroscale to nanoscale. Spider silk fibres are composed of crystalline subunits made of β-sheets (dark grey) and semiextended disordered peptide chains (light grey) [4].

We know the mechanical properties of spider silk at the nanoscale from atomistic molecular dynamics (MD) simulations of individual and coupled subunits [4, 29]. Termonia's network model [25] relies on molecular modelling of crystalline and amorphous phases. This model shows that the high stiffness and yield strength of dragline spider silk are due to the β-sheet crystals, whereas the high extensibility comes from the amorphous glycine-rich domains. But this model fails to predict the Young's modulus of spider silk from those of the constituents. For a quantitatively correct prediction of a fibre's macroscopic mechanical response, a bottom-up approach is needed that links molecular structure to fibre mechanics. Here, the following important points are considered in our finite element and material modelling approach of spider silk: plastic and viscoelastic properties of crystal and amorphous components, respectively, mesh convergence study, and 2-d and 3-d finite element models. As such, this study presents a few steps forward towards predictive silk fibre modelling.

2 Finite Element Modelling

2.1 A Comparison between COMSOL and LS-DYNA for Fibre Models

In our previous study, all finite element simulations of fibre models were performed with the COMSOL Multiphysics simulation software package [4]. COMSOL has some limitations, e. g. the extensive memory requirement for solving models, limited choices in modelling 3-d contacts, not user friendly for UMAT subroutine. To overcome these limitations, we used the LS-DYNA finite element analysis software for our present work. In the present study, finite element analysis of the fibre models with COMSOL are referred to as old models and with LS-DYNA are referred to as new models.
Depending on the crystal arrangement in the amorphous phase, the fibre model can be divided into three categories [4], a serial (lamellar-like) arrangement of the crystalline and amorphous subunits (see Figure 3a), a parallel

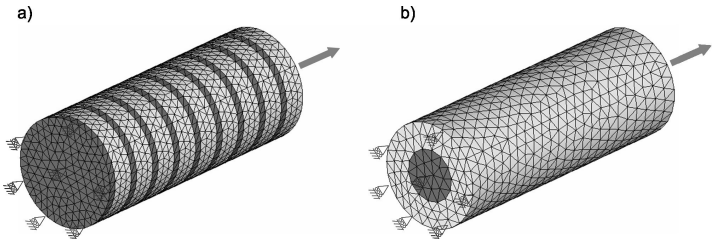

Fig. 3. Finite element silk fibre models of a) serial arrangement and b) parallel arrangement with the boundary constraints and the loading. The crystal component shown in dark grey and the amorphous phase in light grey.

Table 2. Comparison of finite element models: old fibre model (COMSOL) and new fibre model (LS-DYNA).

	parallel arrangement		serial arrangement	
	Old model (COMSOL)	New model (LS-DYNA)	Old model (COMSOL)	New model (LS-DYNA)
displacement [nm]	1	1	0.72	0.72
stress [GPa]	2.510	2.502	0.277	0.271

(longitudinal) arrangement (see Figure 3b) and a random arrangement between these two extremes. For this comparison study, we have considered the serial and parallel arrangements. Both fibre models are 39 nm long with a 14 nm diameter of circular cross section. Table 2 shows the displacement and stress results of the old model (COMSOL) and the new model (LS-DYNA). For both models, linear elastic Hooke's material law was considered. The material parameters for the crystal component ρ=1200 kg/m^3, E=80 GPa, ν=0.42 and for the amorphous component ρ=1200 kg/m^3, E=2.7 GPa, ν=0.31 were considered in both models. For both models, tetrahedral elements were considered with 0.6 nm element size. The loading and boundary conditions are shown in Figure 3. The values in Table 2 show that both finite element codes produce nearly the same results.

2.2 Mesh Convergence Study

Applying the finite element method, the mesh plays a crucial role in the numerical simulation. In general, a finer finite element discretisation yields a better approximation and more accurate calculation result. However, it has always been a question: what is the resolution of the finite element mesh that provides reasonably accurate results? Therefore, it is very important to check the mesh independency of the numerical simulation model. The refinement of the spatial discretisation in the finite element method can be accomplished in two ways: first by dividing elements into smaller ones (h-refinement) and by increasing their polynomial degree (p-refinement). In the present work, the mesh refinement is obtained by h-refinement. To study mesh independency, we have considered 3-d linear hexahedral (brick8) and tetrahedral (tetra4) element types, as well as different element sizes, see Figure 4. Our results show:

- Element type: Comparing the mechanical response of the elements, the tetra4 elements used in LS-DYNA appeared to be stiffer than the brick8 elements. These differences are small when compared at very small mesh size. However, the hexahedral elements are costlier than the tetrahedral elements, because their nodes exhibit greater connectivity, leading to denser matrices (computational cost of brick8 element model is about

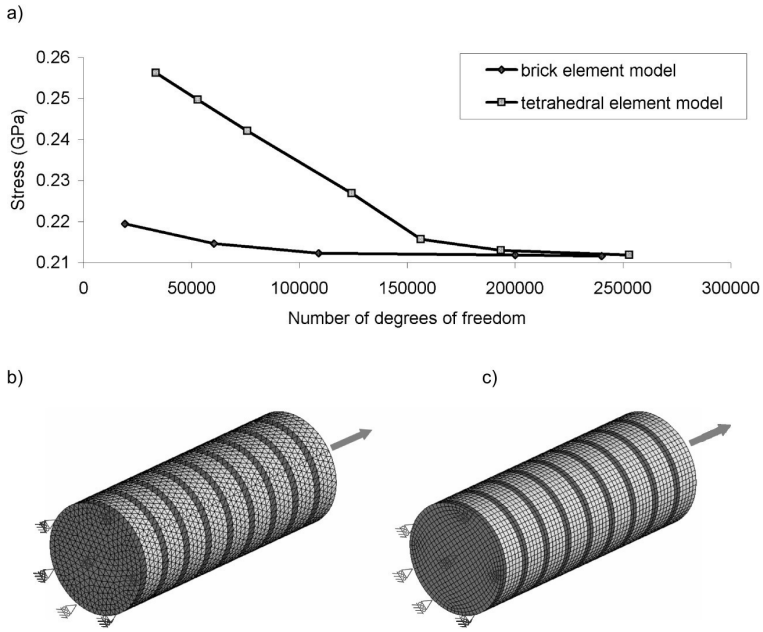

Fig. 4. Mesh convergence: a) Stress vs. number of degrees of freedom curves, b) tetrahedral (tetra4) element model, c) hexahedral (brick8) element model.

1.5 times higher than tetra4 element model in the case of the LS-DYNA viscoelastic material *MAT_006).

- Mesh size: Ideally for very fine meshes tetra4 and brick8 elements show the same result independent of computing costs. As the mesh size decreases, the stress values for the tetra4 discretisation decrease significantly compared to the brick8 elements.

The results obtained (cf. Figure 4) indicate that linear hexahedral elements are the elements of choice to represent our fibre finite element model, even though they are difficult to generate due to the random distribution of crystals in the amorphous phase.

2.3 3-d Finite Element Fibre Model

In the primary structure of spider silk, amino acids are linked into peptide chain proteins by the peptide bonds. It can be seen that the silk proteins consist of repeating units. The secondary structure refers to highly regular local sub-structures. It is one level above the primary structure. The commonly observed secondary structures are parallel and antiparallel β-sheets. Initially, secondary structures of the spider silk were studied using X-ray diffraction [9] and Fourier transform infrared measurements [31]. The spider silk was found to be a semi-crystalline structure consisting of stiff β-sheet crystals

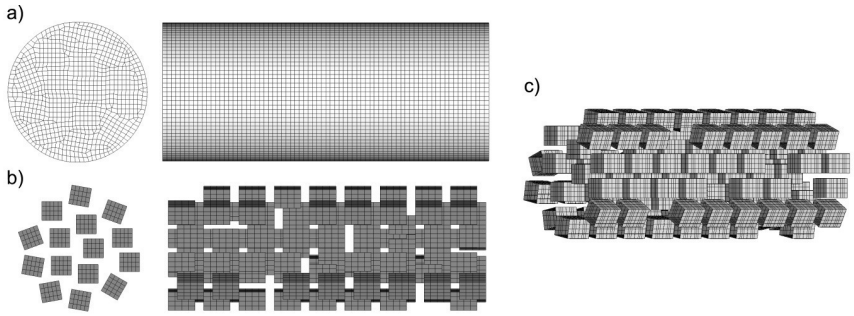

Fig. 5. 3-d finite element model: a) Amorphous component in cylinder shape shown as side view (left) and front view (right), b) crystal solid blocks placed randomly in the amorphous component shown as side view (left) and front view (right), c) surfaces of amorphous phase (light grey) in contact with surfaces of crystals (dark grey).

surrounded by amorphous glycine-rich domains (Section 1.2).
We propose a continuum mechanics-based 3-d finite element model, where the stiff β-sheet crystals are considered as solid blocks, having similar mechanical behaviour. The geometrical dimensions of the crystal blocks are obtained from the all atom models [29]. The second component is the amorphous phase, which is the remaining domain in silk. In the silk fibre model, crystals are connected to the amorphous phase along the fibre axis direction. In the direction perpendicular to the fibre axis, there are no connections between crystals and amorphous phase. Therefore, forces are transferred from crystal to amorphous phase and vice versa by friction between them in perpendicular direction. To describe friction in the model, we introduced additional contact surfaces, see Figure 5.
The finite element method can reach larger length scales at smaller computational cost, as compared to all atom simulations. The computational cost of the finite element analysis of the cylindrical fibre model with 39 nm length, 14 nm diameter, about $2 \cdot 10^5$ finite elements, and applying a constant load of 1 nm displacement for 1 millisecond was about 3-4 CPU hours. The computational cost for a similar fibre model in an all atom simulation would require about 1 million CPU hours for a several million atom system and microsecond time scale. Moreover, setting up and modify a finite element model is less time consuming than an atomistic model for molecular dynamics simulations.

2.4 Refined 2-d Finite Element Fibre Model

In the next step of our spider silk modelling, we added one more component to account for the anisotropic cross-linking between the crystals. In the continuum mechanics-based approach, it is difficult to consider the influence of one crystal on other crystals, which are a distance away from each other.

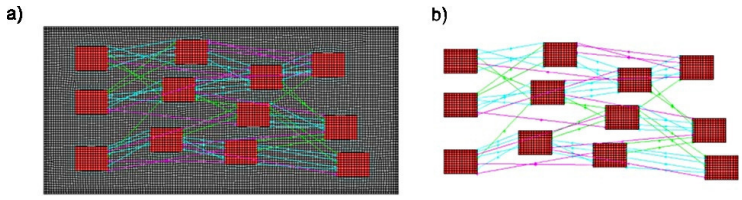

Fig. 6. 2-d finite element model: a) Crystals (red) are connected with truss elements in the amorphous phase component (grey), b) only truss elements with crystals. Shortest truss elements (cyan), medium length truss elements (lime green) and longest length truss elements (pink) connecting the randomly placed crystals.

Therefore, we introduced structural truss elements to mimic direct connections between neighbouring and distant crystals. For simplicity, we first built a 2-d finite element model, which is shown in Figure 6. The crystals are represented as rectangular faces and they are connected to the amorphous component as well as the truss elements along the horizontal direction. The crystals and the amorphous phase are not connected in vertical direction. Therefore, we applied sliding friction between them. Contact sliding friction in LS-DYNA is based on a Coulomb formulation. Friction is invoked by giving non-zero values for the static and dynamic friction coefficients, FS and FD, respectively, in the *CONTACT input. The percentage of amorphous chains, which are connected directly to the next crystal, side crystals in the next column and distant crystals, is still unclear in the literature. We have considered 65% of amorphous chains being connected directly to the next crystal, 25% being connected to side crystals in the next column, and 10% being connected to the distant crystals.

3 Model Calibration

Spider silk has different components and they exhibit different material properties. LS-DYNA offers a variety of material models, each with capabilities designed to capture the unique behaviour of the different components. A material model is described by a set of mathematical equations that gives a relationship between stress and strain. Material models are often expressed in a form in which infinitesimal increments of stress (or stress rate) are related to infinitesimal increments of strain (or strain rate). In this section, we calibrated the crystal component and the 3-d finite element fibre model by using standard material models of LS-DYNA.

The crystal component behaves like an elastoplastic material, which undergoes non-reversible changes of shape in response to applied forces. There are several mathematical descriptions of plasticity. We used the *MAT_003 material model from LS-DYNA, which is suited to model isotropic and kinematic hardening plasticity. For the finite element simulation, we used a crystal cube

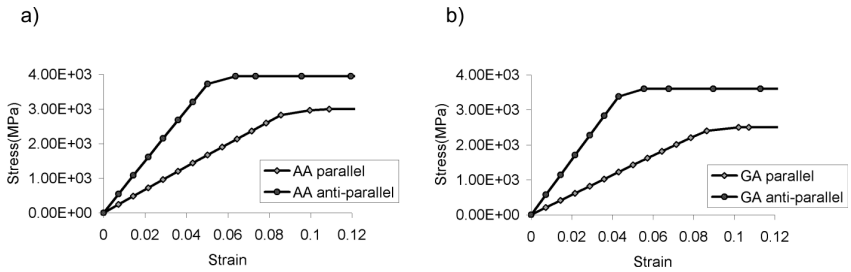

Fig. 7. Stress-strain curves for parallel and anti-parallel arrangement for a) AA (dragline silk) and b) GA (cocoon silk) using the plastic material with kinematic hardening model from LS-DYNA.

of size $2.048 \times 1.908 \times 2.691$ nm^3. The elastic modulus and the rupture strain were taken from all atom simulations. In our previous work [29], we discussed the MD simulations and finite element models proceeding from geometrical as well as material linearity of the crystal component[1]. In the present study, we took into account material nonlinearity and reproduced the previous MD simulation results [29] as shown in Figure 7.

From a literature study, we found some interesting properties of spider silk: cyclical loading characteristic shows that major ampullate silk is not completely reversible [27]. The hysteresis cycles indicate that a silk fibre does not weaken substantially upon repeated loading. When a silk fibre is stretched and held in place for some time, then, the required force decays exponentially. Therefore, silk fibres show relaxation behaviour [24]. Load cycle experiments by Denny (1976) indicate that major ampullate silk has a viscoelastic nature. The induced energy during a load cycle has been supposed to be transformed into heat through molecular friction [6].

As already mentioned, spider silk has two important components, crystals and the amorphous matrix. Previously, we studied the crystal component in detail [29]. It is an elastoplastic material. Therefore, the viscoelastic properties are assumed to be associated with the amorphous component. Before we go into the complicated user defined material subroutine, we studied inbuilt LS-DYNA viscoelastic material models. For study purposes, we assigned *MAT_006 material for the amorphous phase. This material model provides a general viscoelastic Maxwell model having up to 6 terms in the prony series expansion and is used for modelling of the amorphous phase. Figure 8 shows the loading rate effect on the silk fibre model. For this simulation study, we

[1] The β-sheet rich crystalline units consist of a poly-alanine, sequence, in spider dragline silk and cocoon silk, in an antiparallel or parallel arrangement of the strands. In an antiparallel arrangement, the successive β-sheet strands alternate directions so that the N-terminus of one strand is adjacent to the C-terminus of the next. In a parallel arrangement, all of the N-termini of successive β-sheet strands are oriented in the same direction.

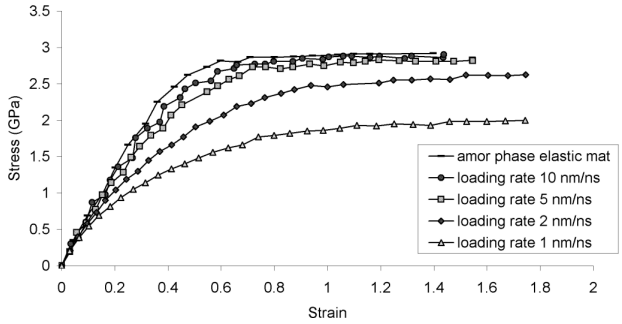

Fig. 8. Effect of loading rate on stress-strain curves of random arrangement fibre model. An elastoplastic material was assigned for the crystal component and a viscoelastic material for the amorphous phase.

have considered a random arrangement of the crystals over a length of 35 nm and 25% crystallinity. As the loading rate increases, the stiffness as well as the yield stress increases. Therefore, the fibre model is capable of describing loading rate-dependent behaviour.

We also studied the effect of the length of the fibre model on the stress-strain curves. For this simulation, we considered a random arrangement fibre model with an elastoplastic material model (*MAT_003) for the crystal component and a viscoelastic material model (*MAT_006) for the amorphous component. We applied 2 nm/ns constant velocity load to all fibre models. The results in Figure 9 show that if the length of the fibre model increases, the stiffness as well as the yield stress decreases due to the viscous effect in the fibre model. If an elastic material is assigned for the amorphous phase, the fibre mechanical response is independent of its length.

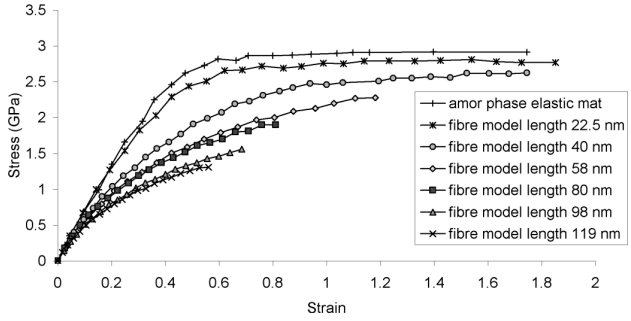

Fig. 9. Effect of the length on stress-strain curves for the random arrangement fibre model. Elastoplastic material assigned for the crystal component and viscoelastic material for the amorphous phase.

4 Summary and Future Work

Finite element analyses of the crystal block explained an elastoplastic material behaviour of the crystal component and reproduced the molecular dynamic simulations results. In the proposed 3-d finite element fibre model, elastoplastic crystals are randomly placed all in contact with the viscous amorphous phase. This fibre model is able to describe loading rate-dependency and length dependency behaviour. The second proposed model is a refined 2-d finite element fibre model, which is capable of predicting the anisotropic cross-linking between the crystals.
In our refined 2-d finite element model we have considered truss elements, which represent single connecting protein chains. The experimental measurements on a single protein chain using force spectroscopy revealed a force-extension behaviour in reasonable agreement with polymer random coil models such as the worm-like chain model (WLC) [15]. The force-extension behaviour of a single protein chain depends on its contour length [15], therefore we distinguish the truss elements into three categories according to their length. In LS-DYNA if the tensile test data is available, the stress-strain points can be entered for use with *MAT_024.
Another important point is interactions within the amorphous phase. These interactions exhibit different properties like stress/strain stiffening, kinematic hardening, fluidisation, bond breaking, etc. Future steps of our work will aim to create the user defined material subroutine to include all the properties mentioned above.

Acknowledgements. This study was supported by the Klaus Tschira Foundation and the German Research Foundation (DFG) under Grant GR 3494/7.

References

[1] A. Simmons, E. R. & Jelinski, L. W.: Solid-state 13C NMR of nephila clavipes dragline silk establishes structure and identity of crystalline regions. *Macromolecules* **27** (1994), 5235–5237.
[2] Altman, G. H.; Diaz, F.; Jakuba, C.; Calabro, T.; Horan, R. L.; J. Chen, H. L.; Richmond, J. & Kaplan, D. L.: Silk-based biomaterials. *Biomaterials* **24** (2003), 401–416.
[3] Beard, J.: Technology: Warding off bullets by a spider's thread. *New Scientist* **136** (1992), 18.
[4] Cetinkaya, M.; Xiao, S.; Markert, B. & Gräter, F.: Silk fiber mechanics from multiscale force distribution analysis. *Biophysical Journal* **100** (2011), 1298–1305.
[5] D. Porter, F. V. & Shao, Z.: Predicting the mechanical properties of spider silk as a model nanostructured polymer. *European Physical Journal E - Soft Matter* **16** (2005), 199–206.

[6] Denny, M.: The physical properties of spider's silk and their role in the design of orb-webs. *Journal of Experimental Biology* **65** (1976), 483–506.
[7] E. Oroudjev, J. S. & Hansma, H. G.: Segmented nanofibers of spider dragline silk: atomic force microscopy and single-molecule force spectroscopy. *Proceedings of the National Academy of Sciences USA* **99** (2002), 6460–6465.
[8] G. L. Jensen, W. L. & Seibert, C. E.: Spider identification and management. *Montana: Montana State University Extension Service* **3** (2005), E5 1–4.
[9] Grubb, D. T. & Jelinski, L. W.: Fiber morphology of spider silk: The effects of tensile deformation. *Macromolecules* **30** (1997), 2860–2867.
[10] Hinman, M. B. & Lewis, R. V.: Isolation of a clone encoding a second dragline silk fibroin. *Journal of Biological Chemistry* **267** (1992), 19320–19324.
[11] J. Gosline, C. O., P. Guerette & Savage, K.: Mechanical and molecular design of spider silks: a guide to the design of novel protein polymers. *Comparative Biochemistry and Physiology – Part B: Biochemistry and Molecular Biology* **126** (2000), 42–42.
[12] J. M. Gosline, M. E. D. & Denny, M. W.: The structure and properties of spider silk. *Endeavour* **10** (1986), 37–43.
[13] J. M. Gosline, P. A. G. & Savage, K. N.: The mechanical design of spider silks: from fibroin sequence to mechanical function. *Journal of Experimental Biology* **202** (1999), 3295–3303.
[14] Kaplan, D. L.: Fibrous proteins-silk as a model system. *Polymer Degradation and Stability* **59** (1998), 25–32.
[15] Marko, J. F. & Siggia, E. D.: Stretching DNA. *Macromolecules* **28** (1995), 8759–8770.
[16] Mori, H. & Tsukada, M.: New silk protein: modification of silk protein by gene engineering for production of biomaterials. *Reviews in Molecular Biotechnology* **74** (2000), 95–103.
[17] Osaki, S.: Is the mechanical strength of spider's drag-lines reasonable as lifeline? *International Journal of Biological Macromolecules* **24** (1999), 283–287.
[18] P. M. Cunniff, M. A. A., S. A. Fossey & Song, J. W.: Mechanical properties of major ampulate gland silk fibers extracted from nephila clavipes spiders. *ACS Symposium Series* **544** (1993), 234–251.
[19] Penman, D.: Spider silk delivers finest optical fibres. *New Scientist* **12** (2003), 20.
[20] S. Y. Hayashi, N. H. S. & Lewis, R. V.: Hypotheses that correlate the sequence, structure, and mechanical properties of spider silk proteins. *International Journal of Biological Macromolecules* **24** (1999), 271–275.
[21] Service, R. F.: Mammalian cells spin a spidery new yarn. *Science Magazine* **295** (2002), 419–421.
[22] Shao, Z. & Vollrath, F.: The effect of solvents on the contraction and mechanical properties of spider silk. *Polymer* **40** (1999), 1799–1806.

[23] T. Lefevre, M. E. R. & Pezolet, M.: Protein secondary structure and orientation in silk as revealed by raman spectromicroscopy. *Biophysical Journal* **8** (2007), 2885–2895.

[24] T. Vehoff, A. G.; Schollmeyer, H.; Zippelius, A. & Salditt, T.: Mechanical properties of spider dragline silk: Humidity, hysteresis, and relaxation. *Biophysical Journal* **93** (2007), 4425–4432.

[25] Termonia, Y.: Molecular modelling of spider silk elasticity. *Macromolecules* **27** (1994), 7378–7381.

[26] V. L. Brookes, R. J. Y. & Vollrath, F.: Deformation micromechanics of spider silk. *Journal of Materials Science* **43** (2008), 3728–3732.

[27] Vollrath, F. & Porter, D.: Spider silk as archetypal protein elastomer. *The Royal Society of Chemistry* **2** (2006), 377–385.

[28] Work, R. W.: Web components associated with the major ampullate silk fibers of orb-web-building spiders. *Transactions of the American Microscopical Society* **100** (1981), 1–20.

[29] Xiao, S.; Stacklies, W.; Cetinkaya, M.; Markert, B. & Gräter, F.: Mechanical response of silk crystalline units from force-distribution analysis. *Biophysical Journal* **96** (2009), 3997–4005.

[30] Xu, M. & Lewis, R. V.: Structure of a protein superfiber: Spider dragline silk. *Proceedings of the National Academy of Sciences* **87** (1990), 7120–7124.

[31] Z. Y. Dong, R. V. L. & Middaugh, C. R.: Molecular mechanism of spider silk elasticity. *Archives of Biochemistry and Biophysics* **284** (1991), 53–57.

Dynamics of Mechanically Induced Cytoskeleton Reorganisation: Experimental Study and Mechanical Modelling

M. Deibler[1], A. Avci[2], W. Ehlers[2], B. Markert[2] & R. Kemkemer[1,3]

[1] Max Planck Institute for Intelligent Systems, 70569 Stuttgart, Germany
[2] Institute of Applied Mechanics (CE), Chair of Continuum Mechanics, University of Stuttgart, Pfaffenwaldring 7, 70569 Stuttgart, Germany
[3] Reutlingen University of Applied Sciences, 72762 Reutlingen, Germany

Abstract. Mechanical forces are crucial in controlling the integrity and functionality of cells and sub-cellular structures. In particular, the actin stress-fibre network and associated adhesion sites are supposed to be load bearing structures as well as crucial elements in the process of mechanotransduction within a cell. In fact, these two structures show a dramatic reorganisation if an adherent cell is exposed to external forces. The underlying molecular and biophysical mechanisms of the dynamic reorganisation processes are poorly understood. In order to study the structural adaptation of the actin cytoskeleton at the impact of external uniaxial cyclic tensile strain, we monitor cells adherent on deformable substrates by life-cell fluorescent imaging. We demonstrate that focal adhesions and the actin cytoskeleton undergo dramatic reorganisation perpendicular to the direction of stretching forces. We speculate that the rotation-like movement is a continuous lateral tread-milling-like behaviour with a net mass displacement toward the less stressed-exposed side of the fibres. In a further step, we propose a phenomenological model for the description of the distinct reorientation of the actin fibres. To this end, non-linear evolution laws for the fibre orientations are formulated accounting for all experimentally observed dependencies such as strain amplitude and frequency. The theoretical model is implemented into the finite element framework and finally applied for simulating the adaptation of the actin structure of a single fibroblast under cyclic tension.

1 Introduction

Cells are natively surrounded and pervaded by a plethora of mechanical processes, acting on the cellular, sub-cellular and molecular level [22, 30, 33, 34]. On the cellular level, forces have an important impact on basic cellular functions, such as migration [20, 26], proliferation [33] and differentiation [13]. In the process of mechanotransduction, cells are able to translate forces or deformations in biochemical signals, which finally may lead to complex responses. The ability to detect and transform external mechanical stimuli is an intrinsic attribute of mechanosensitive cells, such as fibroblasts, osteocytes or endothelial cells [12, 39]. The cells are able to adapt their morphology and

structural components once they are exposed to external mechanical stimuli. Maintenance of the cellular shape is thereby a complicated net product of membrane forces, osmotic pressure, shear stresses, tensional and compressive forces, sophisticatedly balanced by a multitude of complex, rate-dependent mechanisms [25].

Important elements for the structural integrity of cells are semi-dilute meshworks of semi-flexible biopolymers termed cytoskeleton [3, 24]. The cytoskeleton is essential in establishing a specific cell morphology and transmitting and converting extracellular forces to cellular responses [6, 37]. It consists of microfilaments, microtubules, and a group of polymers collectively described as intermediate filaments. Microfilaments are cable-like dynamic structures assembled from actin monomers forming actin filaments, which can also assemble with additional proteins to contractile actin stress fibres, one major intracellular tension bearing structure [10, 23].

A common approach to investigate mechanically induced cell responses in vitro is the use of flexible membranes as cell culture substrates. Cells adhere on such membranes and cyclic tensile deformation of the membrane can be realised by a simple apparatus [2]. In such experiments, it is a well-observed phenomena that cells respond to a uniaxial cyclic tensile strain (CTS) by reorganising, over several hours, their cell morphology with respect to the major axis of strain [4, 5, 8, 17, 19]. R. Buck was one of the first investigators interested in the effects of uniaxial cyclic substrate deformation on cell populations [5]. Using a rudimentary device to deform cells adhering to a polysiloxane polymer substrate, he subjected fibroblast to 0.07 Hz cyclic stretch with unknown amplitude. He found that cells align orthogonally to the direction of stretch within 18-24 hours. This general behaviour could be found for various cell types [4, 8, 18, 19]. This response is suggested to be an avoidance reaction protecting the cells from longitudinal deformation and force overload [5]. Further reports exhibited that this cell reorientation depends on the strain amplitude [7, 19]. Increasing amplitudes led to faster cell body orientation, requiring a minimal deformation of more than 2%.

Jungbauer et al. substantiated these observations by means of live cell experiments on periodically deformed substrates utilizing rat embryonic fibroblasts (REF52wt) and human dermal fibroblasts [19]. Beyond a characteristic threshold stretch amplitude (REF52wt: 1%, HDF: 2%) both cell types reoriented faster with increasing deformation amplitude, following a linear dependency of reorganisation time on amplitude. Sub-confluent fibroblasts responded to increasing frequencies (1.0×10^{-4} Hz to 20.0 Hz) with a biphasic characteristic. The orientation speed and maximal alignment increases with frequency until reaching a threshold frequency at 1.0 Hz. Beyond this stimulation frequency, both orientation parameters remained constant [19]. Since the cytoskeleton is the major integrity providing structure within the cell and essential for migration processes, it appears obvious that it might adopt a central position in force-induced avoidance responses. Especially the dynamic

microfilament system got increasingly into the focus of biomechanically motivated studies [15, 17, 31, 38]. Actin stress fibres (SF) were found to be reorganised perpendicular to the direction of deformation within the experimental time frame, coinciding with cell soma reorientation [11, 15, 17, 31, 36, 38]. Currently, the avoidance response is assumed to protect cells from longitudinal deformation, thereby minimizing the intracellular strain and disruption of vital cellular structures, as for example the cytoskeleton [5, 9, 19, 38]. Despite numerous experimental studies investigating actin dynamics during biomechanical stimulation, a holistic picture how stress fibres are realigned is still missing. Studies conducted so far are contradictory in terms of experimental outcomes and observations. In order to determine the dynamics of the actin stress fibre reorganisation, we performed experiments by using actin fluorescent probes and a self-build setup to expose the cells to cyclic tensile strain (CTS). This approach allowed for observing the structural adaptation of actin stress fibres over a time of several hours with a sufficient temporal resolution.

In order to obtain a better understanding of the mechanically triggered internal cell reorganisation, a phenomenological continuum model based on a linear elastic stress analysis of a cell adhering to a flexible substrate is developed. The changes in the actin fibre orientation are predicted based on the present minimum principal strain direction, where the evolution of the fibre angle accounts for the relevant dependencies on the peak strain amplitude, loading frequency and time history observed in the experiments. The governing differential equations and constitutive relations are implemented into a two-dimensional finite element framework, which enables us to simulate the uniaxial cyclic strain response of a fibroblast cell, but also paves the way for the computation of more complex biaxial loading scenarios in the future.

2 Dynamic Actin Reorganisation upon Application of Cyclic Tensile Strain

The setup for mechanically stimulating cells while observing their responses by live-cell microscopy was developed previously by Jungbauer *et al.* [19]. The membrane is fixed in a device and stretched periodically as schematically shown in Figure 1A. Typically, cells adhere on the membrane with no preferred direction of their long cell axis. The orientation gradually changes once cyclic tensile strain is applied, adopting a highly ordered alignment perpendicular to the direction of deformation (Figure 1B, Figure 2A). Image analysis is used to determine the orientation of the cell body ($\varphi_{Cell\ body}$) and the mean actin orientation angle (φ_{Actin}) for predefined time points (Figure 1C).

We subjected Rat Embryonic Fibroblasts (REF52wt) transfected with EGFP-Lifeact to periodic uniaxial tensile strain at various stimulation frequencies at a constant amplitude of 8% and observed the behaviour of the cells by

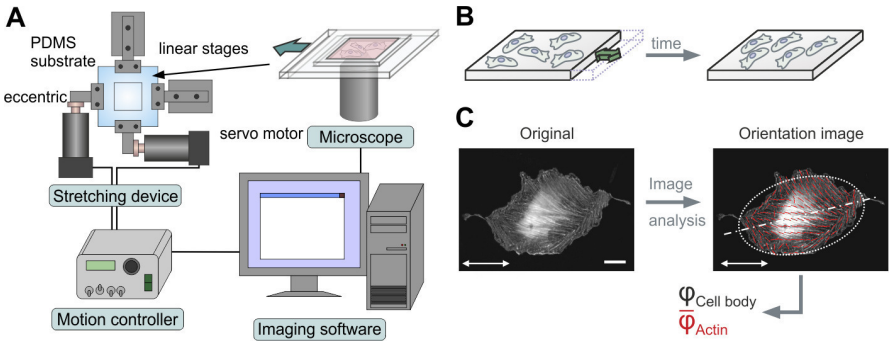

Fig. 1. Automated mechanostimulation of adherent cells. **A)** Experimental setup: an elastic substrate is periodically deformed with help of computer-controlled servo motors. Microscopy and mechanical stimulation are synchronised via a self-developed software routine. **B)** Adherent cells, cultured on elastic PDMS substrates, change their mean orientation from random to perpendicular during application of cyclic tensile strain with respect to the major axis of deformation. **C)** Determination of cell body and actin orientation by image analysis (scale bar: 25 µm, double arrow indicates direction of deformation).

live-cell microscopy. The cells showed the characteristic reorientation of the cell body upon the application of the CTS (Figure 2A). The initial orientation is set by the deliberate selection of a field of view exhibiting cells with initially random orientation with respect to direction of deformation. During the experiments cells realigned orthogonally to the direction of cyclic tensile deformation (see [11, 19]).

In accordance with the reorganisation of the cell bodies, the actin stress fibre system within the cells gradually realigns from a initially nearly parallel orientation with respect to the direction of CTS, to a virtually perpendicular orientation by continuously shifting pre-existing fibres (Figure 2B). Transfection of REF52wt cells with pEGFP-Lifeact, a bacterial plasmid encoding a fluorescent protein indirectly labelling f-actin, allowed the experimental visualisation of this process. Remarkably, only a few stress fibres were disrupted during mechanical stimulation. Most of these contractile filaments appeared to remain macroscopically intact. The fibres seemed to rotate gradually toward the new direction over time. Stress fibre orientation was quantified by local image processing routines measuring the mean orientation in small squares within the cells. Average orientation of the actin stress fibres within the cell was then calculated form these local orientation angles.

To determine whether the deformation-induced fibre reorientation was dependent on the applied stretching rate (deformation speed), CTS was applied at increasing frequencies. The mean actin stress fibre orientation was determined over time for each experimental condition. The initial mean stress fibre orientation angle $\bar{\varphi}_0 = 22.4° \pm 3.5°$ (SEM, $N > 8$) was due to deliberate selection of transfected cells, approximately oriented within the direction

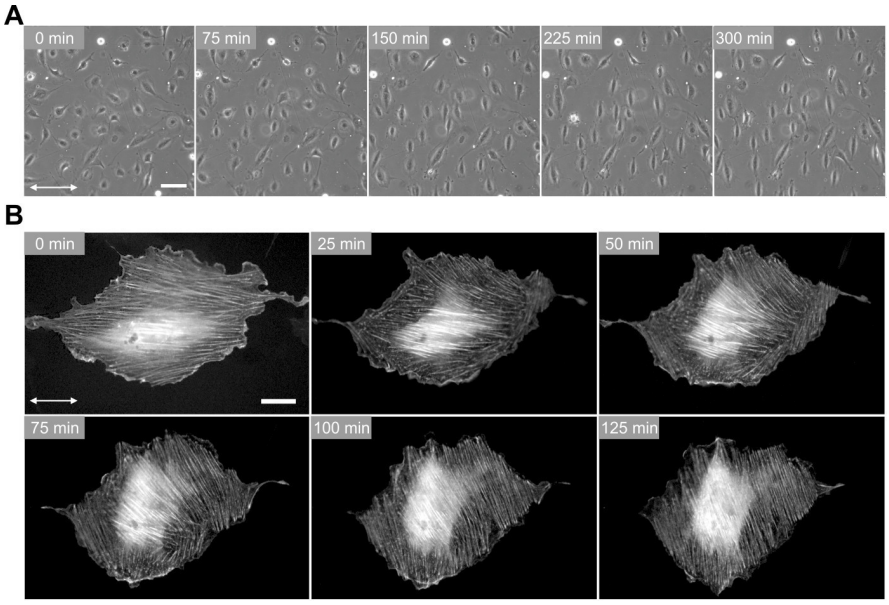

Fig. 2. Reorientation of the cell body and actin stress fibres of Rat Embryonic Fibroblasts (REF52wt) during cyclic tensile deformation. **A)** Cell body alignment from random to perpendicular with respect to the direction of tensile strain during application of 8% stretch at 0.5 Hz (scale bar: 100 µm). **B)** Reorganisation of actin stress fibres in EGFP-Lifeact expressing REF52wt cells orthogonally to the direction of CTS. Actin stress fibres are continuously realigned during mechanical stimulation (0.5 Hz, 8%, scale bar: 25 µm, double arrow indicates direction of deformation).

of deformation. Non-stimulated cells maintained their initial actin alignment over time (Figure 3A, black squares). A continuous non-linear increase in the mean orientation angle $\bar{\varphi}$ could be observed for all experimental conditions (Figure 3A). Stimulation with 0.1 Hz led to a gradual shift of $\bar{\varphi}$, levelling off after 250 min cyclic deformation within the regime of indifferent orientation (approx. 45°) (Figure 3A, purple circles). Increasing deformation rates induced a faster change in the actin stress fibre alignment, determined by a reduced half-maximal orientation time ($t_{\frac{1}{2}}$), Figure 3B). Stimulation at 0.5 Hz led to a clearly distinguishable plateau phase after approximately 125 min of mechanical stimulation at a mean orientation angle of $\bar{\varphi}$= 62.6° ± 0.6° (SEM, N > 8, Figure 3A, blue triangles), approaching a new steady state of the actin orientation in a more perpendicular direction to the uniaxial strain. Displaying no initial lag-time, the time course could be fit with a simple exponential function. The approximated half-maximal orientation time was determined to be 59.6 min ± 2.5 min with a maximal orientation

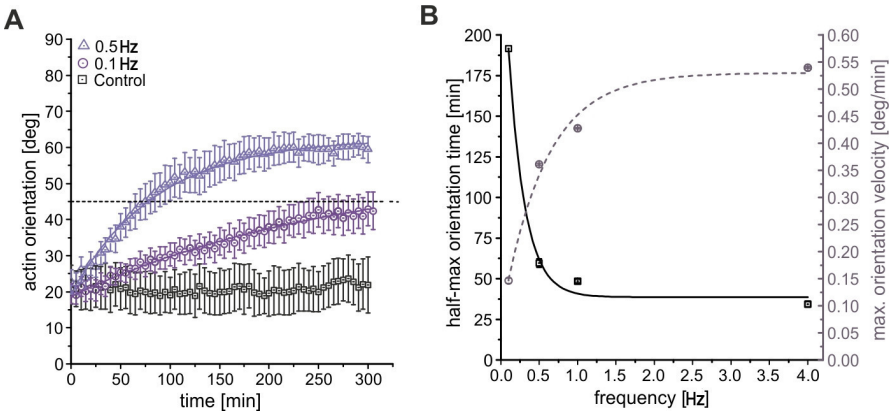

Fig. 3. Reorientation characteristics of stress fibres in EGFP-Lifeact transfected REF52wt cells subjected to 8% CTS. **A)** Mean actin stress fibre reorientation over time for three selected frequencies at a fixed amplitude of 8%. **B)** Half-maximal orientation time and maximal orientation velocity at deformation rates between 0.1 and 4.0 Hz.

speed (v_{max}) of 0.36°/min. Both parameters ($t_{\frac{1}{2}}$) and v_{max} could be shown to scale non-linearly with the deformation rate (Figure 3B).
Closer examination of this stress avoidance response exhibited two major underlying mechanisms: a phenomenological rotation of apparently intact stress fibres away from the major axis of tensile strain and fusion of fibres parallel to the direction of stretch with subsequent alignment along rotating actin filaments.

3 Modelling of Actin Stress Fibre Realignment

We proceed from an isotropic, linear elastic stress analysis, where the stress state in the flexible PDMS substrate is computed from a Hookean elasticity law with the stress tensor given as

$$\boldsymbol{\sigma} = \frac{E}{(1+\nu)}\,\boldsymbol{\varepsilon} + \frac{E\,\nu}{(1+\nu)\,(1-2\,\nu)}\,(\boldsymbol{\varepsilon}\cdot\mathbf{I})\,\mathbf{I}\,. \tag{1}$$

Herein, $E = 1.2$ MPa and $\nu = 0.49$ are the Young's modulus and Poisson's ratio of the substrate, $\boldsymbol{\varepsilon} = \mathrm{sym}(\mathrm{grad}\,\mathbf{u})$ is the linear strain tensor of the infinitesimal theory with displacement vector $\mathbf{u}$, and $\mathbf{I}$ is the identity tensor. Due to the thinness of the substrate membrane (approx. 400 µm), (1) is evaluated for plane-stress conditions with the out-of-plane stress components being neglected. Moreover, the stress and deformation fields in the substrate are assumed not to be affected by the adhering cells, which are modelled as perfectly attached to the substrate. Relative movements of the cells and their adhesion sites with respect to the PDMS membrane are not considered.

The in-plane (1-2 plane) substrate displacements u_1 and u_2, and thus, the deformations imposed on the cells, are computed from the momentum balance

$$\operatorname{div}\boldsymbol{\sigma} = \mathbf{0} \quad \overset{\text{plane}}{\underset{\text{stress}}{\longrightarrow}} \quad \begin{cases} \mathbf{e}_1 : & \dfrac{\partial \sigma_{11}}{\partial x_1} + \dfrac{\partial \sigma_{12}}{\partial x_2} = 0\,, \\ \mathbf{e}_2 : & \dfrac{\partial \sigma_{21}}{\partial x_1} + \dfrac{\partial \sigma_{22}}{\partial x_2} = 0\,. \end{cases} \tag{2}$$

Herein, inertia and body forces have been neglected, $\mathbf{e}_1$ and $\mathbf{e}_2$ denote the Cartesian in-plane basis vectors, x_1 and x_2 the respective coordinates, and σ_{ik} $(i,k = 1,2)$ the coefficients of the stress tensor components.
Proceeding from an initial distribution of the actin orientation $\varphi_0(\mathbf{x}, t_0)$ in a cell ($\mathbf{x} \in \Omega_{Cell}$ is the vector pointing to a position in the cell domain Ω_{Cell}) at time $t = t_0$ obtained from the experiments by image analysis (cf. Figure 1), the reference fibre vectors read $\mathbf{a}_0 = \cos(\varphi_0)\,\mathbf{e}_1 + \sin(\varphi_0)\,\mathbf{e}_2$. The actual actin fibre vectors in the deformed configuration can then be computed from the mapping $\mathbf{a} = \mathbf{F}\,\mathbf{a}_0$ with the material deformation gradient $\mathbf{F} = \operatorname{grad}\mathbf{u} + \mathbf{I}$. However, the temporal evolution of the fibre angle in the course of the mechanical stimulation is described with respect to the unstrained state, which has also been used for the image acquisition during the CTS experiments.
The reorientation of the actin stress fibres is modelled based on the experimental observation that a cell tries to escape from the loading direction by rearranging its structural stiffness perpendicular to the exposed stretching. In mechanical terms, this means that the actin fibres realign in the minimum principal strain direction, which can be easily computed from the strain tensor components. In particular, the principal direction φ_p^{min} is found from

$$\tan(2\,\varphi_p^{max}) = \frac{2\,\varepsilon_{12}}{\varepsilon_{11} - \varepsilon_{22}} \quad \longrightarrow \quad \varphi_p^{min} = \varphi_p^{max} + \tfrac{1}{2}\,\pi\,. \tag{3}$$

Proceeding from a tightly interconnected fibre network, even local stretching of a part of the cell is assumed to activate the reorientation mechanism in the entire cell. This hypothesis is corroborated by experiments locally stimulating cells via atomic force microscopy or anisotropic stretching thereby inducing a general stiffening of the cell body [21, 28, 35] or observing a stress fiber response far away from the stimulation site [16]. Rigidity is governed by the cytoskeleton thereby establishing a direct causality between the stiffening response, the intracellular fibre network and the reorientation mechanism. To describe the possibly biaxial state of strain that is sensed by a cell, we use the common definition of the equivalent strain

$$\varepsilon_{eq} := \frac{1}{E}\,\sigma_{eq} \quad \text{with} \quad \sigma_{eq} = \sqrt{\sigma_{11}^2 + \sigma_{22}^2 - \sigma_{11}\,\sigma_{22} + 3\,\sigma_{12}^2} \tag{4}$$

as the equivalent (von Mises) stress in the PDMS substrate under plane-stress conditions. For the uniaxial CTS experiment, (4) simplifies to $\varepsilon_{eq} =$

$\frac{1}{E}\,|\sigma_{11}| = |\varepsilon_{11}|$ with $\mathbf{e}_1$ being the stretching direction. In the same way as the value of the equivalent strain is related to the externally applied peak strain amplitude, its temporal change $\dot{\varepsilon}_{eq} = \mathrm{d}\varepsilon_{eq}/\mathrm{d}t$ (equivalent strain rate) is connected to the loading frequency[1].

Experimental observations exhibit a cell-type specific lower threshold frequency (0.01 Hz - 0.05 Hz) upon reorientation of cells and stress fibres occurs [19]. Therefore, we assume that the persistence of the strain signal in the cell is not very long. In other words, the signal dissipates over time. The cell's fading memory of the mechanical stimulus is modelled by use of decaying exponential functions of the maximum values of ε_{eq} and $\dot{\varepsilon}_{eq}$. In particular, we define the sensed peak strain amplitude and loading frequency as

$$A_{Cell} = A_{Cell}^{max} \exp\big(-\frac{t-t_A}{\tau_A}\big) \quad \text{with} \quad A_{Cell}^{max} = \max_{t\in[0,T]}\Big(\max_{\mathbf{x}\in\Omega_c}\big(\varepsilon_{eq}(\mathbf{x},t)\big)\Big), \tag{5}$$

$$f_{Cell} = f_{Cell}^{max} \exp\big(-\frac{t-t_f}{\tau_f}\big) \quad \text{with} \quad f_{Cell}^{max} = \max_{t\in[0,T]}\Big(\frac{\max\limits_{\mathbf{x}\in\Omega_c}\big(\dot{\varepsilon}_{eq}(\mathbf{x},t)\big)}{\pi \max\limits_{\mathbf{x}\in\Omega_c}\big(\varepsilon_{eq}(\mathbf{x},t)\big)}\Big). \tag{6}$$

Therein, t_A and t_f denote the times in the considered time interval $[0,T]$ at which the maximum values A_{Cell}^{max} and f_{Cell}^{max} occur, and τ_A and τ_f are the relaxation time constants governing the fading memory effect. Based on the above mentioned experimental observations, investigating embryonic rat fibroblast cells, we assume $\tau_A = \tau_f = 5$ min.

Moreover, dependent on the cell type, the actin fibre bundles remain in the reoriented state or relax back to their initial orientation if the loading has stopped or is below some amplitude or frequency threshold A_{Cell}^{thr} or f_{Cell}^{thr}. The considered fibroblasts show a reverse orientation dynamics under strain-relieved conditions with the back-rotation to the initial fibre direction φ_0 taking place within the same time frame as the mechanically triggered realignment [19]. This is accomplished in the model by setting

$$\varphi_p^{min} = \varphi_0 \quad \text{if} \quad A_{Cell} < A_{Cell}^{thr} \quad \text{or} \quad f_{Cell} < f_{Cell}^{thr}\,, \tag{7}$$

where for the REF52wt cells $A_{Cell}^{thr} = 1$ % and $f_{Cell}^{thr} = 0.01$ Hz [19]. The final evolution of the stress fibre orientation proceeds from two experimentally inspired assumptions. First, the linear dependence of the fibre orientation velocity (angular velocity) on the peak strain amplitude is adopted from observations on whole cells, where the cell reorientation dynamics is assumed to be also representative for the internal stress fibres. Second, the exponential

[1] Consider a sinusoidal, uniaxial strain loading $\varepsilon_{11} = A_{load}\,[\frac{1}{2}\,\sin(2\,\pi\,f_{load}\,t - \frac{1}{2}\,\pi) + \frac{1}{2}\,]$. Then, the maximum value of the equivalent strain corresponds to the applied peak strain amplitude, $\max(\varepsilon_{eq}) = A_{load}$, and the magnitude of the equivalent strain rate is proportional to the loading frequency, $\max(\dot{\varepsilon}_{eq}) = \pi\,f_{load}\,A_{load}$. In the context of bone tissue adaptation, a more detailed discussion on strain-amplitude-frequency relations can be found in Turner [29].

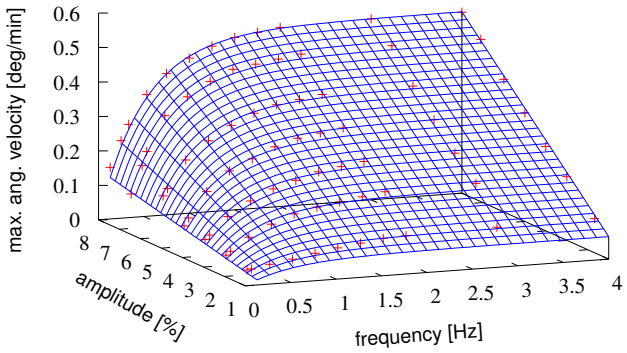

Fig. 4. Sketch of the modelled fibre orientation velocity (angular velocity) function (8) depending on the peak strain amplitude and the loading frequency in the CTS experiment. For the plot $(\varphi_p^{min} - \varphi_{Actin})/\tau_\varphi = 1$ has been used.

dependence of the maximal orientation velocity on the loading frequency (see Figure 3B) is supposed to hold also for the entire alignment process. Following this, the fibre angle is determined from the empirical rate equation

$$\dot{\varphi}_{Actin} = c_A\, A_{Cell} \left(1 - \exp(-c_f\, f_{Cell})\right) \frac{1}{\tau_\varphi} \left(\varphi_p^{min} - \varphi_{Actin}\right) \tag{8}$$

with the parameters $c_A = 6.6$ and $c_f = 2.0$ and the time constant $\tau_\varphi = 45$ min controlling the speed of the fibre angle evolution. A plot of the function is provided in Figure 4.

4 Materials and Methods

Cell Culture REF52wt rat embryonic fibroblasts were cultured at 37°C, 5% CO_2 in Dulbecco's modified eagle medium (DMEM, 4.5 g/L D-glucose) (Invitrogen, Karlsruhe, Germany) supplemented with 10% fetal bovine serum (FBS; Invitrogen). Cells were used before passage 30.

Plasmids and Transfection Transfection was performed using pEGFP-Lifeact [27] (kind gift of Michael Sixt, Institute of Science and Technology, Klosterneuburg, Austria) with the Nucleofector Kit R (Lonza, Basel, Switzerland) and the AMAXA Nucleofector system (Lonza). Following transfection, cells were plated on transparent, elastic poly(dimethylsiloxane) (PDMS, Sylgard 184, Dow Corning, Midland, USA) membranes coated with 5 µg/ml bovine fibronectin (Sigma, Steinheim, Germany) and cultured for 16 h at standard conditions (37 °C, 5% CO_2) before experimental use.

Mechanical Stimulation Cells cultured on PDMS membranes were exposed to uniaxial cyclic tensile strain (CTS) as described previously [11, 19].

Briefly, a customised stretching device was fit on an upright fixed-stage microscope (AxioExaminer, Carl Zeiss). PDMS membranes with cells are clamped to this device and cells can be observed with the microscope. The entire setup (microscope and stretching device) was enclosed by an environmental chamber to perform the experiments at culture conditions 37 °C. Uniaxial cyclic stretch experiments were performed with cells covered by phenol red free Leibovitz L-15 media (Invitrogen) supplemented with 5% FBS and 1% penicillin-streptomycin (Invitrogen). The stretching amplitude was kept constant at 8% stretch, stretching frequency was varied from 0.1 Hz to 4.0 Hz. Imaging was carried out using either an A-Plan 5x/0,12 Ph0 objective or a W-Plan-Apochromat 40x/1,0 DIC objective (both Carl Zeiss) in combination with a Halogen lamp or the Colibri (Carl Zeiss) LED illumination system. Additional magnification was achieved via a manual magnification changer adjacent to the CCD-camera (AxioCam MRm3, Carl Zeiss). Cells with comparable fluorescence intensity were chosen for each experiment. A self-developed software routine was used to synchronise image acquisition with the stretching control. Cyclic stretching was stopped every five minutes (or other time intervals if indicated), cells were automatically focused and z-stacks of images were taken in the relaxed state of the substrate.

Image Processing Z-stacks were projected via an extended depth of field routine developed for ImageJ [1] by the Biomedical Imaging Group, EPFL, Lausanne [14] and contrast enhanced, setting 0.5% of the overall pixels to saturation. After background removal by means of thresholding and masking, actin orientation was extracted by 32×32 pixel sliding square analysis of the images. Fast Fourier Transformation (FFT) was performed in each square following shape analysis of the FFT image by fitting an ellipse to the Fourier spectra and calculating the angle of the major axis. Rotation by 90° yielded the mean orientation of the actin bundles within the field of analysis. The mean angle of actin orientation and the mean standard error was calculated using Matlab (MathWorks, Natick, USA). The mean inter-stress-fibre distance was quantified by means of line plots across multiple sections within one cell, averaging the results over six independent experiments.

FE Simulation All computations have been performed using the finite element solution environment FlexPDE V 6.20 (PDE Solutions Inc., 9408 E. Holman Rd., Spokane Valley, WA 99206, USA). The implementation proceeds from a 2-d Cartesian framework (`COORDINATES CARTESIAN2`) with the x-y coordinates representing the 1-2 plane of the thin PDMS membrane assuming plane-stress conditions. The degrees of freedom (DOF) of the analysis are the in-plane substrate displacements u_1 and u_2, which also correspond to the cell displacements, and the actin fibre orientation angle φ_{Actin}.
The model described in Section 3 is implemented into FlexPDE using the strong form of the momentum balance (2) to determine the unknown dis-

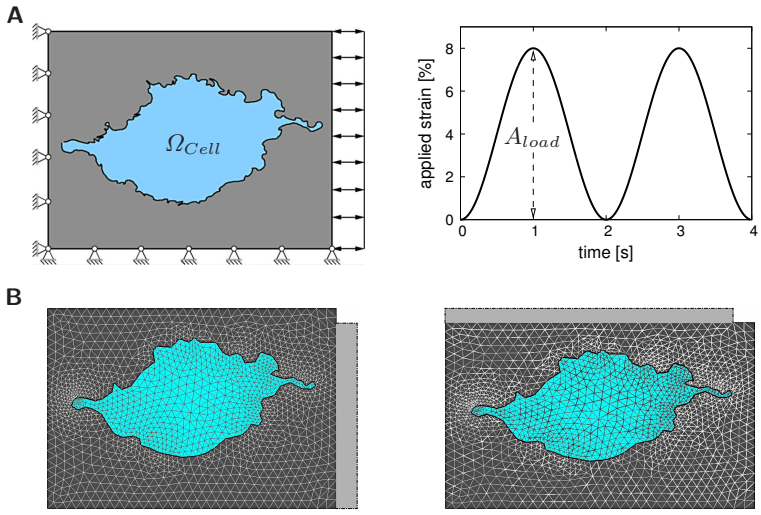

Fig. 5. A) Geometry and boundary conditions of the displacement-driven, cyclic tensile test with exemplary loading path for a peak strain amplitude of 8% at a frequency of 0.5 Hz according to (9). **B)** Undeformed and deformed finite element mesh during the cyclic tension test.

placements and the evolution equation for the fibre angle (8) (`EQUATIONS` section). The strain and stress computation as well as the constitutive functions describing the reorientation properties and the fading memory effect are implemented in the `DEFINITIONS` section using the built-in features of FlexPDE.

An initial-boundary-value problem describing the CTS experiment of a single cell is defined using a rectangular domain ($W \times H = 220 \times 165\,\mu m^2$) representing a small section of the cell-populated PDMS membrane (approx. $20 \times 20\,mm^2$). On it we imprinted a second domain Ω_{Cell} with the real shape of a representative fibroblast cell reconstructed from an experimentally acquired image (see Figure 5A, left). Initially, the displacements are set to zero in the entire domain and the fibre angle in the cell is initialised with the values obtained from the image analysis. The entire domain is spatially discretised with triangular finite elements using quadratic interpolation functions for all unknowns (778 elements, 1615 nodes, 4845 DOF). For the time integration, FlexPDE uses by default a second-order backward difference formula with adaptive time-step control. For the CTS simulation, we have chosen constant time increments (`FIXDT=ON`) of one-tenth of the minimum period of the applied load, i. e., $\Delta t = (10\, f_{load})^{-1}$ to ensure a good signal reconstruction. The rectangular domain is fixed horizontally at the left and vertically at the bottom, while the top side is not constrained and the right side is loaded

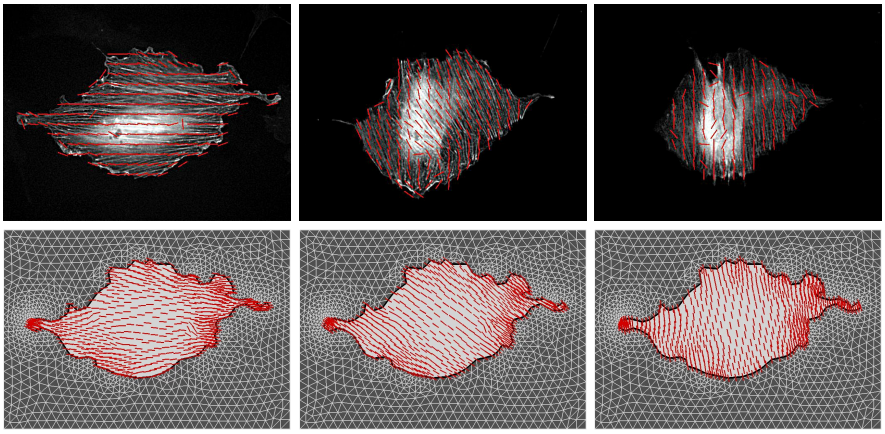

Fig. 6. Comparison between experiment and simulation at different reorientation stages for a cell subjected to 8% CTS at 0.5 Hz. The simulated fibre directions are depicted with respect to the undeformed cell as the current modelling approach does not account for active cell reorientation and deformation.

displacement-driven in horizontal direction via

$$\overline{u}_1(t) = A_{load}\, W \left[\tfrac{1}{2} \sin\left(2\,\pi\, f_{load}\, t - \tfrac{1}{2}\,\pi\right) + \tfrac{1}{2} \right]. \tag{9}$$

The geometry and boundary conditions, the loading path and the undeformed and deformed FE mesh are depicted in Figure 5.
The computation results are written to a data file and analysed using the visualisation software tool Tecplot 360 2010 (Tecplot, Inc., 3535 Factoria Blvd. S. E., Bellevue, WA 98015, USA). A comparison of the actin fibre orientation obtained from the experiment and predicted by the simulation is given in Figure 6. As can be seen, the phenomenological model is capable of mimicking the reorientation behaviour very nicely. However, it must be noted that the reorientation and change in shape of the whole cell is not described by the current modelling approach as no relative movement between cell and substrate is considered.

5 Conclusion and Discussion

Cells have remarkable abilities to sense and respond to mechanical signals of their environment, but despite the physiological importance, the underlying biological and mechanical mechanisms are poorly understood. We could experimentally demonstrate that the well-studied phenomenon of cell alignment at the application of cyclic uniaxial tensile strain coincides with a rotation-like reorganisation of the actin stress fibres in a perpendicular direction to the strain axis. The kinetics of that process depends on the frequency of the cyclic

strain. Remarkably, there is hardly a disruption and complete dissociation of stress fibres in response to the strain visible. The stress fibres rather change their orientation continuously within a time course of several minutes regardless of the frequency of the cyclic tensile strain. This observation is partly in contrast to a mechanism proposed by Wang [32]. There, stress fibres are suggested to have a basal intrinsic strain energy and deviation from it may cause filament disassembly. Another phenomenological model suggests that cells try to keep an optimal stress level in the stress fibres, and therefore, the actin fibres reorganise in perpendicular direction upon the application of uniaxial cyclic tensile strain [9]. However, the mechanism of the actual reorganisation of the stress fibres is not addressed.

In our study, we proceed from a phenomenological description based on mean-field physics thereby taking into account the relevant factors influencing the actin reorientation process. In particular, we model the fibre angle as a field function that evolves with a rate equation governed by the minimum principle strain direction, the peak strain amplitude and the loading frequency. Moreover, time history effects as well as min/max thresholds are also accounted for. Consequently, the macroscopic modelling approach enables us to mimic the stress fibre reorganisation with sufficient spatial and temporal resolution. However, a limitation of our as well as the other above-mentioned models is that no molecular details of sub-cellular structures are considered.

Our and other experiments show that stress fibres and focal adhesions, which link the extracellular environment to the stress fibres, are key players in the mechanically induced reorganisation and need to be considered in a more realistic model. The current description proceeds from a welded contact between cell and substrate such that active cell movement and deformation are excluded. The discrete modelling of adhesion sites would alleviate this limitation. It should finally be noted that with the presented continuum model and its numerical treatment using the finite element method, it is straightforward to extend the simulations to whole cell clusters or cells embedded into an extracellular matrix and to more complex loading scenarios. This opens an avenue for future investigations.

Acknowledgements. This study was supported by the Federal Ministry of Education and Research (BMBF) of Germany under the call "Systems Biology for Tissue Engineering of Mesenchymal Stem Cells: Integrating Novel Experimental Methods and Mathematical Models" (Grant: 0315506A, AZ: 0101-31 P 5848).

References

[1] Abramoff, M. D.; Magalhaes, P. J. & Ram, S. J.: Image Processing with ImageJ. *Biophotonics International* **11** (2004), 36–42.

[2] Bao, G. & Suresh, S.: Cell and molecular mechanics of biological materials. *Nature Materials* **2** (2003), 715–725.
[3] Bausch, A. R. & Kroy, K.: A bottom-up approach to cell mechanics. *Nature Physics* **2** (2006), 231–238.
[4] Boccafoschi, F.; Bosetti, M.; Gatti, S. & Cannas, M.: Dynamic fibroblast cultures: response to mechanical stretching. *Cell Adhesion & Migration* **1** (2007), 124–128.
[5] Buck, R. C.: Reorientation response of cells to repeated stretch and recoil of the substratum. *Experimental Cell Research* **127** (1980), 470–474.
[6] Cai, Y. & Sheetz, M. P.: Force propagation across cells: mechanical coherence of dynamic cytoskeletons. *Current Opinion in Cell Biology* **21** (2009), 47–50.
[7] Dartsch, P. & Hämmerle, H.: Orientation of cultured arterial smooth muscle cells growing on cyclically stretched substrates. *Cells Tissues Organs* **125** (1986), 108–113.
[8] Dartsch, P. C. & Betz, E.: Response of cultured endothelial cells to mechanical stimulation. *Basic Research in Cardiology* **84** (1989), 268–281.
[9] De, R.; Zemel, A. & Safran, S.: Dynamics of cell orientation. *Nature Physics* **3** (2007), 655–659.
[10] Deguchi, S.; Ohashi, T. & Sato, M.: Intracellular stress transmission through actin stress fiber network in adherent vascular cells. *Molecular & Cellular Biomechanics: MCB* **2** (2005), 205–216.
[11] Deibler, M.; Spatz, J. P. & Kemkemer, R.: Actin fusion proteins alter the dynamics of mechanically induced cytoskeleton rearrangement. *PLoS ONE* **6** (2011), e22941.
[12] Discher, D. E.; Janmey, P. & Wang, Y.-L.: Tissue cells feel and respond to the stiffness of their substrate. *Science* **310** (2005), 1139–1143.
[13] Discher, D. E.; Mooney, D. J. & Zandstra, P. W.: Growth factors, matrices, and forces combine and control stem cells. *Science* **324** (2009), 1673–1677.
[14] Forster, B.; Van De Ville, D.; Berent, J.; Sage, D. & Unser, M.: Complex wavelets for extended depth-of-field: a new method for the fusion of multichannel microscopy images. *Microscopy Research and Technique* **65** (2004), 33–42.
[15] Geiger, R. C.; Taylor, W.; Glucksberg, M. R. & Dean, D. a.: Cyclic stretch-induced reorganization of the cytoskeleton and its role in enhanced gene transfer. *Gene Therapy* **13** (2006), 725–731.
[16] Guolla, L.; Bertrand, M.; Haase, K. & Pelling, A. E.: Force transduction and strain dynamics in actin stress fibres in response to nanonewton forces. *Journal of Cell Science* **125** (2012), 603–613.
[17] Hayakawa, K.; Hosokawa, a.; Yabusaki, K. & Obinata, T.: Orientation of Smooth Muscle-Derived A10 Cells in Culture by Cyclic Stretching: Relationship between Stress Fiber Rearrangement and Cell Reorientation. *Zoological science* **17** (2000), 617–624.

[18] Hayakawa, K.; Sato, N. & Obinata, T.: Dynamic reorientation of cultured cells and stress fibers under mechanical stress from periodic stretching. *Experimental cell research* **268** (2001), 104–114.

[19] Jungbauer, S.; Gao, H.; Spatz, J. P. & Kemkemer, R.: Two characteristic regimes in frequency-dependent dynamic reorientation of fibroblasts on cyclically stretched substrates. *Biophysical Journal* **95** (2008), 3470–3478.

[20] Lauffenburger, D. A. & Horwitz, A. F.: Cell migration: a physically integrated molecular process. *Cell* **84** (1996), 359–369.

[21] Matthews, B. D.; Overby, D. R.; Mannix, R. & Ingber, D. E.: Cellular adaptation to mechanical stress: role of integrins, Rho, cytoskeletal tension and mechanosensitive ion channels. *Journal of Cell Science* **119** (2006), 508–518.

[22] Orr, A. W.; Helmke, B. P.; Blackman, B. R. & Schwartz, M. A.: Mechanisms of mechanotransduction. *Developmental Cell* **10** (2006), 11–20.

[23] Pellegrin, S. & Mellor, H.: Actin stress fibres. *Journal of Cell Science* **120** (2007), 3491–3499.

[24] Pollard, T. D.: The cytoskeleton, cellular motility and the reductionist agenda. *Nature* **422** (2003), 741–745.

[25] Rafelski, S. M. & Marshall, W. F.: Building the cell: design principles of cellular architecture. *Nature Reviews Molecular Cell Biology* **9** (2008), 593–602.

[26] Ridley, A. J.; Schwartz, M. A.; Burridge, K.; Firtel, R. A.; Ginsberg, M. H.; Borisy, G.; Parsons, J. T. & Horwitz, A. R.: Cell migration: integrating signals from front to back. *Science* **302** (2003), 1704–1709.

[27] Riedl, J.; Crevenna, A. H.; Kessenbrock, K.; Yu, J. H.; Neukirchen, D.; Bista, M.; Bradke, F.; Jenne, D.; Holak, T. A.; Werb, Z.; Sixt, M. & Wedlich-Soldner, R.: Lifeact: a versatile marker to visualize F-actin. *Nature Methods* **5** (2008), 605–607.

[28] Riveline, D.; Zamir, E.; Balaban, N. Q.; Schwarz, U. S.; Ishizaki, T.; Narumiya, S.; Kam, Z.; Geiger, B. & Bershadsky, a. D.: Focal contacts as mechanosensors: externally applied local mechanical force induces growth of focal contacts by an mDia1-dependent and ROCK-independent mechanism. *The Journal of cell biology* **153** (2001), 1175–1186.

[29] Turner, C. H.: Three rules for bone adaptation to mechanical stimuli. *Bone* **23** (1998), 1399–1407.

[30] Vogel, V. & Sheetz, M. P.: Cell fate regulation by coupling mechanical cycles to biochemical signaling pathways. *Current Opinion in Cell Biology* **21** (2009), 38–46.

[31] Wang, J. H.; Goldschmidt-Clermont, P. & Yin, F. C.: Contractility affects stress fiber remodeling and reorientation of endothelial cells subjected to cyclic mechanical stretching. *Annals of Biomedical Engineering* **28** (2000), 1165–1171.

[32] Wang, J. H.-C.: Substrate deformation determines actin cytoskeleton reorganization: a mathematical modelling and experimental study. *Journal of Theoretical Biology* **202** (2000), 33–41.

[33] Wang, J. H.-C. & Thampatty, B. P.: An introductory review of cell mechanobiology. *Biomechanics and Modeling in Mechanobiology* **5** (2006), 1–16.

[34] Wang, N.; Butler, J. P. & Ingber, D. E.: Mechanotransduction across the cell surface and through the cytoskeleton. *Science* **260** (1993), 1124–1127.

[35] Watanabe-Nakayama, T.; Machida, S.-I.; Harada, I.; Sekiguchi, H.; Afrin, R. & Ikai, A.: Direct detection of cellular adaptation to local cyclic stretching at the single cell level by atomic force microscopy. *Biophysical Journal* **100** (2011), 564–572.

[36] Woertche, E.; Deibler, M.; Schulz, S.; Steinberg, T.; Kemkemer, R. & Tomakidi, P.: Kinetic fingerprint discriminates similar cell populations subjected to uniaxial cyclic tensile strain on flexible substrates. *Soft Matter* **7** (2011), 8612.

[37] Wozniak, M. a. & Chen, C. S.: Mechanotransduction in development: a growing role for contractility. *Nature Reviews Molecular Cell Biology* **10** (2009), 34–43.

[38] Yoshigi, M.; Clark, E. B. & Yost, H. J.: Quantification of stretch-induced cytoskeletal remodeling in vascular endothelial cells by image processing. *Cytometry. Part A: The journal of the International Society for Analytical Cytology* **55** (2003), 109–118.

[39] Zhu, C.; Bao, G. & Wang, N.: Cell mechanics: mechanical response, cell adhesion, and molecular deformation. *Annual Review of Biomedical Engineering* **2** (2000), 189–226.

A Porous Media Model for the Description of Avascular Tumour Growth

R. Krause, B. Markert & W. Ehlers

Institute of Applied Mechanics (CE), University of Stuttgart,
Pfaffenwaldring 7, 70569 Stuttgart, Germany

SimTech – Cluster of Excellence, University of Stuttgart,
Pfaffenwaldring 5a, 70569 Stuttgart, Germany

Abstract. Avascular tumours are acclumerations of neoplastic cells without blood supply. Neoplastic cells proliferate uncontrolled if enough nutrients are available. Therefore, the local growth rate is governed by the amount of nutrients delivered via diffusive transport.
In the context of the Theory of Porous Media (TPM), a phenomenolgical model of avascular tumour growth is introduced, which is able to describe the local accretion and reduction of cells. The tumour cell tissue is treated as an aggregate of two immiscible constituents. In this idealised biphasic macro-model, the aggregate consists, firstly, of an extracellular matrix (ECM) and cells summarised to a solid phase and, secondly, of a fluid phase comprising extracellular and interstitial liquids, necrotic debris as well as cell precursors. Additionally, the growth-energy concentration is introduced as an additional quantity, which measures the average amount of chemical energy available for cell metabolism, and thus, controls the growth process. The addition and removal of cell material is described by a mass exchange between the solid and fluid constituents, which is controlled by the local growth energy concentration.
The numerical treatment of the coupled multi-field equations is carried out within the mixed finite element method proceeding from an implicit monolithic solution strategy. The simulation of a growing tumour spheroid finally reveals the capabilities of the model.

1 Introduction

Biological tissues are composed of many constituents, like various cell types, abundant water, extracellular matrix (ECM), etc., cf. Cowin [8] for details. Growth processes cause changes in the relative amount of these components and their properties. In the last decades, continuum mechanics was extensively applied in the context of material modelling of hard and soft biological tissues, such as bone, cartilage or muscle, where nonlinear, inelastic and anisotropic properties have been addressed. Reviews of achievements in the biomechanics of biological tissues including growth and remodelling are given by Taber [20] and Humphrey [12].
Here, particularly focussing on tumour growth processes, it is apparent that growing tissues not only undergo changes in size and shape but also in their

inner structure. In singlephasic models, the internal changes are described employing the open-system theory. Thereby, only the cells and the ECM are assumed to influence the overall mechanical behaviour and the fluid constituents are neglected. This concept has been applied to growing tumour spheroids by Ambrosi & Mollica [3, 4], using an open singlephasic material model with an additional nutrient concentration that triggers the growth process. A recent overview of different tumour models is given by Unnikrishnan *et al.* [22].

Multiphasic models, which also include extracellular fluid, are proposed by Ambrosi & Preziosi [5] and Byrne & Preziosi [7] for the description of avascular tumours. Moreover, Preziosi & Tosin [18] describe a region of tumour and healthy cells using a triphasic material description.

In the present article, a general framework for the description of non-equilibrium growth processes in tumours is developed. Therefore, cells and the extracellular matrix as well as the extracellular fluid are considered as individual components of the growing biological tissue. In addition, it is necessary to take diffusion and consumption of metabolites (oxygen, glucose, ATP, etc.) into account. However, it seems to be impossible to include all metabolic mechanisms into a continuum-mechanical macro model. Therefore, following the ideas of Markert & Ehlers [16] as well as Ambrosi & Guillou [2], a single, non-mechanical quantity is introduced to summarise the metabolites insight the extracellular fluid. This method provides the necessary thermodynamic restrictions, which are evaluated for avascular tumour growth.

To reveal the capability of the multi-field continuum model, the governing coupled system of partial differential equations is numerically treated by use of the mixed finite element method. Based on a direct implicit solution procedure, an exemplary simulation of a 3-d growing tumour spheroid is presented.

2 Preliminaries

Biological tissues are multiphasic, porous materials, which are formed by several interacting components. To describe the mechanical behaviour of the overall biological material, it is necessary to consider its individual constituents. In this contribution, tumour tissue is modelled as a multiphasic continuum φ, which basically consists of superimposed and interacting solid and fluid phases φ^α ($\alpha \in \{S, F\}$), see Figure 1. In particular, the extracellular matrix and the adhering cells are summarised within the solid phase φ^S. These are surrounded by the extracellular fluid, which is subsumed in the fluid phase φ^F. However, the extracellular fluid is itself a homogeneous solution, which contains several mixture components, i. e., $\varphi^F = \cup_\beta \varphi^\beta$ with $\beta \in \{L, \gamma\}$. In detail, these mixture components are divided into a solvent φ^L (liquid water) and several solutes φ^γ (nutrients, glucose, cell and matrix precursors, cell debris, etc.).

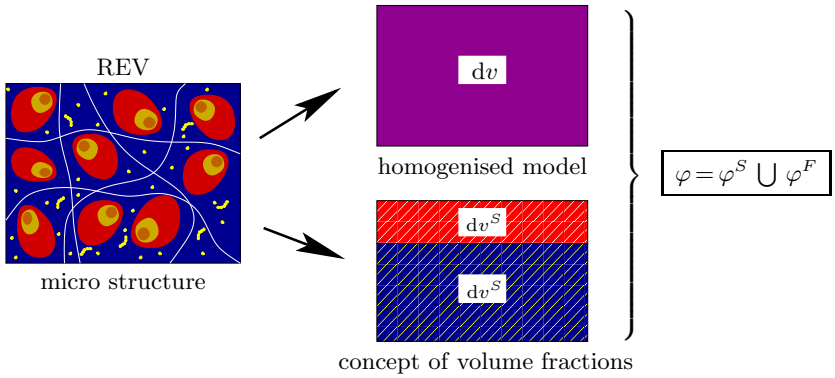

Fig. 1. Representative elementary volume (REV) of the biological microstructure and biphasic macro model.

2.1 Immiscible Phases and Volume Fractions

The immiscible phases φ^α are described by their volume fractions $n^\alpha = \mathrm{d}v^\alpha/\mathrm{d}v$ (partial volume $\mathrm{d}v^\alpha$ per bulk volume $\mathrm{d}v$), which must fulfil the saturation constraint

$$\sum_\alpha n^\alpha = n^S + n^F = 1\,. \tag{1}$$

Furthermore, the partial density $\rho^\alpha = \mathrm{d}m^\alpha/\mathrm{d}v$ and the material or realistic density $\rho^{\alpha R} = \mathrm{d}m^\alpha/\mathrm{d}v^\alpha$ both defined with the constituent mass element $\mathrm{d}m^\alpha$ are related to each other via the volume fraction n^α:

$$\rho^\alpha = n^\alpha \rho^{\alpha R}\,. \tag{2}$$

Summation over the partial densities ρ^α yields the density ρ of the overall aggregate:

$$\rho = \sum_\alpha \rho^\alpha = \rho^S + \rho^F\,. \tag{3}$$

2.2 Miscible Components and Partial Pore Densities

The fluid phase is an ideal mixture that contains several miscible components φ^β. These are described by employing the partial pore density ρ_F^β, which relates the fluid mixture component mass to the fluid volume:

$$\rho^\beta = n^F \rho_F^\beta\,, \quad \text{where} \quad \rho_F^\beta = \frac{\mathrm{d}m^\beta}{\mathrm{d}v^F}\,. \tag{4}$$

Summation over the partial pore densities ρ_F^β of the fluid mixture components yields the material density ρ^{FR} of the fluid phase, which, in the context of the Theory of Mixtures (TM), can be interpreted as the fluid mixture density:

$$\rho^{FR} = \sum_\beta \rho_F^\beta \,. \tag{5}$$

2.3 Kinematic Relations

The kinematics is based on the concept of superimposed continua [cf., e. g., 9, 10]. Within this framework, each material point P^α is characterised by its position $\mathbf{X}_\alpha$ in the reference configuration at time $t = t_0$ and follows its individual
motion function $\mathbf{x} = \boldsymbol{\chi}_\alpha(\mathbf{X}_\alpha, t)$. Hence, each spatial point $\mathbf{x}$ is occupied at every time t by material points of all constituents, which in addition have their own velocity field

$$\mathbf{v}_\alpha = \overset{\prime}{\mathbf{x}}_\alpha = \frac{\mathrm{d}\,\boldsymbol{\chi}_\alpha(\mathbf{X}_\alpha, t)}{\mathrm{d}t} \quad \text{with} \quad (\cdot)'_\alpha = \frac{\mathrm{d}_\alpha}{\mathrm{d}t}(\cdot) = \frac{\partial\,(\cdot)}{\partial t} + \operatorname{grad}(\cdot)\cdot\mathbf{v}_\alpha \,, \tag{6}$$

where $\operatorname{grad}(\cdot) = \partial(\cdot)/\partial\mathbf{x}$. The motion of the solid constituent φ^S is given by the solid displacement vector $\mathbf{u}_S$, whereas the fluid motion is described relative to the deforming solid using the seepage velocity $\mathbf{w}_F$. Thus,

$$\mathbf{u}_S = \mathbf{x} - \mathbf{X}_S \,, \quad \mathbf{w}_F = \mathbf{v}_F - \mathbf{v}_S \,, \quad \text{where} \quad \mathbf{v}_S = (\mathbf{u}_S)'_S = \overset{\prime}{\mathbf{x}}_S \,. \tag{7}$$

Concerning the fluid components φ^β, the overall fluid mixture velocity $\mathbf{v}_F$ as well as the mixture-component diffusion velocities $\mathbf{d}_{\beta F}$ and the corresponding seepage velocities $\mathbf{w}_\beta$ are given by

$$\mathbf{v}_F = \frac{1}{\rho^{FR}} \sum_\beta \rho_F^\beta \mathbf{v}_\beta \,, \quad \mathbf{d}_{\beta F} = \mathbf{v}_\beta - \mathbf{v}_F \quad \text{and} \quad \mathbf{w}_\beta = \mathbf{v}_\beta - \mathbf{v}_S \,. \tag{8}$$

Herein, $\mathbf{v}_\beta$ denotes the velocity of φ^β in analogy to (6). Moreover, the following relations hold:

$$(\,\cdot\,)'_F = (\,\cdot\,)'_S + \operatorname{grad}(\,\cdot\,)\cdot\mathbf{w}_F \quad \text{and} \quad (\,\cdot\,)'_\beta = (\,\cdot\,)'_S + \operatorname{grad}(\,\cdot\,)\cdot\mathbf{w}_\beta \,. \tag{9}$$

The deformation gradient $\mathbf{F}_\alpha$ and the spatial velocity gradient $\mathbf{L}_\alpha$ are introduced via

$$\mathbf{F}_\alpha = \frac{\partial\,\mathbf{x}}{\partial\mathbf{X}_\alpha} =: \operatorname{Grad}_\alpha \mathbf{x} \quad \text{and} \quad \mathbf{L}_\alpha = \frac{\partial\,\mathbf{v}}{\partial\mathbf{x}} = \operatorname{grad}\mathbf{v}_\alpha. \tag{10}$$

2.4 Balance Equations

In this section, the constituent balance equations of mass and momentum are introduced. The balance equations of the overall material can be obtained as a result of the balance equations of the constituents [21]. For a detailed derivation of the local balance equations, we refer to Ehlers [9, 10]. Here, proceeding from isothermal, quasi-static conditions and waving inertia terms, the partial balance equations of mass and momentum read:

$$(\rho^\alpha)'_\alpha + \rho^\alpha \operatorname{div} \mathbf{v}_\alpha = \hat{\rho}^\alpha \quad \text{with} \quad \sum_\alpha \hat{\rho}^\alpha = 0\,, \tag{11}$$

$$\mathbf{0} = \operatorname{div} \mathbf{T}^\alpha + \rho^\alpha \mathbf{b}^\alpha + \hat{\mathbf{p}}^\alpha \quad \text{with} \quad \mathbf{0} = \sum_\alpha \big(\hat{\mathbf{p}}^\alpha + \hat{\rho}^\alpha \mathbf{v}_\alpha\big)\,. \tag{12}$$

Therein, the local mass production $\hat{\rho}^\alpha$ results from a mass exchange process among the constituents, which is used to model the growth process. $\mathbf{T}^\alpha$ and $\mathbf{b}^\alpha$ denote the partial symmetric Cauchy stress tensor and the volume force acting on φ^α. Furthermore, $\hat{\mathbf{p}}^\alpha$ is the direct momentum production of φ^α, which describes the local momentum exchange between the constituents. The summation constraints $(11)_2$ and $(12)_2$ hold due to the overall conservation of mass and of momentum in a closed mixture system.
Concerning the miscible fluid components, the mass balance (11) can be rewritten employing the partial pore density ρ_F^β:

$$(n^F \rho_F^\beta)'_\beta + n^F \rho_F^\beta \operatorname{div} \mathbf{v}_\beta = n^F \hat{\rho}_F^\beta \quad \text{with} \quad n^F \hat{\rho}_F^\beta = \hat{\rho}^\beta\,. \tag{13}$$

For the materially incompressible phases, division of (11) by the constant material density $\rho^{\alpha R}$ leads to the constituent volume balance

$$(n^\alpha)'_\alpha + n^\alpha \operatorname{div} \mathbf{v}_\alpha = \hat{n}^\alpha \quad \text{with} \quad \hat{n}^\alpha := \frac{\hat{\rho}^\alpha}{\rho^{\alpha R}} \tag{14}$$

as the respective volume production, which, in general, does not add up to zero $\sum_\alpha \hat{n}^\alpha \neq 0$. Analytical integration of the solid volume balance yields:

$$n^S = \underbrace{n_{0S}^S \exp\Big(\int_{t_0}^{t} \frac{\hat{n}^S}{n^S} \mathrm{d}t\Big)}_{n_{tS}^S} (\det \mathbf{F}_S)^{-1} = n_{tS}^S (\det \mathbf{F}_S)^{-1}\,. \tag{15}$$

Therein, the solid volume fraction is multiplicatively split into a deformation-dependent part $(\det \mathbf{F}_S)^{-1}$ and a growth-dependent part n_{tS}^S. The quantity n_{0S}^S denotes the initial solid volume fraction at time $t = t_0$ and n_{tS}^S denotes the solid volume fraction at time $t \geq t_0$ associated with an accompanying reference configuration [cf. 13] or an intermediate configuration [cf. 1, 4].

3 Constitutive Modelling

To close the continuum-mechanical problem, constitutive information is necessary to describe the properties of the growing multiphasic material. In particular, specific constitutive equations for the partial Cauchy stress tensor $\mathbf{T}^\alpha$ as well as the volume production $\hat{n}^\alpha$ and the direct momentum production $\hat{\mathbf{p}}^\alpha$ are provided.

3.1 Modelling Assumptions

The following considerations proceed from an isothermal, biphasic material description under quasi-static conditions with a fluid mixture and a solid phase, which are both materially incompressible ($\rho^{\alpha R} = \text{const.}$). Moreover, the fluid constituent is treated as a dilute solution that mainly consists of water with low concentrations of dissolved molecules. In particular, the mixture components are separated into the liquid solvent φ^L and several dissolved solutes φ^γ ($\gamma \in \{1, 2, \dots, N\}$ with N as the number of considered solutes). Here, only those metabolites contributing to the cellular energy metabolism are considered explicitly, while the remaining components of the extracellular fluid are assumed to be sufficiently available within the extracellular fluid solution, such that they do not hinder the biological processes. They are considered implicitly as a part of the solvent φ^L. Moreover, it is assumed that the partial solute densities per extracellular fluid volume are marginal, such that their contribution to the fluid mixture density is negligibly small[1]:

$$\rho^{FR} \approx \rho_F^L = \text{const.} \quad \text{and} \quad \frac{\rho_F^\gamma}{\rho^{FR}} \approx 0\,. \tag{16}$$

Inserting these assumptions into (8) and proceeding from finite component velocities $\mathbf{v}_\gamma$, yields that the velocity of the solvent $\mathbf{v}_L$ is identical with the fluid mixture velocity $\mathbf{v}_F$, i. e.,

$$\mathbf{v}_L \approx \mathbf{v}_F \quad \Longrightarrow \quad \mathbf{d}_{LF} \approx \mathbf{0}\,. \tag{17}$$

Hence, the mechanical properties of the fluid mixture are assumed to be identical to those of the solvent.

3.2 Growth-Energy Concept

Following the idea of Markert & Ehlers [16], the vast amount of dissolved chemical molecules is summarised in one quantity: the growth energy $\mathcal{C}^F$. This concept is also known from the energy value on food labels. It is biologically motivated by the cellular energy metabolism, where the metabolisation

[1] The extracellular fluid of a healthy person has a partial glucose density in the range of $\rho_F^\gamma \approx$ 0.7-1.0 g/l [cf. 14, p. 70], which is negligible compared to the partial density of the solvent water $\rho_F^L \approx 1.0$ kg/l.

of a certain substrate, i. e. the reactant of a metabolic reaction, follows a fixed metabolic pathway and always yields the synthesis of the same amount of adenosine triphosphate (ATP). For details regarding the cellular energy metabolism, the interested reader is referred to Löffler [14][2]. Following this, the growth energy is obtained by summation over the fluid component densities multiplied with the respective constant energy values f^γ, i. e., the amount of energy that is gained from the respective component by cell metabolism:

$$\mathcal{C}^F := \sum_\gamma f^\gamma \rho_F^\gamma = f^\mathcal{C} \rho_F^\mathcal{C} \quad \text{with} \quad \rho_F^\mathcal{C} = \sum_\gamma \rho_F^\gamma \quad \text{and} \quad f^\mathcal{C} = \frac{\mathcal{C}^F}{\rho_F^\mathcal{C}} \,. \tag{18}$$

Therein, $\rho_F^\mathcal{C}$ denotes the growth-energy density per pore-fluid volume, and $f^\mathcal{C}$ is the averaged energy value of all growth-energy components.

Growth-Energy Balance With definition (18), the growth-energy balance is obtained by summation over the mass balances of the growth-energy components φ^γ weighted by the respective energy values f^γ. Hence, the growth-energy balance has the same structure as a mass balance reading

$$(n^F \mathcal{C}^F)'_\mathcal{C} + n^F \mathcal{C}^F \operatorname{div} \mathbf{v}_\mathcal{C} = \hat{\mathcal{C}}^F \,. \tag{19}$$

Therein, the growth-energy velocity $\mathbf{v}_\mathcal{C}$ and the growth-energy production $\hat{\mathcal{C}}^F$ are defined as

$$\mathbf{v}_\mathcal{C} := \mathbf{d}_{CF} + \mathbf{v}_F = \frac{1}{\mathcal{C}^F} \sum_\gamma f^\gamma \rho_F^\gamma \mathbf{v}_\gamma \quad \text{and} \quad \hat{\mathcal{C}}^F := n^F \sum_\gamma f^\gamma \hat{\rho}_F^\gamma \tag{20}$$

with the growth-energy diffusion velocity $\mathbf{d}_{CF}$.
The growth-energy production summarises the growth-energy consumption of the cells. In contrast to the overall mass production, the growth-energy production $\hat{\mathcal{C}}^F$ is in general not equal to zero. A negative growth-energy production indicates a nutrient consumption, and a positive production indicates a nutrient production (e. g., photosynthesis). This does not contradict the summation constraint of the constituent mass productions $(11)_2$, as the growth-energy production is obtained by a mass-preserving transfer among metabolic components with different energy values.

3.3 Constitutive Equations

Cauchy Stress Tensor The overall Cauchy stress tensor is obtained by summation of the constituent Cauchy stress tensors

$$\mathbf{T} = \mathbf{T}^S + \mathbf{T}^F \quad \text{with} \quad \mathbf{T}^S = \mathbf{T}_E^S - n^S p^{FR} \mathbf{I} \quad \text{and} \quad \mathbf{T}^F = -n^F p^{FR} \mathbf{I} \,. \tag{21}$$

[2] In particular, pp. 102 f: β-oxidation, fatty acid metabolism, pp. 105 f.: ketone body degradation, pp. 149 ff.: amino acid degradation, pp. 157 ff: citric acid cycle, glucose degradation

Therein, the constituent Cauchy stress tensors contain the fluid pressure p^{FR} and the solid extra stress tensor $\mathbf{T}^S_E$. The fluid frictional stresses are neglected. Regarding growing biological tissue, it is convenient to split the solid extra stress tensor into a purely mechanical part $\mathbf{T}^S_{E/\mathrm{mech}}$ and a growth-related part $\mathbf{T}^S_{E/\mathrm{grow}}$,

$$\mathbf{T}^S_E = \overbrace{\rho^S \frac{\partial \psi^S}{\partial \mathbf{F}_S}\mathbf{F}_S^T}^{\mathbf{T}^S_{E/\mathrm{mech}}} \overbrace{-\rho^{SR}(n^S)^2 \frac{\partial \psi^S}{\partial n^S}\mathbf{I}}^{\mathbf{T}^S_{E/\mathrm{grow}}} = \mathbf{T}^S_{E/\mathrm{mech}} + \mathbf{T}^S_{E/\mathrm{grow}}\,. \tag{22}$$

The mechanical part of the solid extra stress, $\mathbf{T}^S_{E/\mathrm{mech}}$, is described by a neo-Hookean elasticity law:

$$\mathbf{T}^S_{E/\mathrm{mech}} = \det\mathbf{F}_S\Big(\mu^S\big(\mathbf{B}_S - \mathbf{I}\big) + \lambda^S \ln\big(\det\mathbf{F}_S\big)\mathbf{I}\Big)\,. \tag{23}$$

Following Ambrosi & Preziosi [5], cell adhesion and repulsion are considered via the growth-dependent part of the extra stress tensor $\mathbf{T}^S_{E/\mathrm{grow}}$:

$$\begin{aligned} \mathbf{T}^S_{E/\mathrm{grow}} &= -n^S p^S_{\mathrm{grow}}\,\mathbf{I} \\ \text{with}\quad p^S_{\mathrm{grow}} &= \begin{cases} \alpha\dfrac{n^S}{n^{Sn}}\dfrac{\big(n^S - n^{St}\big)^2\big(n^S - n^{Sn}\big)}{\sqrt{1-n^S}} & \text{for } n^S \geq n^{St}\,, \\ 0 & \text{for } n^S < n^{St}\,. \end{cases} \end{aligned} \tag{24}$$

Therein, p^S_{grow} denotes the growth pressure, where in the natural state defined by n^{Sn} neither cell repulsion nor attraction occurs. In areas with a solid volume fraction below the threshold n^{St}, no interactions between the cells are possible since the cells are too far away from each other to interact. If the solid volume fraction n^S exceeds the value n^{Sn}, the cells are repulsing each other, and if $n^{St} < n^S < n^{Sn}$, the cells are attracting each other. A qualitative plot of p^S_{grow} is given in Figure 2.

Momentum Production Concerning the fluid and the growth-energy momentum productions, the effective production terms $\hat{\mathbf{p}}^F_E$ and $\hat{\mathbf{p}}^{\mathcal{C}}_E$ are introduced by separating the pressure-dependent part from the effective part of the production terms:

$$\begin{aligned} &\hat{\mathbf{p}}^F_E := \hat{\mathbf{p}}^F - p^{FR}\operatorname{grad} n^F \quad \text{and} \\ &\hat{\mathbf{p}}^{\mathcal{C}}_E := \hat{\mathbf{p}}^{\mathcal{C}} - \pi^{\mathcal{C}}\operatorname{grad} n^F \quad \text{with} \quad \pi^{\mathcal{C}} = \sum_\gamma \frac{f^\gamma \pi^\gamma}{f^{\mathcal{C}}}\,. \end{aligned} \tag{25}$$

Therein, $\pi^{\mathcal{C}}$ denotes a growth-energy related quantity equivalent to an osmotic pressure. Following Ehlers [10], appropriate constitutive assumptions for the effective momentum productions are given by

$$\hat{\mathbf{p}}^F_E = -(n^F)^2\frac{\gamma^{FR}}{k^F}\mathbf{w}_F \quad \text{and} \quad \hat{\mathbf{p}}^{\mathcal{C}}_E = -(n^F)^2\frac{R^{\mathcal{C}}\theta\rho^{\mathcal{C}}_F}{D^{\mathcal{C}}}\mathbf{d}_{CF} \tag{26}$$

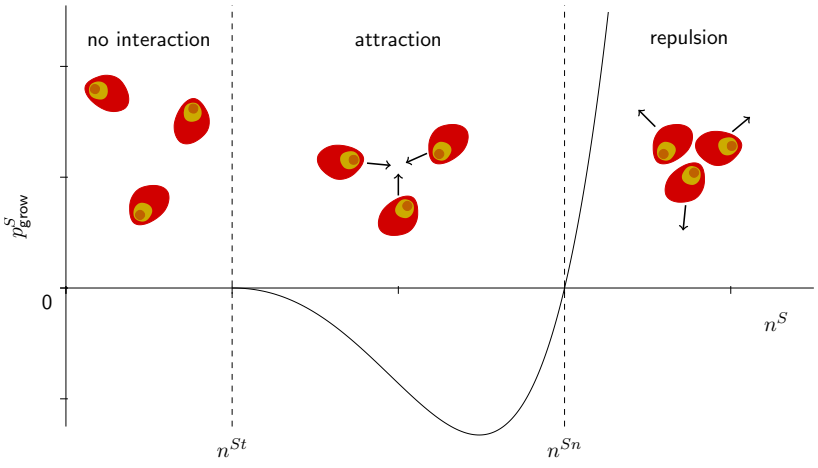

Fig. 2. Qualitative plot of the growth pressure p^S_{grow}.

with the conventional hydraulic conductivity k^F (isotropic Darcy permeability), the effective fluid weight γ^{FR} and the growth-energy diffusion coefficient $D^{\mathcal{C}}$. The parameter $R^{\mathcal{C}}$ is an equivalent to the specific gas constant, and θ is the absolute temperature.
Inserting (26) and $(21)_2$ in the momentum balance (12) yields the conditional equations of the seepage velocity and the growth-energy diffusion velocity

$$n^F \mathbf{w}_F = -\frac{k^F}{\gamma^{FR}} \operatorname{grad} p^{FR} \quad \text{and} \quad n^F \rho^{\mathcal{C}}_F \mathbf{d}_{CF} = -D^{\mathcal{C}} \operatorname{grad} \rho^{\mathcal{C}}_F \,. \tag{27}$$

These equations are commonly known as Darcy's law and Fick's law.

Mass and Growth-Energy Production The solid mass production describes the degenerative and regenerative processes that occur within a biological tissue. In the context of tumour growth, the regenerative process describes the cell proliferation, and cell apoptosis and necrosis are considered as degenerative processes. The solid volume production is therefore additively split into a part that describes the degenerative process $\hat{n}^S_{\text{deg}}$ and another part that describes the regenerative process $\hat{n}^S_{\text{reg}}$:

$$\hat{n}^S = \hat{n}^S_{\text{reg}} - \hat{n}^S_{\text{deg}} \quad \text{with} \quad \hat{n}^S_{\text{reg}} \geq 0 \quad \text{and} \quad \hat{n}^S_{\text{deg}} \geq 0 \,. \tag{28}$$

Furthermore, the growth-energy production is additively split into a basal-metabolic part $\hat{\mathcal{C}}^F_{\text{basal}}$ and an additional growth-dependent part $\hat{\mathcal{C}}^F_{\text{grow}}$. The basal-metabolic part denotes the growth-energy consumption of cells in a quiescent state, and the growth-dependent part describes the additional growth-

energy consumption if the tissue is proliferating:

$$\hat{\mathcal{C}}^F = \hat{\mathcal{C}}^F_{\text{basal}} + \hat{\mathcal{C}}^F_{\text{grow}} \quad \text{with} \quad \begin{cases} \hat{\mathcal{C}}^F_{\text{basal}} = -k_{\text{basal}}\, n^S\,, \\ \hat{\mathcal{C}}^F_{\text{grow}} = -k_{\text{grow}}\, \hat{n}^S_{\text{reg}}\,. \end{cases} \tag{29}$$

As a consequence of thermodynamic considerations, cell proliferation is only possible if the growth energy exceeds a certain threshold value. Concerning the degenerative process, here, only necrotic cell death caused by malnutrition (nutrient starvation) is considered. Thereby, it is assumed that the considered tumour cells have lost their ability to initiate an apoptotic cell death. Accordingly, the solid volume production is calculated by employing a Mechalis-Menten-type reaction equation, where a regenerative process is considered if the growth-energy exceeds the threshold $\mathcal{C}^F_0$, and a degenerative process is considered if the growth-energy is below this threshold:

$$\hat{n}^S = \begin{cases} \hat{n}^S_{\text{reg}} = \gamma\, n^S n^F \dfrac{\mathcal{C}^F - \mathcal{C}^F_0}{K^{\mathcal{C}+}_M + (\mathcal{C}^F - \mathcal{C}^F_0)} & \text{if} \quad \mathcal{C}^F > \mathcal{C}^F_0\,, \\ \hat{n}^S_{\text{deg}} = \delta\, n^S n^F \dfrac{\mathcal{C}^F_0 - \mathcal{C}^F}{K^{\mathcal{C}-}_M + (\mathcal{C}^F_0 - \mathcal{C}^F)} & \text{if} \quad \mathcal{C}^F \leq \mathcal{C}^F_0\,. \end{cases} \tag{30}$$

Herein, $K^{\mathcal{C}+}_M$ and $K^{\mathcal{C}-}_M$ denote the Michaelis constants representing the growth-energy at which the volume production is half of its maximum.

4 Numerical Treatment

For the numerical treatment of initial-boundary-value problems, the weak formulation of the governing partial differential equations are implemented and numerically discretised in space and time. The presented continuum-mechanical growth model is governed by five independent field variables: the solid displacement vector $\mathbf{u}_S$, the fluid seepage velocity $\mathbf{w}_F$, the effective fluid pressure p^{FR}, the growth-energy diffusion velocity $\mathbf{d}_{CF}$ and the growth energy $\mathcal{C}^F$. However, by use of $(27)_1$, the filter velocity $n^F\mathbf{w}_F$ is obtained as a function of the pressure gradient, and the growth-energy gradient governs $\mathbf{d}_{CF}$ via $(27)_2$. Hence, the fluid seepage velocity and the growth-energy diffusion velocity can be substituted by the respective gradient terms. Accordingly, the number of independent field variables reduces to three, and $\mathbf{w}_F$ and $\mathbf{d}_{CF}$ can be computed in a post-processing step. In summary, the governing equations are the overall momentum balance

$$\mathbf{0} = \operatorname{div}\big(\mathbf{T}^S_E - p^{FR}\mathbf{I}\big)\,, \tag{31}$$

which is obtained by summation over the partial momentum balances (12), the mixture volume balance (14)

$$0 = -\operatorname{div}\big(\mathbf{v}_S + n^F\mathbf{w}_F\big)\,, \tag{32}$$

which is obtained by summation over the constituent volume balances, and the growth-energy balance: (19)

$$0 = n^F (\mathcal{C}^F)'_S + \mathcal{C}^F \operatorname{div} \mathbf{v}_S + \operatorname{div}\left[n^F \mathcal{C}^F (\mathbf{w}_F + \mathbf{d}_{CF})\right] - \hat{\mathcal{C}}^F \,. \tag{33}$$

Therein, it must be taken into account that $\hat{\mathbf{p}}^S + \hat{\mathbf{p}}^F = \hat{n}^S \rho^{SR} \mathbf{w}_F$. However, concerning the mixture volume and momentum balances, influences of the solid volume production are negligible since the considered biological growth processes are slow and differences of densities and of the velocities of the involved constituents are finite. Furthermore, $\mathbf{T}^S_E(\mathbf{u}_S)$ and $\hat{n}^S$ are given by (22) and (28), $\mathbf{v}_S = (\mathbf{u}_S)'_S$, cf. (6), and $\hat{\mathcal{C}}^F$ according to (29).

4.1 Weak Formulation

Following the standard Galerkin procedure (Bubnov-Galerkin), a weak formulation of the governing balance relations is obtained by multiplying the strong formulation by a test function followed by an integration over the domain Ω and integration by parts to obtain boundary terms. This procedure leads to the weak formulation of the overall momentum balance:

$$\mathcal{G}_{\mathbf{u}_S} = \int_\Omega \left(\mathbf{T}^S_E - p^{FR}\,\mathbf{I}\right) \cdot \operatorname{grad} \delta\mathbf{u}_S \,\mathrm{d}v - \int_{\Gamma_t} \bar{\mathbf{t}} \cdot \delta\mathbf{u}_S \,\mathrm{d}a = 0 \,. \tag{34}$$

Therein, $\delta\mathbf{u}_S$ denotes the test function and $\bar{\mathbf{t}} = (\mathbf{T}^S_E - p^{FR}\,\mathbf{I})\mathbf{n}$ is the total external load vector, which acts on the Neumann boundary Γ_t of the overall medium, where $\mathbf{n}$ denotes the outward-oriented unit surface normal.
Analogously, the weak formulation of the overall volume balance is found by multiplication with the test function δp^{FR} and integration over the domain Ω:

$$\begin{aligned} \mathcal{G}_{p^{FR}} = &\int_\Omega \left[\operatorname{div} \mathbf{v}_S \,\delta p^{FR} + \frac{k^F}{\gamma^{FR}} \operatorname{grad} p^{FR} \cdot \operatorname{grad} \delta p^{FR}\right] \mathrm{d}v + \\ &+ \int_{\Gamma_v} \bar{v}^F \,\delta p^{FR} \,\mathrm{d}a = 0 \,. \end{aligned} \tag{35}$$

Herein, $\bar{v}^F = -k^F/\gamma^{FR} \operatorname{grad} p^{FR} \cdot \mathbf{n}$ denotes the fluid volume efflux through the Neumann boundary Γ_v.
Applying the same procedure to the growth-energy balance using the test function $\delta\mathcal{C}^F$ yields

$$\begin{aligned} \mathcal{G}_{\mathcal{C}^F} = &\int_\Omega \left[n^F (\mathcal{C}^F)'_S + \mathcal{C}^F \operatorname{div} \mathbf{v}_S - \hat{\mathcal{C}}^F\right] \delta\mathcal{C}^F \mathrm{d}v + \\ &+ \int_\Omega \left(\mathcal{C}^F \frac{k^F}{\gamma^{FR}} \operatorname{grad} p^{FR} + D^{\mathcal{C}} \operatorname{grad} \mathcal{C}_F\right) \cdot \operatorname{grad} \delta\mathcal{C}^F \mathrm{d}v + \\ &+ \int_{\Gamma_d} \bar{d}^{\mathcal{C}} \,\delta\mathcal{C}^F \mathrm{d}a = 0 \,. \end{aligned} \tag{36}$$

Therein, $\bar{d}^{\mathcal{C}} = -\big(\mathcal{C}^F k^F/\gamma^{FR} \operatorname{grad} p^{FR} + D^{\mathcal{C}} \operatorname{grad} \mathcal{C}_F\big) \cdot \mathbf{n}$ denotes the growth-energy efflux through the Neumann boundary Γ_d, e. g., parenteral nutrition. Since the growth energy only influences slow growth and remodelling processes and has no influence on the mechanical behaviour, short-time fluctuations of the growth energy are neglected. On the large time scale of growth processes, the growth energy is assumed to be at a quasi-steady state with $(\mathcal{C}^F)'_S = 0$.

4.2 Solution Procedure

To solve the three-field variational problem, an implicit monolithic solution strategy is used. Therefore, the spatial domain Ω is approximated by a discrete domain Ω^h with N_e finite elements, and the resulting system of semi-discrete differential-algebraic equations (DAE) of first order in time is solved using an implicit Euler scheme. However, the use of equal approximation orders may lead to strongly mesh-dependent results with strange instabilities that arise from spurious pressure modes if low permeabilities k^F and materially incompressible constituents are considered [15, p. 418f]. More precisely, the patch test or the inf-sub condition (also known as Ladyzhenskaya-Babuška-Brezzi (LBB) condition) must be fulfilled [cf. 6, p. 210]. These conditions are satisfied if the approximations for shape and test functions of the solid displacement are chosen one order higher than the approximations used for shape and test functions of the fluid pressure and the growth energy. Quadratic approximations for the solid displacement and linear approximations for the other primary variables are the simplest combination that yields stable solutions and is known as Taylor-Hood element [15, p. 418f].

4.3 Internal Variables

The growth processes within biological tissues are modelled by changes of the volume fraction of the accompanying reference configuration n^S_{tS}. It is possible to calculate the growth process globally by introducing an additional field variable or locally at every integration point[cf. 23].
For a global calculation, the solid volume fraction n^S must be used as an additional degree of freedom of the finite element system with the solid volume balance $(14)_{\alpha=S}$ as governing equation readily blowing up the system size. Here, the solid volume fraction is calculated locally in the sense of a collocation method by introducing n^S_{tS} as an internal history variable. Therefore, the ordinary differential equation

$$\mathcal{L}^h_n = (n^S_{tS})'_S - \hat{n}^S \det \mathbf{F}_S = 0 \tag{37}$$

is solved at every integration point $\mathbf{x}^h_n$ of the finite element mesh. The result is then used to obtain the actual solid volume fraction n^S from (15).

5 Numerical Example

As a numerical example, three avascular tumours with different proliferation rates are calculated. It is taken into account that tumour cells differ in their proliferation rate depending on tumour type and malignancy. The volume is discretised by 896 finite elements using 20-node brick elements. The results are obtained by calculating one eighth of an unloaded tumour spheroid with an initial diameter of 50 micrometer, cf. Figure 3. The initial and boundary conditions are adopted form Ehlers *et al.* [11]. Thereby, symmetry conditions are used on the inner surfaces. On the outer surface, a pore pressure of zero and a growth-energy value that lies inside the physiological range are applied and held constant during the calculation.

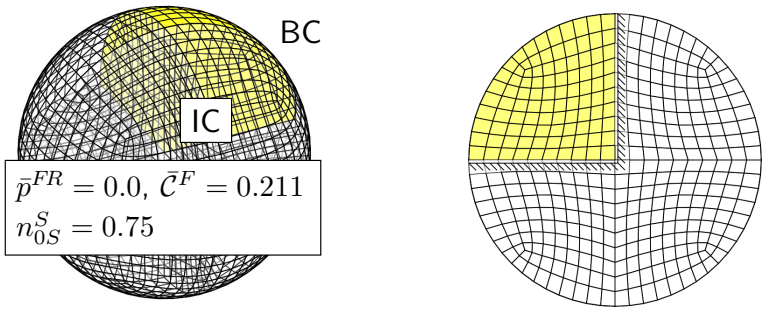

Fig. 3. Considered initial-boundary-value problem, adopted from Ehlers *et al.* [11], proceeding from an initial solid volume fraction of $n^{S}_{0S} = 0.75$, and using symmetry boundary conditions on the inner surfaces.

For the simulations, PANDAS was used as numerical framework. PANDAS is a numerical tool, which is designed to efficiently solve porous media problems. It includes the mixed finite element method as well as Diagonally Implicit Runge-Kutta methods (DIRK), such as implicit Euler techniques, for global and local equation systems.
The simulations proceed from an initial volume fraction of $n^{S}_{0S} = 0.75$, the material parameters given in Table 1 and varying proliferation coefficients $\gamma = \{3.0 \times 10^{-5}, 1.5 \times 10^{-5}, 7.5 \times 10^{-6}\}$ [cm^3/(J s)]. In Figure 4, the ratios of tumour radii of the simulations to the initial radius are depicted and compared to in-vitro experiments [19]. Figure 5 depict results of the qualitative three-dimensional simulation. The colouring indicates the distribution of the tumour cell volume fractions. Within the spheroids, three regions can be identified: the outer rim (red), where the cells are proliferating, a transient region with quiescent cells (yellow) and the necrotic core without living cells (blue). At the end of the simulation depicted in Figure 5, top right, the tumour surface begins to buckle. This results from the fact that the tumour surface

Table 1. Material parameters used for the tumour growth example.

parameter	symbol	value	SI unit
1st Lamé constant of the solid skeleton	μ^S	1.0×10^{-5}	$\mathrm{N/cm^2}$
2nd Lamé constant of the solid skeleton	λ^S	5×10^{-5}	$\mathrm{N/cm^2}$
effective density of dense solid	ρ^{SR}	1.3×10^{-3}	$\mathrm{kg/cm^3}$
effective density of pore-fluid mixture	ρ^{FR}	1.0×10^{-3}	$\mathrm{kg/cm^3}$
Darcy permeability	k^F	3.0×10^{-2}	cm/s
natural solid volume fraction	n^{Sn}	0.75	—
cell interaction threshold	n^{St}	0.65	—
growth stress constant	α	50	$\mathrm{N/cm^2}$
tumour proliferation coefficient	γ	variant	$\mathrm{cm^3/(J\,s)}$
tumour necrosis coefficient	δ	1.5×10^{-5}	1/s
boundary and initial growth-energy value	$\bar{\mathcal{C}}^F$	2.11×10^{-1}	$\mathrm{J/cm^3}$
growth-energy threshold value	$\mathcal{C}_0^F$	1.05×10^{-1}	$\mathrm{J/cm^3}$
basal metabolic growth-energy consumption	k^{bm}	1.0×10^{-4}	$\mathrm{J/(cm^3\,s)}$
additional growth-energy consumption	k_{gr}^r	60.0	$\mathrm{J/cm^3}$
growth-energy diffusion coefficient	$D^{\mathcal{C}}$	2.0×10^{-8}	cm/s
growth Michaelis constant	$K_M^{\mathcal{C}+}$	3.0×10^{-2}	cm/s
necrosis Michaelis constant	$K_M^{\mathcal{C}-}$	2.0×10^{-2}	cm/s

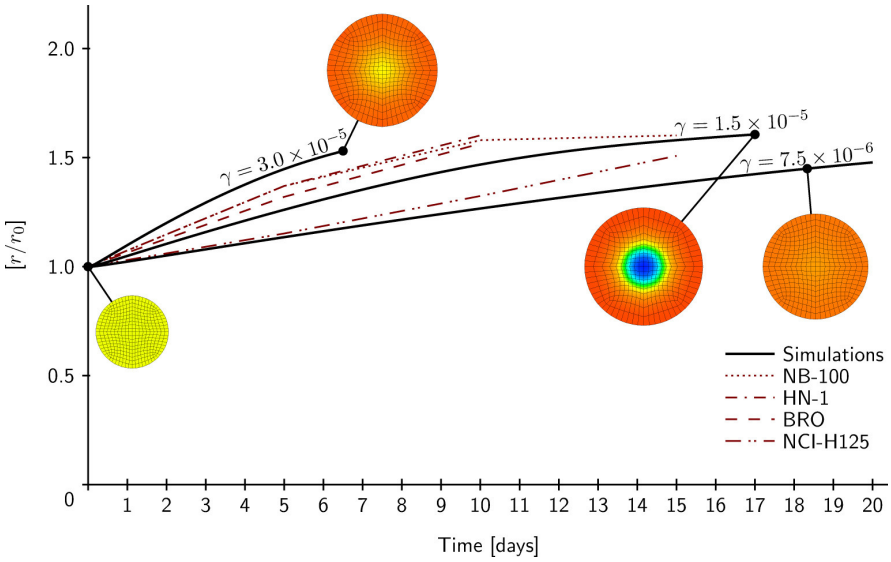

Fig. 4. Development of the outer tumour radius of the simulations related to its initial radius compared with experimental data given by Schwachöfer *et al.* [19, Figure 1, 100μg/ml], which are related to their size after 10 days.

grows faster than the inner domain yielding to surface instabilities, which can also be observed in in-vitro experiments. As can be seen, the model is

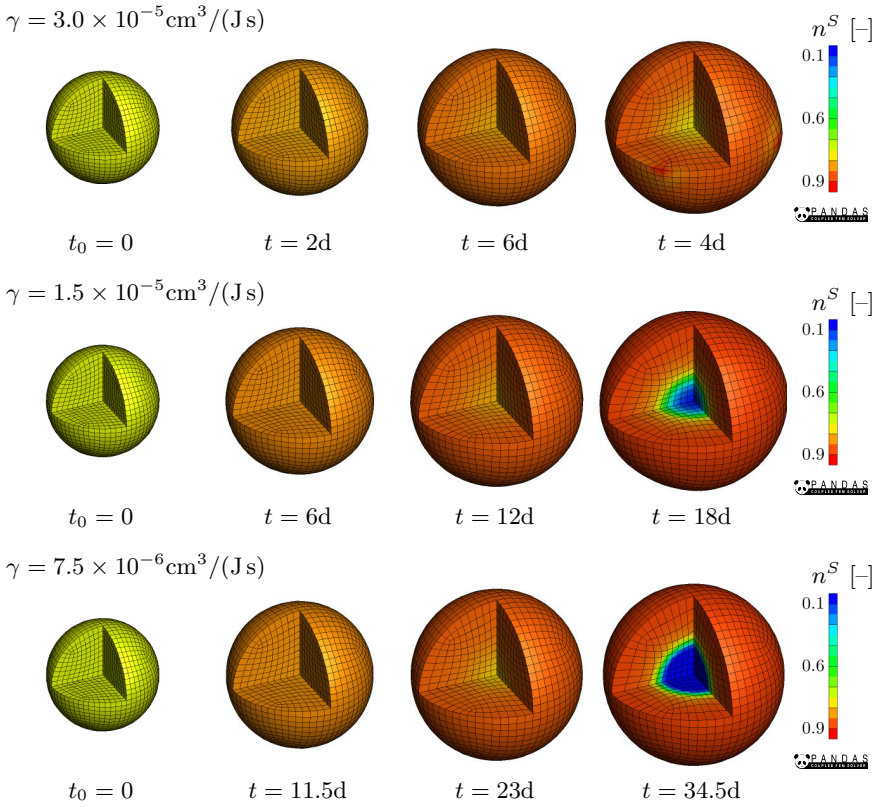

Fig. 5. Qualitative 3-d simulation results of a growing avascular tumour spheroid mapped with the distribution of the volume fraction of living tumour cells using variant proliferation coefficient γ.

in principle capable in mimicking the biologically correct growth behaviour. However, more investigations are necessary to provide reliable and cell-type specific predictions.

6 Conclusion and Future Work

The described modelling approach using a biphasic TPM model extended by the concept of growth energy provides an adequate framework for the description of avascular solid tumour growth. Thereby, the solid constituent describes the extracellular matrix and the cells, while the extracellular liquids including necrotic debris, interstitial liquids and the multiple components dissolved in them are described by the fluid constituent.
The growth-energy concept summarises the huge amount of nutrients, which are dissolved in the extracellular fluid, in their effect to a non-mechanical

quantity triggering the growth process. This concept reduces the numerical effort and allows for a thermodynamic evaluation of the constitutive equations for growth processes.
The model has then been applied to the prediction of the early stages of avascular tumour growth. An IBVP of a tumour spheroid and its solution calculated by PANDAS were presented. For the description of tumour growth, the growth-energy acts as the major trigger of the growth process. The model provides the basis for further investigations in the sense of a numerical laboratory (in-silico experiments). To extent this model towards vascular tumours that develop in a healthy tissue, vasculature and surrounding tissue can be included into this framework (cf. [17]).

Acknowledgements. The authors Robert Krause, Bernd Markert and Wolfgang Ehlers would like to thank the German Research Foundation (DFG) for financial support of the project within the Cluster of Excellence in Simulation Technology (EXC 310/1) at the University of Stuttgart.

References

[1] Ambrosi, D. & Guana, F.: Stress-modulated growth. *Mathematics and Mechanics of Solids* **12** (2007), 319–342.
[2] Ambrosi, D. & Guillou, A.: Growth and dissipation in biological tissues. *Continuum Mechanics and Thermodynamics* **19** (2007), 245–251.
[3] Ambrosi, D. & Mollica, F.: On the mechanics of a growing tumor. *International Journal of Engineering Science* **40** (2002), 1297–1396.
[4] Ambrosi, D. & Mollica, F.: The role of stress in growth of multicell spheroid. *Journal of Mathematical Biology* **48** (2004), 477–499.
[5] Ambrosi, L. & Preziosi, L.: On the closure of mass balance models for tumor growth. *Mahematical Models and Methods in Applied Sciences* **12** (2002), 737–754.
[6] Brezzi, F. & Fortin, M.: *Mixed and Hybrid Finite Element Methods.* Springer-Verlag, New York 1991.
[7] Byrne, H. & Preziosi, L.: Modelling solid tumour growth using the theory of mixtures. *Mathematical Medicine and Biology* **20** (2003), 341–366.
[8] Cowin, S. C.: How is a tissue built? *Journal of Biomechanical Engineering* **122** (2000), 553–569.
[9] Ehlers, W.: Foundations of multiphasic and porous materials. In Ehlers, W. & Bluhm, J. (eds.): *Porous Media: Theory, Experiments and Numerical Applications.* Springer-Verlag, Berlin 2002, pp. 3–86.
[10] Ehlers, W.: Challenges of porous media models in geo- and biomechanical engineering including electro-chemically active polymers and gels. *International Journal of Advances in Engineering Sciences and Applied Mathematics* **1** (2009), 1–24.

[11] Ehlers, W.; Markert, B. & Röhrle, O.: Computational continuum biomechanics with application to swelling media and growth phenomena. *GAMM–Mitteilungen* **32** (2009), 135–156.
[12] Humphrey, J. D.: Continuum biomechanics of soft biological tissues. *Proceedings of the Royal Society of London A* **459** (2003), 3–46.
[13] Humphrey, J. D. & Rajagopal, K. R.: A constrained mixture model for growth and remodeling of soft tissues. *Mahematical Models and Methods in Applied Sciences* **12** (2002), 407–430.
[14] Löffler, G.: *Basiswissen Biochemie mit Pathobiochemie*. Springer-Verlag, Berlin 2008, 7th edn., ISBN 3-540-44368-1.
[15] Markert, B.: A biphasic continuum approach for viscoelastic high-porosity foams: Comprehensive theory, numerics, and application. *Archives of Computational Methods in Engineering* **15** (2008), 371–446.
[16] Markert, B. & Ehlers, W.: Modeling and simulation of spheroidal tumor growth. In Bittnar, Z. & Mang, S. (eds.): *Proceedings of the ECCOMAS Thematic Conference on Modelling of Heterogeneous Materials*, Czech Technical University, Prague, Czech Republic 2007, pp. 24–25.
[17] Markert, B. & Häberle, K.: A phase-field model for the description of angiogenesis. *Computer Aided Medical Engineering* **2** (2011), 6–11.
[18] Preziosi, L. & Tosin, A.: Multiphase modelling of tumour growth and extracellular matrix interaction: mathematical tools and applications. *Journal of Mathematical Biology* **58** (2009), 625–656.
[19] Schwachöfer, J. H. M.; Hoogenhout, J. & Kal, H. B.: Three-dimensional culture of human tumor cells under standardized medium conditions. *Cytotechnology* **5** (1991), 265–271.
[20] Taber, L. A.: Biomechanics of growth, remodeling, and morphogenesis. *Applied Mechanics Reviews* **48** (1995), 487–545.
[21] Truesdell, C.: Thermodynamics of diffusion. In Truesdell, C. (ed.): *Rational Thermodynamics*. Springer-Verlag, New York 1984, 2nd edn., pp. 219–236.
[22] Unnikrishnan, G. U.; Unnikrishnan, V. U.; Reddy, J. N. & Lim, C. T.: Review on the constitutive models of tumor tissue for computational analysis. *Applied Mechanics Reviews* **63** (2010), 040801.
[23] Zienkiewicz, O. C. & Taylor, R. L.: *Finite Element Method*, vol. 2. McGraw-Hill Book Company, London 1989, 4 edn.

Author Index

List of Participants

Reza Abedian, M. Sc.
abedian.reza@ddh-gruppe.de
Labor für Biomechanik und Biomaterialien, Orthopädische Klinik
Medizinische Hochschule Hannover

Dipl.-Ing. Arzu Avci
avcia@mechbau.uni-stuttgart.de
Institut für Mechanik (Bauwesen)
Lehrstuhl für Kontinuumsmechanik
Universität Stuttgart

Prof. Dr.-Ing. Markus Böl
m.boel@tu-bs.de
Institut für Festkörpermechanik
Technische Universität Braunschweig

Prof. Dr.-Ing. Wolfgang Ehlers
ehlers@mechbau.uni-stuttgart.de
Institut für Mechanik (Bauwesen)
Lehrstuhl für Kontinuumsmechanik
Universität Stuttgart

Dipl.-Ing. Alexander Ehret
ehret@km.rwth-aachen.de
Lehr- und Forschungsgebiet
Kontinuumsmechanik
RWTH Aachen

Kristin Fietz, M. Sc.
fietz@ibnm.uni-hannover.de
Institut für Baumechanik und
Numerische Mechanik
Leibniz Universität Hannover

Dr. techn. Andreas Fritsch
andreas.fritsch@tuwien.ac.at
Institut für Mechanik der
Werkstoffe und Strukturen
Technische Universität Wien

Dipl.-Phys. Thomas Fritz
thomas.fritz@kit.edu
Institut für Biomedizinische Technik
Karlsruher Institut für Technologie

Dipl.-Phys. Daniel Häufle
haeufle@inspo.uni-stuttgart.de
Institut für Sport- und
Bewegungswissenschaft
Universität Stuttgart

Dipl.-Ing. Thomas Heidlauf
heidlauf@mechbau.uni-stuttgart.de
Institut für Mechanik (Bauwesen)
Lehrstuhl für Kontinuumsmechanik
Universität Stuttgart

Dr. rer. nat. Rudolf Jäger
jaeger@mechbau.uni-stuttgart.de
Institut für Mechanik (Bauwesen)
Lehrstuhl für Kontinuumsmechanik
Universität Stuttgart

Dr.-Ing. Nils Karajan
karajan@mechbau.uni-stuttgart.de
Institut für Mechanik (Bauwesen)
Lehrstuhl für Kontinuumsmechanik
Universität Stuttgart

Dr. Ralf Kemkemer
ralf.kemkemer@mf.mpg.de
ZWE Biomaterialien
Max-Planck-Institut für
Metallforschung, Stuttgart

Prof. Dr.-Ing. Reinhold Kienzler
rkienzler@uni-bremen.de
Fachgebiet Technische Mechanik –
Strukturmechanik
Universität Bremen

Prof. Dr.-Ing. Wojciech Kowalczyk
wojciech.kowalczyk@uni-due.de
Lehrstuhl für Mechanik und Robotik
Universität Duisburg-Essen

Dipl.-Ing. Bastian Krüger
bastian.krueger@kit.edu
Institut für Mechanik
Karlsruher Institut für Technologie

Dipl.-Ing. Ramona Maas
rmaas@rhrk.uni-kl.de
Fachbereich Maschinenbau
und Verfahrenstechnik
Technische Universität Kaiserslautern

PD Dr.-Ing. Bernd Markert
markert@mechbau.uni-stuttgart.de
Institut für Mechanik (Bauwesen)
Lehrstuhl für Kontinuumsmechanik
Universität Stuttgart

Dipl.-Ing. Annika Radermacher
annika.radermacher@rwth-aachen.de
Institut für Angewandte Mechanik
RWTH Aachen

Dr. Eduard Rohan
rohan@kme.zcu.cz
Department of Mathemathics
and Mechanics
University of West Bohemia

Dr. Holger Schmid
schmied@km.rwth-aachen.de
Lehr- und Forschungsgebiet
Kontinuumsmechanik
RWTH Aachen

Dr. rer. nat. Syn Schmitt
schmitt@inspo.uni-stuttgart.de
Institut für Sport- und
Bewegungswissenschaft
Universität Stuttgart

Dipl.-Ing. Robert Krause
krause@mechbau.uni-stuttgart.de
Institut für Mechanik (Bauwesen)
Lehrstuhl für Kontinuumsmechanik
Universität Stuttgart

Dipl.-Ing. (FH) Frederick Lutz
frederick.lutz@hs-esslingen.de
Labor für Konstruktion
und Simulation
Hochschule Esslingen

DDipl.-Ing. Joffrey Mabuma
mabuma@mechbau.uni-stuttgart.de
Institut für Mechanik (Bauwesen)
Lehrstuhl für Kontinuumsmechanik
Universität Stuttgart

Gavin Daniel Olender, M. Sc.
gavin.olender@ddh-gruppe.de
Labor für Biomechanik und Biomaterialien, Orthopädische Klinik
Medizinische Hochschule Hannover

JP Dr.-Ing. Tim Ricken
tim.ricken@uni-due.de
Institut für Mechanik
Universität Duisburg-Essen

JP Dr.-Ing. Oliver Röhrle
roehrle@mechbau.uni-stuttgart.de
Institut für Mechanik (Bauwesen)
Lehrstuhl für Kontinuumsmechanik
Universität Stuttgart

Prof. Dr. Jens Georg Schmidt
schmidt@rheinahrcampus.de
Fachbereich Mathematik und Technik
Fachhochschule Koblenz

Dipl.-Ing. André Schmitz
a.schmitz@tu-bs.de
Institut für Festkörpermechanik
Technische Universität Braunschweig

Prof. Dr.-Ing. Karl Schweizerhof
schweizerhof@kit.edu
Institut für Mechanik
Karlsruher Institut für Technologie

Prof. Dr.-Ing. Gerhard Silber
silber@fb2.fh-frankfurt.de
Institut für Materialwissenschaften
Fachhochschule Frankfurt am Main

Dipl.-Ing. Michael Sprenger
sprenger@mechbau.uni-stuttgart.de
Institut für Mechanik (Bauwesen)
Lehrstuhl für Kontinuumsmechanik
Universität Stuttgart

Prof. Dr.-Ing. Holger Steeb
holger.steeb@ruhr-uni-bochum.de
Lehrstuhl für Mechanik –
Kontinuumsmechanik
Ruhr-Universität Bochum

Dipl.-Ing. Arndt Wagner
wagner@mechbau.uni-stuttgart.de
Institut für Mechanik (Bauwesen)
Lehrstuhl für Kontinuumsmechanik
Universität Stuttgart

Dipl.-Ing. Daniel Werner
daniel.werner@uni-due.de
Institut für Mechanik
Universität Duisburg-Essen

Senbo Xiao, M. Sc.
senbo.xiao@h-its.org
Molecular Biomechanics
Heidelberger Institut für Theoretische
Studien (HITS) gGmbH

Prof. Philippe Zysset, Ph. D.
philippe.zysset@ilsb.tuwien.ac.at
Institut für Leichtbau und
Strukturbiomechanik
Technische Universität Wien

Scientific Program

	Wednesday 24.11.10	Thursday 25.11.10	Friday 26.11.10
8:00 – 9:00		*Breakfast*	*Breakfast*
9:00 – 10:30		*Welcome* (W. Ehlers) **Section 1: Arteries & Aneurysms** J. Schmidt (invited) H. Schmid W. Kowalczyk	**Section 5: General Biomechanics** N. Karajan S. Schmitt R. Maas
10:30 – 11:00		*Coffee Break*	*Coffee Break*
11:00 – 13:00		**Section 2: Hard & Soft Tissues** E. Rohan P. Zysset B. Krüger K. Fietz	**Section 6: Cells & Biomaterials** R. Kemkemer H. Steeb S. Xiao *Closing* (W. Ehlers)
13:00 – 14:00		*Lunch*	*Lunch*
14:00 – 16:00		**Section 3: Soft Tissues** G. Silber (invited) A. Ehret T. Fritz A. Schmitz	Meeting of the Biomechanics Activity Group
16:00 – 16:30		*Coffee Break*	
16:30 – 18:00	Arrival & Check In	**Section 4: Perfusion & Growth** T. Ricken A. Wagner R. Krause	
18:00 – 19:30	*Banquet*	*Dinner*	

Sponsors


SimTech
Cluster of Excellence


LBBW
Stiftungen
Landesbank Baden-Württemberg

Released Report Series

II-1 Gernot Eipper: *Theorie und Numerik finiter elastischer Deformationen in fluidgesättigten porösen Festkörpern*, 1998.

II-2 Wolfram Volk: *Untersuchung des Lokalisierungsverhaltens mikropolarer poröser Medien mit Hilfe der Cosserat-Theorie*, 1999.

II-3 Peter Ellsiepen: *Zeit- und ortsadaptive Verfahren angewandt auf Mehrphasenprobleme poröser Medien*, 1999.

II-4 Stefan Diebels: *Mikropolare Zweiphasenmodelle: Formulierung auf der Basis der Theorie Poröser Medien*, 2000.

II-5 Dirk Mahnkopf: *Lokalisierung fluidgesättigter poröser Festkörper bei finiten elastoplastischen Deformationen*, 2000.

II-6 Heiner Müllerschön: *Spannungs-Verformungsverhalten granularer Materialien am Beispiel von Berliner Sand*, 2000.

II-7 Stefan Diebels (Ed.): *Zur Beschreibung komplexen Materialverhaltens: Beiträge anläßlich des 50. Geburtstages von Herrn Prof. Dr.-Ing. Wolfgang Ehlers*, 2001.

II-8 Jack Widjajakusuma: *Quantitative Prediction of Effective Material Parameters of Heterogeneous Materials*, 2002.

II-9 Alexander Droste: *Beschreibung und Anwendung eines elastisch-plastischen Materialmodells mit Schädigung für hochporöse Metallschäume*, 2002.

II-10 Peter Blome: *Ein Mehrphasen-Stoffmodell für Böden mit Übergang auf Interface-Gesetze*, 2003.

II-11 Martin Ammann: *Parallel Finite Element Simulations of Localization Phenomena in Porous Media*, 2005.

II-12 Bernd Markert: *Porous Media Viscoelasticity with Application to Polymeric Foams*, 2005.

II-13 Saeed Reza Ghadiani: *A Multiphasic Continuum Mechanical Model for Design Investigations of an Effusion-Cooled Rocket Thrust Chamber*, 2005.

II-14 Wolfgang Ehlers & Bernd Markert (Eds.): *Proceedings of the 1st GAMM Seminar on Continuum Biomechanics*, 2005.

II-15 Bernd Scholz: *Application of a Micropolar Model to the Localization Phenomena in Granular Materials: General Model, Sensitivity Analysis and Parameter Optimization*, 2007.

II-16 Wolfgang Ehlers & Nils Karajan (Eds.): *Proceedings of the 2nd GAMM Seminar on Continuum Biomechanics*, 2007.

II-17 Tobias Graf: *Multiphasic Flow Processes in Deformable Porous Media under Consideration of Fluid Phase Transitions*, 2008.

II-18 Ayhan Acartürk: *Simulation of Charged Hydrated Porous Materials*, 2009.

II-19 Nils Karajan: *An Extended Biphasic Description of the Inhomogeneous and Anisotropic Intervertebral Disc*, 2009.

II-20 Bernd Markert: *Weak or Strong – On Coupled Problems in Continuum Mechanics*, 2010.

II-21 Wolfgang Ehlers & Bernd Markert (Eds.): *Proceedings of the 3rd GAMM Seminar on Continuum Biomechanics*, 2012.

II-22 Wolfgang Ehlers: *Poröse Medien – ein kontinuumsmechanisches Modell auf der Basis der Mischungstheorie*, 2012.

II-23 Hans-Uwe Rempler: *Damage in Multi-phasic Materials Computed with the Extended Finite-Element Method*, 2012.

II-24 Irina Komarova: *Carbon-Dioxide Storage in the Subsurface: A Fully Coupled Analysis of Transport Phenomena and Solid Deformation*, 2012.

II-25 Yousef Heider: *Saturated Porous Media Dynamics with Application to Earthquake Engineering*, 2012.